Acceleration of Divide-and-Conquer Based Electronic Structure Calculations for Large Molecule Systems

分割統治法を用いた 大規模電子状態計算の高速化

February 2015

Waseda University
Graduate School of Advanced Science and Engineering
Department of Chemistry and Biochemistry
Research on Electronic State Theory

YOSHIKAWA Takeshi
吉川　武司

Contents

List of Abbreviations

AC	active center
AEN	approximate electron number
AFL	approximate Fermi level
AO	atomic orbital
CC	coupled cluster
CCSD	coupled cluster singles and doubles
CCSD(T)	coupled cluster singles and doubles with perturbative connected triples
CIS	configuration interaction singles
CPU	central processing unit
cuBLAS	CUDA basic linear algebra subroutines
CUDA	compute unified device architecture
cuSPARSE	CUDA sparse matrix library
DC	divide-and-conquer
DDI	distributed data interface
DFT	density functional theory
DGEMM	double precision general matrix multiply
DM	density matrix
EDA	energy density analysis
EOM	equation-of-motion
ERI	two-electron repulsion integral
ES	excitation subsystem
FMM	fast multipole method
FMO	fragment molecular orbital
GA	global arrays
GDDI	generalized distributed data interface
GPU	graphical processing unit
HF	Hartree–Fock

I/O	input/output
LR	linear response
MAGMA	matrix algebra on GPU and multicore architectures
MM	molecular mechanics
MO	molecular orbital
MPI	message-passing interface
MP2	second-order Møller–Plesset
ONIOM	our own n-layered integrated molecular orbital and molecular mechanics
OpenMP	open multi-processing
PC	personal computer
PYP	photoactive yellow protein
QM	quantum mechanics
RHF	restricted Hartree–Fock
RI	resolution of the identity
SAC	symmetry-adapted cluster
SACCI	symmetry-adapted cluster configuration interaction
SCF	self-consistent field
SIMD	single instruction multiple data
TDCPHF	time-dependent coupled perturbed Hartree–Fock
TDHF	time-dependent Hartree–Fock
TDDFT	time-dependent density functional theory
UDFT	unrestricted density functional theory
UHF	unrestricted Hartree–Fock
UMP2	unrestricted second-order Møller–Plesset
VSIPL	vector signal image processing library

General Introduction

Recent advances in parallel computing and large-scale techniques of quantum chemical calculations could have predicted various molecular properties for large systems. In the present-day computer architecture, the development of an efficient parallelization scheme is important as well as the acceleration on a single core. Large-scale techniques have the potential to reduce CPU times and required memory sizes while maintaining accuracy. The large-scale techniques can be categorized into two types: namely, (i) the multilayer theories that define two or three layers treated at different levels of accuracy and (ii) linear-scaling theories that divide an entire system into several fragments treated at the same level. A fine example of the multilayer theories is QM/MM method developed by Nobel Prize-winning Karplus, Levitt, and Warshel in 2013. QM/MM method applies the QM calculations to an active center and MM calculations to the other parts. However, this method is not suitable for the case that systems involve several active centers. On the other hand, linear-scaling techniques accelerate the large QM calculations by separately solving the local equation in each fragment. DC-SCF method originally proposed by Yang and coworkers is one of the linear-scaling techniques. Unlike to other linear-scaling techniques the DC method has a high applicability to delocalized electron and/or spin systems due to the adoption of the common Fermi level for the entire system. Furthermore, Nakai and Kobayashi have extended the DC method to electron correlation theories such as MP2 and CC theories. The DC method, however, had been limited to ground-state calculations for closed-shell systems. Further theoretical developments of the DC method were required to enhance the applicability.

This thesis involves eight chapters divided into three parts, in addition to general introduction here. Chapter 1 reviews the history and theoretical background of the DC-based closed-shell calculations.

Part I, which consists of two chapters, summarizes studies on the extension of the DC method for open-shell calculations. In Chapter 2, the DC-based linear-scaling SCF method is extended to the spin-unrestricted methods for treating large open-shell systems. The DC-UHF method can avoid specifying the numbers of up- and down-spin electrons in each fragment by introducing up- and down-spin Fermi levels. Test calculations for oligothiophenes demonstrate the high efficiency and accuracy of the DC-based unrestricted methods even for spin-delocalized systems.

Chapter 3 extends the DC-based unrestricted open-shell scheme to the correlated perturbation theory. According to the scaling analysis by the double-logarithmic plot, the

CPU times and required memory sizes scale with $O(n^5)$ and $O(n^3)$ for conventional correlated calculations, respectively. In the DC method, the both CPU times and memory sizes scale with $O(n^1)$.

Part II, which consists of three chapters, summarizes studies on the extension of the DC method for excited-state calculations. In Chapter 4, the author develops the SAC theory based on the DC method. While the perturbative configuration selection adopted in the SAC program significantly reduces its computational cost compared with the CC calculations, the reduction of the configurations leads to less inclusion of the total correlation energy. However, the numerical assessments confirm that the use of the local orbitals constructed in each subsystem in DC-SAC calculations reduces the loss in total correlation energy, which provides more reliable total and relative energies than the standard SAC method.

In Chapter 5, the DC method is extended to CIS, TDDFT, and SACCI methods for enabling excited-state calculations of large systems. In the DC-based excited-state theories, one subsystem is selected as an active center. Test calculations for formaldehyde in water and a conjugated aldehyde demonstrate the high accuracy and effectiveness of these methods. The numerical applications to PYP confirm that the DC-SACCI method significantly accelerates the excited-state calculations while maintaining high accuracy.

Chapter 6 presents the development and numerical assessments of an algorithm to calculate excited states using the dynamic polarizability as an alternative methods. The author proposes the algorithm in three sections: a constant frequency interval search, bisection method with a convergence condition of oscillator strength, and subtracting the contribution of calculated excitations from dynamic polarizability. The numerical assessment shows an appropriate interval and convergence condition to yield a large number of excitations and small errors to the conventional method. This algorithm is applied to calculate excited states of several molecules. All excitations are detected with smaller errors than the conventional method.

Part III, which consists of two chapters, summarizes studies on the high parallel programs of the DC method. Chapter 7 presents efficient algorithms for the linear-scaling DC-SCF for parallel computations. The methods adopt approximate Fermi level in order to reduce the network communication. Numerical assessments demonstrate the high parallel efficiency for the present methods without loss of accuracy.

Chapter 8 examines the DC-SCF calculation using RI approximation on GPUs. GPUs are emerging in computational chemistry to include HF methods and electron-correlation theories. However, *ab initio* calculations of large molecules face technical difficulties such as slow CPU-GPU memory access and other shortfalls of GPU memory.

The DC method could avoid these bottlenecks by separately solving local equations in individual fragments. In addition, the RI approximation enables an effective reduction in computational cost with respect to the GPU memory. The author implements the DC-RI-HF code on GPUs by using math libraries, which guarantee compatibility with future development of the GPU architecture. Numerical applications confirm that the present code using GPUs significantly accelerates the HF calculations while maintaining accuracy.

Chapter 1
Theoretical Background

1.1. History of DC method

The DC method is one of the linear-scaling techniques and originally proposed to pure Kohn–Sham DFT by Yang and the coworker [1,2]. The DC method requires no artificial prediction related to the positions of the spins and/or charges, because the distribution of electrons in the system under consideration is uniformly settled by the common Fermi level. Since the first proposal, it has been mainly applied to semiempirical MO calculations [3,4]. For performing HF and hybrid DFT calculations, Nakai's group developed and assessed the DC method including the HF exchange interactions [5–7]. Furthermore, two strategies have been proposed for evaluating the electron correlation energy. The first one uses density matrix of the entire system obtained from the DC-HF calculation for evaluating the MP2 energy by means of the DM-Laplace MP2 method [8]. The second one uses subsystem MOs for evaluating the correlation energy corresponding to the subsystem. The correlation energy of entire system is evaluated as the sum of the subsystem correlation energies by EDA techniques [9]. The second one was applied to the MP2 [10] and CC [11,12] calculations and succeeded in achieving gold-standard accuracy for the ground-state calculations for closed-shell systems.

Since 2009, Nakai's group has applied the DC method to several methodologies to enhance the applicability. The author and coworkers extended it to spin-unrestricted HF [13] and MP2 [14] calculations for open-shell systems, explained as Part I. The DC-based unrestricted calculations separately solve the local equations for up and down spins. Furthermore, the author and coworkers developed the DC-based excited-state methods [15], explained as Part II. Around the same time, the DC method was applied to property calculations with derivation such as gradient [16,17] and poralizability [18,19], and hyperporalibazility [20]. Recently, the relativistic framework has been combined with the DC-based HF, MP2, and CC theories to enhanced applicability for heavy metal systems [21]. By LUT scheme [22], which approximates the one-particle unitary transformation as a block-diagonal form of the subsystem contributions, the relativistic calculations could be performed in same computational cost as non-relativistic calculations.

Fragmentation techniques, including the DC method, could reduce the network communications by separately solving the local equation in each fragment. Therefore, the DC method has higher affinity with the multi-node parallelization than conventional quantum chemical calculations: for example, two-level hierarchical parallelization

algorithm for the DC-MP2 method [23]. The coarse-grain and fine-grain parallel treatments are accomplished by assigning one subsystem to one node and distributing the computational task of each subsystem in the same node, respectively. Because DC-HF calculations are more expensive than DC-MP2 ones in many cases, the author and the coworkers implemented and assessed the new algorithms of the DC-HF method for parallel computations, explained as Part III.

1.2. DC-SCF method

In the DC method, the system under consideration is spatially divided into disjoint subsystems, where a set of AOs in a subsystem s is represented as $\boldsymbol{S}(s)$:

$$\boldsymbol{S}(s) \bigcap \boldsymbol{S}(s') = \varnothing \quad \forall s \neq s', \tag{1.1}$$

and the union of $\boldsymbol{S}(s)$ becomes a set of AOs in the entire system represented as $\boldsymbol{T}$:

$$\bigcup_s \boldsymbol{S}(s) = \boldsymbol{T}. \tag{1.2}$$

The disjoint subsystem is called the central region. To improve the description of the subsystem, the neighboring region from the central region, which is called the buffer region, is taken into consideration when expanding subsystem MOs in the DC calculation. A set of AOs corresponding to the buffer region of subsystem s, which is denoted by $\boldsymbol{B}(s)$, is added to $\boldsymbol{S}(s)$ and one constructs a set of AOs in the localization region of subsystem s, $\boldsymbol{L}(s)$; namely,

$$\boldsymbol{S}(s) \bigcup \boldsymbol{B}(s) \equiv \boldsymbol{L}(s). \tag{1.3}$$

Hereafter, indices $\{\mu,\nu, \ldots\}$ refer to AOs, $\{i, j, \ldots\}$ to occupied MOs, $\{a, b, \ldots\}$ to virtual MOs, and $\{p,q, \ldots\}$ to all MOs. In the DC-SCF method, the density matrix of the entire system $\boldsymbol{D}$ is constructed from local density matrices for subsystems $\{s\}$ $\boldsymbol{D}^s$, as follows:

$$D_{\mu\nu} \approx D_{\mu\nu}^{\mathrm{DC}} = \sum_s P_{\mu\nu}^s D_{\mu\nu}^s, \tag{1.4}$$

where s runs all subsystems. In Eq. (1.4), $\boldsymbol{P}^s$ represents the partition matrix with elements of

$$P_{\mu\nu}^s = \begin{cases} 1 & \left[\boldsymbol{S} \quad \boldsymbol{S} \right] \\ 1/2 & \left[\boldsymbol{B} \quad \boldsymbol{S} \right] \left[\boldsymbol{S} \quad \boldsymbol{B} \right] \\ 0 & \text{otherwise.} \end{cases} \tag{1.5}$$

$\boldsymbol{P}^s$ avoids the double counting for the electron numbers of the buffer region. $\boldsymbol{D}^s$ is obtained by the subsystem MO coefficients, $\boldsymbol{C}^s$, subsystem orbital energies, $\boldsymbol{\varepsilon}^s$, and common Fermi level, ε_F:

$$D_{\mu\nu}^s = \sum_p f_\beta(\varepsilon - \varepsilon^s) C_\mu^s C_{\mu p}^s, \tag{1.6}$$

where p runs all MOs of the subsystem s, i.e., $\boldsymbol{L}(s)$. $\boldsymbol{C}^s$ and $\boldsymbol{\varepsilon}^s$ are determined by solving the following Roothaan–Hall or Kohn–Sham equation for the subsystem s:

$$\boldsymbol{F}^s \boldsymbol{C}^s = \boldsymbol{\varepsilon}^s \boldsymbol{S}^s \boldsymbol{C}^s. \tag{1.7}$$

Here, $\boldsymbol{S}^s$ and $\boldsymbol{F}^s$ represent the local overlap and Fock matrices for subsystem s, i.e., submatrices of the entire overlap and Fock matrices in the basis of $\boldsymbol{L}(s)$. After solving the local equations, the common Fermi level can be determined via constraint of the total number of electrons, N_e:

$$N_\mathrm{e} = \mathrm{Tr}[\boldsymbol{D}^{\mathrm{DC}}\boldsymbol{S}]. \tag{1.8}$$

1.3. DC-based correlation method

The DC based correlation energy is estimated by summing up the correlation energies corresponding to individual subsystems as follows:

$$\Delta E_{corr}^{\mathrm{DC}} = \sum_{s}^{\mathrm{subsystem}} \Delta E_{corr}^{s} . \tag{1.9}$$

Here, the correlation energy of subsystem s is estimated using subsystem MOs analogous to the EDA applied to the Nesbet's correlation energy representation as follows:

$$\Delta E_{corr}^{\alpha} = \sum_{ij}^{\mathrm{occ}(s)} \sum_{ab}^{\mathrm{vir}(s)} \left(\sum_{\mu \in \boldsymbol{S}'} \cdots \sum_{\nu \in \boldsymbol{S}(s)} \cdots \right) \times \left[\tilde{\ } \quad \tilde{\ } \right], \tag{1.10}$$

where $\{i^s, j^s, \ldots\}$ and $\{a^s, b^s, \ldots\}$ represent the occupied and virtual MOs of the subsystem s, respectively. $\tilde{t}_{ij,ab}^{s}$ is the effective two-electron excitation amplitude for subsystem s defined by

$$\tilde{t}_{ij,ab}^{s} = -\frac{\left\langle a^s b^s \middle| i^s j^s \right\rangle}{\varepsilon_a^s + \varepsilon_b^s - \varepsilon_i^s - \varepsilon_j^s} \qquad \text{: DC-MP2,} \tag{1.11}$$

$$\tilde{t}_{ij,ab}^{s} = t_{i,a}^{s} t_{j,b}^{s} + t_{ij,ab}^{s} \qquad \text{: DC-CCSD.} \tag{1.12}$$

In DC-CCSD method, $t_{i,a}^{s}$ and $t_{ij,ab}^{s}$ are the so-called T_1 and T_2 amplitudes, which are determined by solving the CCSD equation for the localization region of subsystem s. w_{occ} and w_{vir} are the weight parameters satisfying $w_{\mathrm{occ}} + w_{\mathrm{vir}} = 1$ that determine the contributions to the correlation energy from occupied and virtual partitionings, respectively. Kobayashi and Nakai assessed the weight parameters for the DC-MP2 method and concluded that (w_{occ}, w_{vir}) = (1, 0) gives more accurate correlation energy than (w_{occ}, w_{vir}) = (0, 1). Therefore, the reduced energy expression of Eq. (1.10) is used, unless otherwise noted.

$$\Delta E_{corr}^{s} = \sum_{ij}^{\mathrm{occ}(s)} \sum_{ab}^{\mathrm{vir}(s)} \sum_{\mu \in \boldsymbol{S}(s)} C_{\mu i}^{s*} \left\langle \mu j^s \middle| a^s b^s \right\rangle \left[\tilde{\ } \quad \tilde{\ } \right]. \tag{1.13}$$

1.4. DC-based property calculations

The definition of the polarizability follows from an expansion of the total dipole moment d with respect to the external electric field E:

$$\begin{aligned} d &= d_0 + \left.\frac{\partial d}{\partial E}\right|_0 E + \left.\frac{\partial^2 d}{\partial E \partial E'}\right|_0 EE' + \cdots \\ &= d_0 + \alpha \quad + \beta EE' + \cdots \end{aligned} \tag{1.14}$$

where d_0 is the dipole moment of the unperturbed system, α is the polarizability and β is the first hyperpolarizability. The polarizability for an oscillating electric field $E_\omega(t) = A\left(e^{+i\omega} + e^{-i\omega t}\right)$ is denoted as $\alpha(-\omega;\omega)$, and that for a static field $E_\omega(t) = A$ is $\alpha(0)$.

One consider the interaction of an N-electron closed-shell molecule with an external electric field. At the HF level, the molecular wave function is described in terms of the unperturbed self-consistent field solutions of the coefficient matrix $\boldsymbol{C}^0$ and the orbital energy ε^0

$$\boldsymbol{F}^0\boldsymbol{C}^0 = \varepsilon^0\boldsymbol{S}\boldsymbol{C}^0, \tag{1.15}$$

where the superscript 0 indicates the unperturbed matrix.

Under the external electric field, the total density matrix $\boldsymbol{D}$ can be expanded as

$$\boldsymbol{D} = \boldsymbol{D}^0 + \boldsymbol{D}(\omega)E_\omega + \cdots \tag{1.16}$$

where $\boldsymbol{D}(\omega)$ is the first-order perturbed density matrix. The total dipole moment d is represented as

$$d = \mathrm{Tr}\left[\boldsymbol{D}\boldsymbol{d}\right], \tag{1.17}$$

where $\boldsymbol{d}$ is the dipole moment matrix defined as

$$d_{\mu\nu} = \left\langle \mu \middle| \hat{d} \middle| \nu \right\rangle, \tag{1.18}$$

and $\hat{d}$ is the dipole moment operator defined as

$$\hat{d} = -\sum_i^N r_i . \tag{1.19}$$

By expanding $\boldsymbol{D}$ in Eq. (1.18) and comparing it with Eq. (1.15),

$$\alpha(-\omega;\omega) = -\mathrm{Tr}\left[\boldsymbol{D}^{(1)}(\omega)\boldsymbol{d}\right].$$

As well as the unperturbed density matrix in the DC-HF method, the density

response $\boldsymbol{D}(\pm\omega)$ appeared in the TDHF method is constructed in the DC manner:

$$D_{\mu\nu}(\pm\omega) = \sum_s D^s_{\mu\nu}(\pm\omega), \tag{1.20}$$

$$\begin{aligned} D^s_{\mu\nu}(\pm\omega) &= \sum_p \eta_p \left[C^s_{\mu p}(\pm\omega) C^{0s*}_{\nu p} + C^{0s}_{\mu p} C^{s*}_{\nu p}(\pm\omega) \right] \\ &= p^s_{\mu\nu} \sum_i \left[C^s_{\mu i}(\pm\omega) C^{0s*}_{\nu i} + C^{0s}_{\mu i} C^{s*}_{\nu i}(\pm\omega) \right]. \end{aligned} \tag{1.21}$$

As well as the standard TDHF scheme, the first-order CPHF equation for the subsystem s is given by,

$$\begin{aligned} \boldsymbol{F}^s(\pm\omega)\boldsymbol{C}^{0s} + \boldsymbol{F}^{0s}\boldsymbol{C}^s(\pm\omega) \pm \omega \boldsymbol{S}^s \boldsymbol{C}^s(\pm\omega) = \\ \boldsymbol{S}^s \boldsymbol{C}^s(\pm\omega)\boldsymbol{\varepsilon}^{0s} + \boldsymbol{S}^s \boldsymbol{C}^{0s} \boldsymbol{\varepsilon}^s(\pm\omega), \end{aligned} \tag{1.22}$$

with the orthonormalization condition,

$$\boldsymbol{C}^{0s\dagger} \boldsymbol{S}^s \boldsymbol{C}^s(\pm\omega) + \boldsymbol{C}^{s\dagger}(\mp\omega) \boldsymbol{S}^s \boldsymbol{C}^{0s} = 1. \tag{1.23}$$

$\boldsymbol{U}^s(\pm\omega)$ for the subsystem s is defined as

$$\boldsymbol{C}^s(\pm\omega) = \boldsymbol{C}^{0s} \boldsymbol{U}^s(\pm\omega), \tag{1.24}$$

and $\boldsymbol{G}^s(\pm\omega)$ for the subsystem s as

$$\boldsymbol{G}^s(\pm\omega) = \boldsymbol{C}^{0s\dagger} \boldsymbol{F}^s(\pm\omega) \boldsymbol{C}^{0s}. \tag{1.25}$$

Using Eqs. (1.23) and (1.24), the element of $\boldsymbol{U}^s(\pm\omega)$ for the subsystem s is given by

$$U^s_{ai}(\pm\omega) = \frac{G^s_{ai}(\pm\omega)}{\varepsilon^{0s}_i - \varepsilon^{0s}_a \mp \omega}, \tag{1.26}$$

$$\boldsymbol{U}^s(\pm\omega) + \boldsymbol{U}^{s\dagger}(\mp\omega) = 0. \tag{1.27}$$

References

1. W. Yang, Phys. Rev. Lett. 66 (1991) 1438.
2. W. Yang, T. S. Lee, J. Chem. Phys. 103 (1995) 5674.
3. S. L. Dixon, K. M. Merz Jr., J. Chem. Phys. 107 (1997) 879.
4. A. van der Vaart, V. Gogonea, S. L. Dixon, K. M. Merz Jr., J. Comput. Chem. 21 (200) 1494.
5. T. Akama, M. Kobayashi, H. Nakai, J. Comput. Chem. 28 (2007) 2003.
6. T. Akama, A. Fujii, M. Kobayashi, H. Nakai, Mol. Phys. 105 (2007) 2799.
7. T. Akama, M. Kobayashi, H. Nakai, J. Comput. Chem. 109 (2009) 2706.
8. M. Kobayashi, T. Akama, H. Nakai, J. Chem. Phys. 125 (2006) 204106.
9. H. Nakai, Chem. Phys. Lett. 368 (2002) 73.
10. M. Kobayashi, Y. Imamura, H. Nakai, J. Chem. Phys. 127 (2007) 074103.
11. M. Kobayashi, H. Nakai, J. Chem. Phys. 129 (2008) 044103.
12. M. Kobayashi, H. Nakai, J. Chem. Phys. 131 (2009) 114108.
13. M. Kobayashi, T. Yoshikawa, H. Nakai, Chem. Phys. Lett. 500 (2010) 172.
14. T. Yoshikawa, M. Kobayashi, H. Nakai, Theor. Chem. Acc. 130 (2011) 411.
15. T. Yoshikawa, M. Kobayashi, A. Fujii, H. Nakai, J. Phys. Chem. B 117 (2013) 5565.
16. M. Kobayashi, T. Kunisada, T. Akama, D. Sakura, H. Nakai, J. Chem. Phys. 134 (2011) 034105.
17. H. Nakai, Chem. Phys. Lett. 368 (2002) 73.
18. T. Touma, M. Kobayashi, H. Nakai, Chem. Physl. Lett. 485 (2010) 247.
19. T. Touma, M. Kobayashi, H. Nakai, Theor. Chem. Acc. 130 (2011) 701.
20. M. Kobayashi, T. Touma, H. Nakai, J. Chem. Phys. 136 (2012) 084108.
21. J. Seino, H. Nakai, J. Chem. Phys. 139 (2013) 034109.
22. J. Seino, H. Nakai, J. Chem. Phys. 136 (2012) 244102.
23. M. Katouda, M. Kobayashi, H. Nakai, S. Nagase, J. Comput. Chem. 32 (2011) 2756.

Part 1

Linear-Scaling Divide-and-Conquer Method for Open-Shell Systems

Chapter 2
Divide-and-Conquer Self-Consistent Field Calculation for Open-Shell Systems

2.1. Introduction

Transition metals in biological systems, as typified by metalloenzymes and heme proteins, play important roles for biogenic processes through the use of their flexible spin states. Thus far, the open-shell electronic state calculations based on the UHF or UDFT treatments [1] have succeeded in explaining and predicting the mechanisms of these biomolecular spin systems by using the model picking up the spin active site from the entire system [2,3]. Although the cut-out models work reasonably well for spin-localized systems, it becomes hard to effectively pick up model systems from spin-delocalized systems or bimolecular radicals and to specify their spin states. Additionally, molecular magnetic materials and nanomagnets recently attract considerable attention because these materials have good prospects as novel molecular devices. To tackle these systems in the quantum chemistry, the acceleration of the electronic structure calculations is indispensable because of their tremendous computational scaling.

Since 1980s, many types of accelerating techniques for *ab initio* electronic structure calculations have been developed. In the HF and DFT calculations, there are two obstacles to the application to large molecular systems: the construction and the diagonalization of the Fock matrix. For accelerating Fock matrix construction, several linear-scaling Coulomb methods have been proposed based on the multipole expansion [4–6] or auxiliary function expansion [7–9]. Linear-scaling HF exchange methods [10–12] are also available for insulators. These accelerated Fock techniques can be applied to both restricted and unrestricted SCF procedures.

For accelerating the step of Fock diagonalization, two categories of the linear-scaling schemes have been proposed: (i) diagonalization-free one-electron density-matrix updating approaches using, for instance, Fermi operator expansion or the purification projection (see Refs. 13 and 14 for review), and (ii) fragmentation approaches which divide the system under consideration into several subsystems and obtain the properties of the entire system by merging the results of subsystem calculations [15–21]. Although the former can be straightforwardly applied to the spin unrestricted SCF [22], its application was limited to mean-field theories. On the other hand, the latter is applicable to the post-HF correlation calculations [18,19,23–25]. However, the treatment of open-shell systems has been limited because the number of each up- and down-spin electrons

should be specified for each fragment [26,27] or a local open-shell moiety should be selected [28].

The DC method firstly proposed by Yang and Lee [29] has both aspects; the DC method divides the system under consideration into several fragments and constructs the entire density matrix by integrating the results of all fragments by means of the unique Fermi level. Recently, Nakai resarch group has assessed the DC method in HF calculations [30,31], applied to the dynamic polarizability calculations [32], and extended to the post-HF correlation theories [33–37]. Several convergence acceleration techniques have been also proposed [30,38]. After basic assessments of the DC-HF method by Nakai resarch group, He and Merz [39] independently developed the DC-HF code and assessed its effectiveness in calculations of realistic proteins. Although the DC-HF or DC-DFT calculation achieves near-linear scaling computational cost with slight loss of accuracy, its applications have been limited within the closed-shell systems so far. In the DC method, unlike with the other fragmentation methods, the definite Fermi level determines the number of electrons in each subsystem.

In this Chapter, the author enables the DC-HF and DC-DFT calculations of open-shell systems by introducing up- and down-spin Fermi levels. This scheme only requires the numbers of up- and down-spin electrons in the entire system (i.e., the total number of electrons and spin multiplicity) and can avoid specifying the numbers of up- and down-spin electrons in each subsystem. The organization of this Chapter is as follows. Section 2.2 presents the theoretical aspects of the DC-UHF method. The performance of this combined method is numerically assessed in Section 2.3. Conclusion will follow as Section 2.4.

2.2. Theory

In the UHF calculation of a system with $n_\uparrow$ up-spin and $n_\downarrow$ down-spin electrons, the one-electron density matrices for up- and down-spins, $\boldsymbol{D}^\uparrow$ and $\boldsymbol{D}^\downarrow$, are given by

$$D_{\mu\nu}^{\uparrow} = \sum_{i}^{n_\uparrow} C_{\mu i}^{\uparrow} C_{\nu i}^{\uparrow *}, \tag{2.1}$$

$$D_{\mu\nu}^{\downarrow} = \sum_{i}^{n_\downarrow} C_{\mu i}^{\downarrow} C_{\nu i}^{\downarrow *}, \tag{2.2}$$

where $C_{\mu i}^{\sigma}$ ($\sigma = \uparrow$ or $\downarrow$) represents the MO coefficient for σ-spin, which is an element of the transformation matrix from an AO basis $\{\phi_\mu\}$ to an MO basis $\{\psi_i^\sigma\}$:

$$\psi_i^\sigma(\mathbf{r}) = \sum_{\mu \in \boldsymbol{T}} C_{\mu i}^{\sigma} \phi_\mu(\mathbf{r}) \tag{2.3}$$

Equations (2.1) and (2.2) can be rewritten by introducing the Heaviside step function

$$\eta(x) = \begin{cases} 1 & (x > 0) \\ 0 & (x \le 0) \end{cases}, \tag{2.4}$$

as follows:

$$D_{\mu\nu}^{\sigma} = \sum_{q} \eta(\varepsilon^\sigma - \varepsilon_{\mathrm{F}}^\sigma) C_{\mu q}^{\sigma} C_{\nu q}^{\sigma *}, \tag{2.5}$$

where ε_q^σ represents the qth orbital energy for σ-spin, and $\varepsilon_{\mathrm{F}}^\sigma$ is the Fermi level for σ-spin, which can have any value between highest occupied and lowest virtual σ-spin orbital energies.

Hereafter, the author follows the same story as the derivation of the spin-restricted version of the DC-HF scheme [29,30]. In the DC approximation, the σ-spin density matrix of the entire system is represented in terms of subsystem density matrices as follows:

$$D_{\mu\nu}^{\sigma} \approx D_{\mu\nu}^{\sigma \mathrm{DC}} = \sum_{s} D_{\mu\nu}^{\sigma s}. \tag{2.6}$$

The density matrix of the subsystem s, $\boldsymbol{D}^{\sigma s}$, is constructed from subsystem orbitals $\{\psi_i^{\sigma s}\}$ that are expanded with subsystem bases $\{\phi_\mu \mid \mu \in \boldsymbol{L}(s)\}$:

$$D_{\mu\nu}^{\sigma} = n_{\mu\nu} \sum_{q} \eta(\varepsilon^\sigma - \varepsilon_{\mathrm{F}}^\sigma) C_{\mu q}^{\sigma} C_{\nu q}^{\sigma s *}, \tag{2.7}$$

$$\psi_i^{\sigma s}(\mathbf{r}) = \sum_{\mu \in \boldsymbol{L}(s)} C_{\mu i}^{\sigma s} \phi_\mu(\mathbf{r}), \tag{2.8}$$

where $C_{\mu q}^{\sigma s}$ and $\varepsilon_q^{\sigma s}$ are the subsystem MO coefficient and energy for σ-spin, which are determined by solving the following Pople–Nesbet equation for subsystem α,

$$\boldsymbol{F}^{\sigma}\,\boldsymbol{C}_q^{\sigma} = \varepsilon_q^{\sigma}\,\boldsymbol{S}\,\boldsymbol{C}_q^{\sigma s}. \tag{2.9}$$

Here, $\boldsymbol{S}^s$ and $\boldsymbol{F}^{\sigma s}$ represent local overlap and σ-spin Fock matrices for subsystem s that are the submatrices of the entire overlap and Fock matrices in the basis of $\boldsymbol{L}(s)$.

Each Fermi level $\varepsilon_{\mathrm{F}}^{\sigma}$ in Eq. (2.7) is determined independently and uniquely through the entire system by the following constraint of the total number of σ-spin electrons n_{e}^{σ}:

$$n_{\mathrm{e}}^{\sigma} = \mathrm{tr}\left[\boldsymbol{D}\quad\boldsymbol{S}\right] = \sum_s \sum_{\mu\in\boldsymbol{L}(s)} (\boldsymbol{D}^{\sigma s}\boldsymbol{S}^s)_{\mu\mu}. \tag{2.10}$$

To make the solution of Eq. (2.10) exist, a step function is substituted with the Fermi function,

$$D_{\mu\nu}^{\sigma} \approx n_{\mu\nu} \sum_q \theta\left(\varepsilon^{\sigma} - \varepsilon^{\sigma}\right) C_{\mu q}^{\sigma} C_{\nu q}^{\sigma *}. \tag{2.11}$$

Then the entire density matrix $\boldsymbol{D}^{\sigma\mathrm{DC}}$ can be obtained from Eq. (2.6). The entire Fock matrix $\boldsymbol{F}^{\sigma}$ is constructed in the usual manner: e.g., in the DC-UHF calculation,

$$F_{\mu\nu}^{\sigma} = H_{\mu\nu}^{\mathrm{core}} + \sum_s \sum_{\lambda\rho\in\boldsymbol{L}(s)} \left[\qquad\right], \tag{2.12}$$

with two-electron integral notation of $\left(\mu\nu\middle|\lambda\rho\right) = \iint \mu^*(\mathbf{r}_1)\,\nu(\mathbf{r}_1)\,r_{12}^{-1}\,\lambda^*(\mathbf{r}_2)\,\rho(\mathbf{r}_2)\mathrm{d}\mathbf{r}_1\mathrm{d}\mathbf{r}_2$ and core Hamiltonian matrix $\boldsymbol{H}^{\mathrm{core}}$. The Fock matrix construction of Eq. (2.12) and the density matrix construction of Eqs. (2.6) and (2.11) are iterated until convergence, as well as the standard SCF procedure. Finally, the DC-UHF energy is given as

$$E_{\text{DC-UHF}} = \frac{1}{2}\sum_s \sum_{\sigma}^{\uparrow,\downarrow} \sum_{\mu\nu\in\boldsymbol{L}(s)} D_{\mu\nu}^{\alpha\sigma}\left(h_{\nu\mu} + F_{\nu\mu}^{\sigma}\right). \tag{2.13}$$

The same procedure can be adopted in the DC-UDFT calculation by substituting the Fock matrix of Eq. (2.12) with the unrestricted Kohn–Sham Hamiltonian, and the energy expression of Eq. (2.13) with the Kohn–Sham energy.

A quantity that is specific in the open-shell UHF/UDFT calculation is the expected value of the squared spin operator $\hat{S}^2$. The UHF wavefunction is the pure eigenfunction of the *z*-spin operator $\hat{S}_z$, but usually not of $\hat{S}^2$. The expected value of $\hat{S}^2$ operator for the UHF wavefunction, which is given by [40]

$$\left\langle \hat{S}^2 \right\rangle = S_z^2 + \frac{n_\uparrow + n_\downarrow}{2} - \sum_i^{n_\uparrow}\sum_j^{n_\downarrow} \left\langle \psi_i^{\uparrow} \middle| \psi_j^{\downarrow} \right\rangle^2, \tag{2.14}$$

in case of $n_\uparrow \geq n_\downarrow$ with $S_z = (n_\uparrow - n_\downarrow)/2$, is a good indicator to estimate the level of spin

contamination. Since this value can be estimated in terms of density and overlap matrices, being as:

$$\sum_{i}^{n_\uparrow}\sum_{j}^{n_\downarrow}\left\langle \psi_i^\uparrow \middle| \psi_j^\downarrow \right\rangle^2 = \mathrm{Tr}\left[\boldsymbol{D}\ \boldsymbol{S}\boldsymbol{D}\ \boldsymbol{S} \right], \tag{2.15}$$

its estimation in the framework of the DC-UHF method is possible by replacing the density matrix expression.

It should be noted that the DC-UHF/UDFT scheme described above does not refer to the numbers of up- and down-spin electrons in each subsystem at all. The Fermi levels, or Eq. (2.10) in other words, control the apportionment of the electrons. This is a remarkable advantage over the other fragmentation-based UHF approaches that requires the numbers of up- and down-spin electrons in each fragmented system, because the prediction of the spin distribution in some systems (e.g., graphene) is more difficult than that of the electron distribution.

2.3. Numerical assessment

The DC-UHF/UDFT method was assessed in calculations of spin- and charge-delocalized oligothiophenes $H(C_4H_2S)_nH$ having D_{2h} symmetry, one of which is depicted in Fig. 2.1 for $n = 14$. All calculations were performed with the modified version of the GAMESS program package [41], where the closed-shell DC codes are incorporated. In the DC SCF calculations, the inverse temperature parameter of the Fermi function β in Eq. (2.11) was fixed to 200 a.u. unless otherwise noted. One thiophene unit in the system was adopted as one subsystem, and adjacent left and right n_b units were adopted as the corresponding buffer region (see Fig. 2.1 representing an example for $n_b = 2$). Carbon atoms and subsystems were numbered from the edge as shown in Fig. 2.1. All following calculations were performed with 6-31G* basis set [42–44].

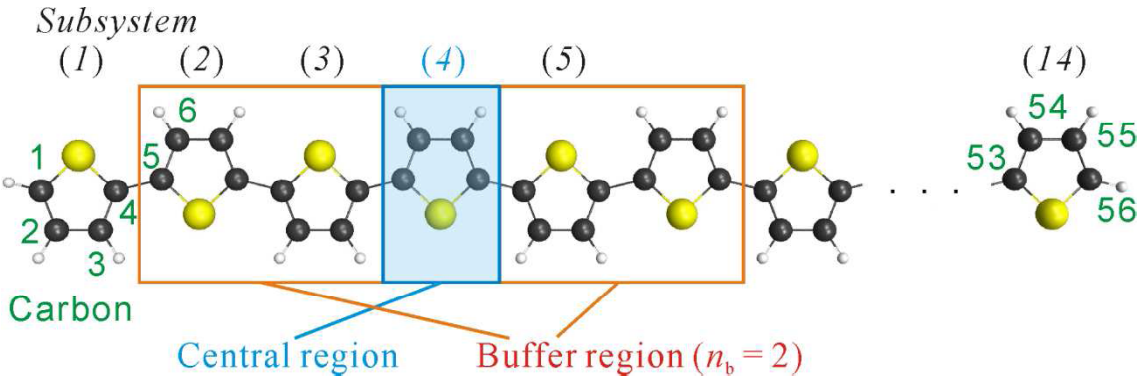

Fig. 2.1. Structure of the oligothiophene $H(C_4H_2S)_nH$ ($n = 14$) and the schematic of the central and buffer regions in the DC calculations with $n_b = 2$. The carbon atoms are numbered from one end to the other end of the conjugated chain.

Fig. 2.2(a) shows the buffer-size dependence of the total energies obtained by the DC-HF calculations of closed-shell singlet, open-shell singlet, and triplet oligothiophenes with size of n = 14. The horizontal axis represents the buffer size n_b, and the right-most data represent the conventional RHF or UHF results. The open-shell singlet is the most stable species among three and the closed-shell singlet follows. Every size of buffer can reproduce this order. As the buffer size n_b increases, all three energies rapidly converge to the conventional HF energies and the variance cannot be confirmed for $n_b \geq 3$. Fig. 2.2(b) shows the buffer-size dependence of the expected values of $\hat{S}^2$ operator, which presents similar dependence on the buffer size to the energy. The deviations of $\langle \hat{S}^2 \rangle$ from the conventional UHF results are sufficiently small (< 0.06) for $n_b \geq 3$, compared to that for $n_b = 2$ of ~0.82.

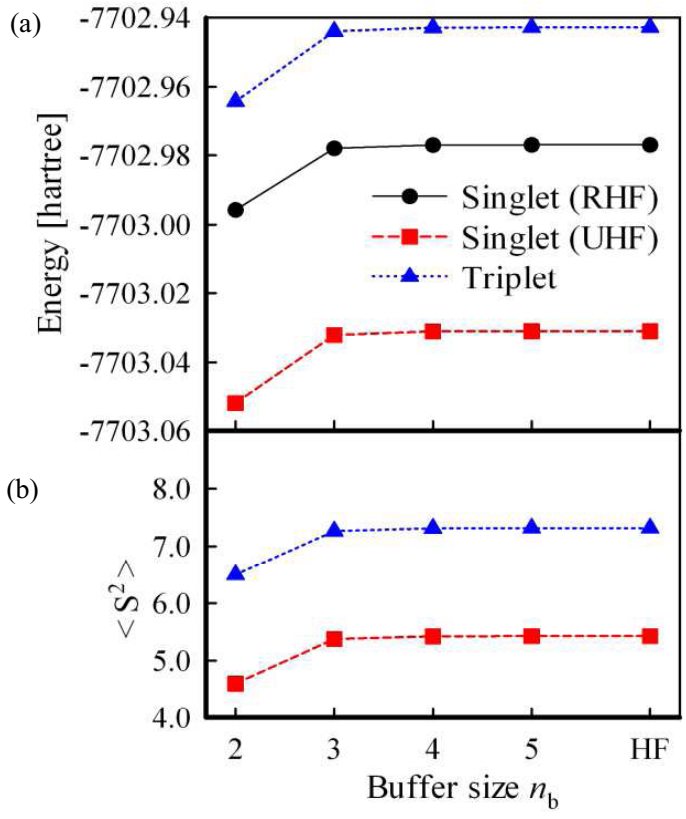

Fig. 2.2. Buffer-size dependence of (a) the total energies (in hartree) and (b) the expected values of $\hat{S}^2$ operator obtained by DC-HF/6-31G* calculations of closed-shell singlet (RHF), open-shell singlet (UHF), and triplet oligothiophenes $H(C_4H_2S)_{14}H$. The right-most data show the conventional HF results.

Fig. 2.3 shows the buffer-size dependence of the total energy errors $\Delta E = E_{\text{DC-UHF}} - E_{\text{UHF}}$ in the DC-UHF/6-31G* calculations of oligothiophene (n = 14). Here, the data of the cation doublet state are also shown in addition to those shown in Fig. 2.2. For all four states, the absolute energy errors for the buffer size of $n_{\text{b}} \geq 3$ achieve 2.2 mhartree or less, and those of $n_{\text{b}} \geq 4$ do 0.07 mhartree or less error. For the singlet and triplet states, the energies with $n_{\text{b}} = 2$ have ~20 mhartree errors. However, the relative energies among the singlet and triplet states already achieve < 2.6 mhartree error. On the other hand, the doublet state superficially attains < 1.5 mhartree error in the total energy. This state, however, corresponds to a higher energy SCF solution, which can be verified as the following.

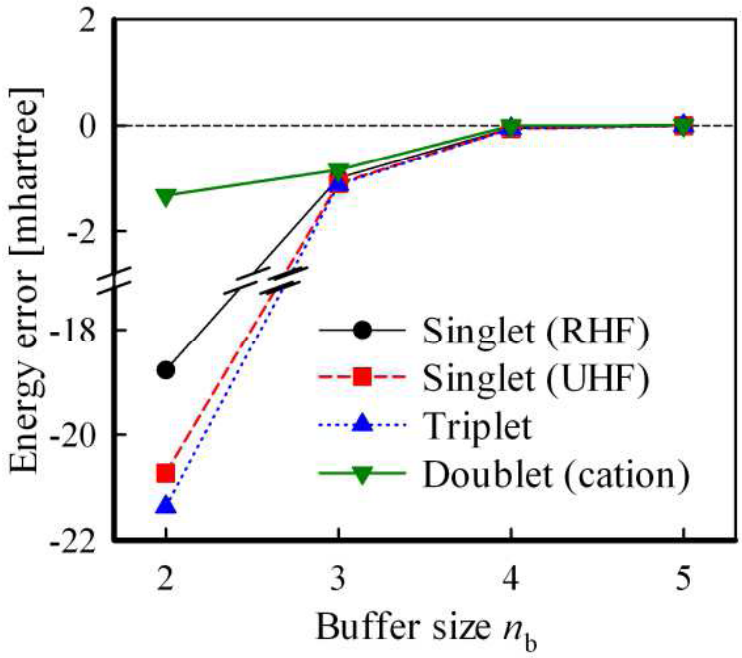

Fig. 2.3. Buffer-size dependence of the total energy errors (in mhartree) in DC-HF/6-31G* calculations of closed-shell singlet (RHF), open-shell singlet (UHF), triplet, and cation doublet states of a oligothiophene molecule $H(C_4H_2S)_{14}H$.

Table 2.1 lists the Mulliken spin densities on C_1 atom (depicted in Fig. 2.1) obtained from DC-UHF calculations for each state with n_b = 2–5. The spin densities by conventional UHF calculations are shown at the bottom row. For the singlet and triplet states, the differences from conventional UHF are less than 0.001 for all sizes of the buffer region. However for the doublet state, even the sign of the spin density by $n_b = 2$ is different from those by n_b = 3–5 or conventional UHF. By changing convergence parameters, one can circumstantially obtain an excited-state UHF solution that has ~19 mhartree higher energy than the ground-state solution and has negative spin density at C_1. In summary, the DC-UHF method with $n_b \geq 3$ offers a reasonably good (< 1 kcal/mol energy error) approximation to the conventional UHF for all four states of this system.

Table 2.1. Buffer-size dependence of Mulliken spin densities at C_1 obtained by DC-UHF/6-31G* calculations of open-shell singlet (UHF), triplet, and doublet (cation) oligothiophenes $H(C_4H_2S)_{14}H$. The conventional UHF results are also listed at the bottom.

n_b	Singlet (UHF)	Triplet	Doublet (cation)
2	+0.5603	+0.5604	–0.5275
3	+0.5613	+0.5608	+0.5611
4	+0.5607	+0.5606	+0.5618
5	+0.5607	+0.5609	+0.5616
Conventional UHF	+0.5607	+0.5607	+0.5615

Fig. 2.4(a) shows the Mulliken spin density on each carbon atom obtained by DC and conventional UHF calculations of the cation doublet-state oligothiophene (n = 14). The buffer size was varied within $2 \le n_b \le 5$ in the DC-UHF calculations. The horizontal axis represents the position of carbon atom, which is numbered in Fig. 2.1. Because the molecule has the symmetry, the values corresponding to the left moiety of Fig. 2.1 are shown. Except for the DC-UHF results with $n_b = 2$, in which the SCF solution converges to the higher-energy state, the spin densities agree well with the conventional UHF result that oscillates along with the conjugated carbon chain. The deviations of the spin densities from the conventional UHF results, which are plotted in Fig. 2.4(b) for $3 \le n_b \le 5$, are considerably small; the largest deviations are 0.0022, 0.0003, and 0.0002 for $n_b = 3$, 4, and 5, respectively. The Mulliken spin density on each atom also converges to the conventional UHF result with respect to the buffer size.

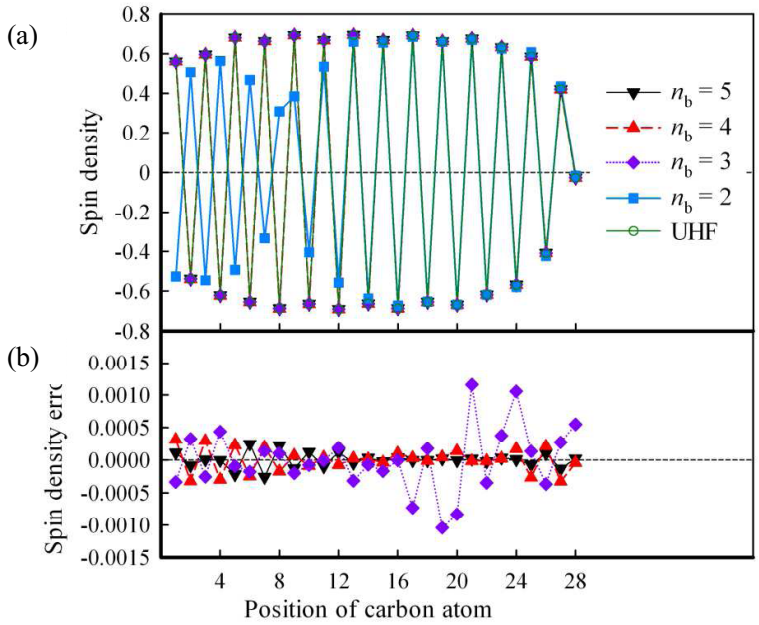

Fig. 2.4. (a) Mulliken spin density on each carbon atom obtained by DC and conventional UHF calculations of the cation doublet-state oligothiophene $H(C_4H_2S)_{14}H$ with the 6-31G* basis set. The values are plotted for each buffer size of $2 \le n_b \le 5$. (b) The deviations of the DC-UHF spin densities from the conventional UHF results for $3 \le n_b \le 5$.

Table 2.2 shows Mulliken charge and spin densities corresponding to each subsystem obtained by DC and conventional UHF calculations of the cation doublet-state oligothiophene (n = 14) with $n_b = 4$. The differences of densities between DC and conventional UHF results, which are given in parentheses, are sufficiently small (≤ 0.0004). Because the excess charge and spin are delocalized, each subsystem has fractional charge and spin densities. Note again that the number of charges or spins in each subsystem is determined from Eq. (2.10), and one needs not to specify the value before the DC-UHF/UDFT calculation. Despite this simple scheme, the DC-UHF/UDFT method can treat charge- and spin-delocalized open-shell systems with a reasonable accuracy.

Next, the accuracy of the DC-UDFT energies with typical functionals (i.e., BLYP [45,46], B3LYP [47], BHHLYP [48], and LC-BOP [49,50]) was assessed. Table 2.3 shows the adopted functional dependence of the DC and conventional UDFT energies of triplet oligothiophene (n = 14) with $n_b = 4$. Here, the results with β = 200 and 400 a.u. [the inverse temperature parameter appeared in Eq. (2.11)] are listed together. The energy errors from the conventional UDFT results are given in parentheses. Attending to the results with β = 200 a.u., the errors of BLYP and B3LYP energies are comparatively large, although those of BHHLYP and LC-BOP energies are small enough. The error introduced by the DC treatment can be roughly classified into two: the cut-off error by constructing subsystem orbitals in reduced AO space $\boldsymbol{L}(s)$ and the finite temperature error by the Fermi distribution of the occupation number in Eq. (2.11). In general, smaller band gap (the energy difference between highest occupied and lowest unoccupied MOs) leads to larger temperature error. Because the band gaps of this system evaluated from the conventional BLYP and B3LYP calculations are small (0.005 and 0.031 hartree, compared to that of HF of 0.261 hartree), large temperature errors in DC-BLYP and DC-B3LYP energies are prospective. Actually, the energy errors of DC-BLYP and DC-B3LYP can be reduced by using lower electronic temperature (β = 400 a.u.) as shown in Table 2.3.

Table 2.2. Mulliken charge and spin densities corresponding to each subsystem obtained by DC and conventional UHF calculations of the doublet (cation) oligothiophene $H(C_4H_2S)_{14}H$ with the 6-31G* basis set. The buffer size of $n_b = 4$ was adopted in the DC-UHF calculation.

Subsystem	Charge density			Spin density		
	UHF	DC-UHF	(diff.)	UHF	DC-UHF	(diff.)
(*1*), (*14*)	+0.0148	+0.0147	(–0.0001)	–0.0401	–0.0402	(–0.0000)
(*2*), (*13*)	+0.0024	+0.0024	(–0.0000)	–0.0015	–0.0015	(+0.0000)
(*3*), (*12*)	+0.0075	+0.0075	(–0.0000)	+0.0001	+0.0000	(–0.0000)
(*4*), (*11*)	+0.0170	+0.0170	(+0.0001)	+0.0015	+0.0016	(+0.0001)
(*5*), (*10*)	+0.0392	+0.0395	(+0.0003)	+0.0093	+0.0095	(+0.0002)
(*6*), (*9*)	+0.1063	+0.1064	(+0.0000)	+0.0715	+0.0716	(+0.0001)
(*7*), (*8*)	+0.3128	+0.3125	(–0.0002)	+0.4593	+0.4589	(–0.0004)

Table 2.3. Adopted DFT functional dependence of the total energy (in hartree) obtained by DC and conventional UDFT calculations of triplet oligothiophene $H(C_4H_2S)_{14}H$ with the 6-31G* basis set. The buffer size of $n_b = 4$ was adopted in DC calculations.

Functional	UDFT energy [hartree]	DC-UDFT (β = 200 a.u.)		DC-UDFT (β = 400 a.u.)	
		Energy [hartree]	(diff.) [mhartree]	Energy [hartree]	(diff.) [mhartree]
HF	–7702.942813	–7702.942871	(–0.058)	–7702.942871	(–0.058)
BLYP	–7725.220236	–7725.212877	(+7.359)	–7725.215185	(+5.051)
B3LYP	–7726.359647	–7726.352891	(+6.756)	–7726.358038	(+1.609)
BHHLYP	–7724.784913	–7724.784753	(+0.160)	–7724.784791	(+0.122)
LC-BOP	–7716.659317	–7716.659314	(+0.003)	–7716.659317	(+0.000)

Finally, the efficiency of the DC-UHF method was examined by measuring the CPU time. An Intel Xeon X5355 (2.66 GHz) processor was used on a single core. Triplet oligothiophenes (n = 10–24) were calculated with the buffer size of n_b = 3 in DC-UHF calculations. Fig. 2.5(a) shows the CPU times for solving SCF equations in the first SCF iteration of the conventional and DC-UHF calculations. The horizontal axis represents the number of units n. As is expected from the DC-RHF result presented in the previous paper [30], the DC-UHF method drastically reduces the computational time from the conventional UHF time. Although the larger system makes the efficiency of the DC-UHF method greater, the DC-UHF time becomes shorter than the conventional UHF time even for n = 14. According to the scaling analysis by the double-logarithmic plot, the times scale with $O(n^{3.54})$ and $O(n^{1.34})$ for conventional and DC-UHF calculations, which reasonably agree with the theoretical asymptotic values of $O(n^3)$ and $O(n^1)$, respectively. Fig. 2.5(b) shows the times for constructing Fock matrix in the first SCF iteration. In these calculations, FMM implemented in the GAMESS program was switched on. Although the Fock matrix construction scheme for the DC calculations is the same as that for the conventional calculations, the DC-UHF times are always shorter than the conventional UHF times. Furthermore, the DC-UHF method reduces the order of this step; the times scale with $O(n^{1.83})$ and $O(n^{1.16})$ for conventional and DC-UHF calculations, respectively. The combination of the DC method with FMM works considerably well and achieves the linear-scaling computational time because the sparse density matrix of the DC-UHF calculation makes the screening more efficiently than that of conventional UHF.

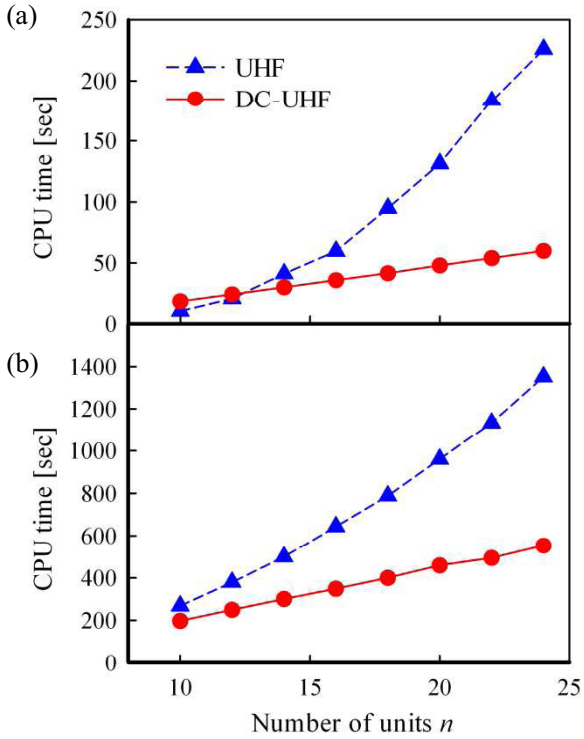

Fig. 2.5. System-size dependence of the CPU times (in sec) for (a) solving SCF equations and (b) constructing Fock matrix in the first SCF iteration of the DC and conventional UHF calculations of triplet oligothiophenes $H(C_4H_2S)_nH$ (n = 10–24) with the 6-31G* basis set. An Intel Xeon X5355 (2.66 GHz) processor was used on a single core. The buffer region was fixed at n_b = 3 in DC-UHF calculations. The FMM option implemented in the GAMESS program was switched on.

2.4. Conclusion

In this Chapter, the author has derived the spin-unrestricted open-shell version of the linear-scaling DC SCF method. Unlike to the other fragmentation-based linear-scaling open-shell treatments, the DC-UHF/UDFT does not require the position of excess spins or charges. This method was implemented into the GAMESS program and was assessed by the illustrative application to spin-delocalized oligothiophenes. Numerical assessments revealed that the accuracy of the DC-UHF method was comparable to that of the closed-shell DC-HF method: the energy and spin-density errors reduced along with the buffer size. Non-integer charge and spin densities in each subsystem were also confirmed. Furthermore, the CPU time for the DC-UHF calculation scaled linearly with respect to the system size by combining with the FMM.

The DC-UHF/UDFT method that only requires the entire charge and spin multiplicity of a system will enable us the black-box linear-scaling treatments of interesting open-shell systems such as magnetic materials, to say nothing of biological spin systems. Although the author only showed the results of one-dimensional uniform polymers in this Chapter, the DC-UHF/UDFT method can be straightforwardly applied to three-dimensional systems, to which the closed-shell DC method has already be applied (e.g., see Ref. 39). Applications to various systems such as the organic spin devices and the metalloenzymes will appear in the near future.

As mentioned in the Introduction, the DC method has both aspects of two linear-scaling SCF categories. Therefore, the extension to the post-HF correlation calculation is possible by means of the density matrix-based formalism [33] or energy partitioning-based method [34–37], which will be reported next Chapter.

References

1. J. A. Pople, R. K. Nesbet, J. Chem. Phys. 22 (1954) 571.
2. P. E. M. Siegbahn, M. R. A. Blomberg, Chem. Rev. 100 (2000) 421.
3. D. A. Scherlis, D. A. Estrin, Int. J. Quantum Chem. 87 (2002) 158.
4. C. A. White, M. Head-Gordon, J. Chem. Phys. 101 (1994) 6593.
5. M. C. Strain, G. E. Scuseria, M. J. Frisch, Science 271 (1996) 51.
6. C. H. Choi, K. Ruedenberg, M. S. Gordon, J. Comput. Chem. 22 (2001) 1484.
7. L. Füsti-Molnár, P. Pulay, J. Chem. Phys. 117 (2002) 7827.
8. Y. Kurashige, T. Nakajima, K. Hirao, J. Chem. Phys. 126 (2007) 144106.
9. M. A. Watson, Y. Kurashige, T. Nakajima, K. Hirao, J. Chem. Phys. 128 (2008) 054105.
10. E. Schwegler, M. Challacombe, J. Chem. Phys. 105 (1996) 2726.
11. J. C. Burant, G. E. Scuseria, M. J. Frisch, J. Chem. Phys. 105 (1996) 8969.
12. C. Ochsenfeld, C. A. White, M. Head-Gordon, J. Chem. Phys. 109 (1998) 1663.
13. S. Goedecker, Rev. Mod. Phys. 71 (1999) 1085.
14. S. Y. Wu, C. S. Jayanthi, Phys. Rep. 358 (2002) 1.
15. D. G. Fedorov, K. Kitaura, J. Phys. Chem. A 111 (2007) 6904.
16. D. G. Fedorov, K. Kitaura, The Fragment Molecular Orbital Method: Practical Applications to Large Molecular Systems, CRC Press, Boca Raton, 2009.
17. D. W. Zhang, J. Z. H. Zhang, J. Chem. Phys. 119 (2003) 3599.
18. S. Li, W. Li, T. Fang, J. Am. Chem. Soc. 127 (2005) 7215.
19. V. Deev, M. A. Collins, J. Chem. Phys. 122 (2005) 154102.
20. S. R. Gadre, R. N. Shirsat, A. C. Limaye, J. Phys. Chem. 98 (1994) 9165.
21. V. Ganesh, R. K. Dongare, P. Balanarayan, S. R. Gadre, J. Chem. Phys. 125 (2006) 104109.
22. H. J. Xiang, W. Z. Liang, J. Yang, J. G. Hou, Q. Zhu, J. Chem. Phys. 123 (2005) 124105.
23. Y. Mochizuki, S. Koikegami, T. Nakano, S. Amari, K. Kitaura, Chem. Phys. Lett. 396 (2004) 473.
24. D. G. Fedorov, K. Kitaura, J. Chem. Phys. 123 (2005) 134103.
25. K. Babu, S. R. Gadre, J. Comput. Chem. 24 (2003) 484.
26. J. Korchowiec, F. L. Gu, Y. Aoki, Int. J. Qunatum Chem. 105 (2005) 875.
27. Y. Orimoto, F. L. Gu, J. Korchowiec, A. Imamura, Y. Aoki, Theor. Chem. Acc. 125 (2010) 493.
28. S. R. Pruitt, D. G. Fedorov, K. Kitaura, M. S. Gordon, J. Chem. Theory Comput. 6

(2010) 1.
29. W. Yang, T.-S. Lee, J. Chem. Phys. 103 (1995) 5674.
30. T. Akama, M. Kobayashi, H. Nakai, J. Comput. Chem. 28 (2007) 2003.
31. T. Akama, A. Fujii, M. Kobayashi, H. Nakai, Mol. Phys. 105 (2007) 2799.
32. T. Touma, M. Kobayashi, H. Nakai, Chem. Phys. Lett. 485 (2010) 247.
33. M. Kobayashi, T. Akama, H. Nakai, J. Chem. Phys. 125 (2006) 204106.
34. M. Kobayashi, Y. Imamura, H. Nakai, J. Chem. Phys. 127 (2007) 074103.
35. M. Kobayashi, H. Nakai, J. Chem. Phys. 129 (2008) 044103.
36. M. Kobayashi, H. Nakai, Int. J. Quantum Chem. 109 (2009) 2227.
37. M. Kobayashi, H. Nakai, J. Chem. Phys. 131 (2009) 114108.
38. T. Akama, M. Kobayashi, H. Nakai, Int. J. Quantum Chem. 109 (2009) 2706.
39. X. He, K. M. Merz, Jr., J. Chem. Theory Comput. 6 (2010) 405.
40. C. J. Cramer, Essentials of Computational Chemistry, 2nd ed., John Wiley & Sons Ltd., West Sussex, 2004, Appendix C.
41. M.W. Schmidt, K. K. Baldridge, J. A. Boatz, S. T. Elbert, M. S. Gordon, J. H. Jensen, S. Koseki, N. Matsunaga, K. A. Nguyen, S. Su, T. L. Windus, M. Dupuis, J. A. Montgomery, Jr., J. Comput. Chem. 14 (1993) 1347.
42. W. J. Hehre, R. Ditchfield, J. A. Pople, J. Chem. Phys. 56 (1972) 2257.
43. P. C. Hariharan, J. A. Pople, Theor. Chim. Acta, 28 (1973) 213.
44. M. M. Francl, W. J. Petro, W. J. Hehre, J. S. Binkley, M. S. Gordon, D. J. DeFrees, J. A. Pople, J. Chem. Phys. 77 (1982) 3654.
45. A. D. Becke, Phys. Rev. A 38 (1988) 3098.
46. C. Lee, W. Yang, R. G. Parr, Phys. Rev. B 37 (1988) 785.
47. P. J. Stephens, F. J. Devlin, C. F. Chabalowski, M. J. Frisch, J. Phys. Chem. 98 (1994) 11623.
48. A. D. Becke, J. Chem. Phys. 98 (1993) 1372.
49. T. Tsuneda, T. Suzumura, K. Hirao, J. Chem. Phys. 110 (1999) 10664.
50. H. Iikura, T. Tsuneda, T. Yanai, K. Hirao, J. Chem. Phys. 115 (2001) 3540. T. D. Crawford, H. F. Schaefer, III. In *Reviews in Computational Chemistry*; Wiley: New York, 2000; Vol. 14, pp 33–136.

Chapter 3
Divide-and-Conquer Second-Order Møller–Plesset Perturbation Calculation for Open-Shell Systems

3.1. Introduction

The MP2 theory [1] has been widely used because it is the most practical (modestly accurate and fast) MO method that can deal with electron correlation in nonempirical manner. Therefore, many quantum chemists have practiced the efficient implementations of the MP2 computation to date. Recent trends in developing the efficient MP2 schemes have been to approximate the MP2 computation by using a rapid calculation trick of the standard MP2 formalism (e.g., local correlation methods [2–7], Laplace-transformed methods [8–15], RI techniques [16,17], and Cholesky decomposed techniques [18,19]) or by fragmenting the system under consideration (e.g., FMO method [20–23], molecular tailoring approach [24–26], incremental correlation schemes [27,28], and the DC method [29–31]). However, an efficient implementation of the straightforward MP2 formalism is indispensable not only to improve the fundamental performance of the approximate treatment but also to evaluate these approximation schemes.

In the past several years, Nagase and coworkers have offered efficient MP2 schemes especially tuned to parallel implementation. They first provided non-approximate MP2 energy calculation scheme [32] and extended it to the nuclear gradient evaluation [33]. This scheme, commonly called IMS-MP2, allowed one to run actual MP2 calculations with ~2000 basis functions using a moderate-size PC cluster. In the next place, they presented parallel RI-MP2 implementation in 2009 [34]. This MP2 scheme is further extended to the periodic system calculations with Bloch Gaussian basis functions [35]. These two excellent schemes have been implemented into the GAMESS program package [36] and interfaced to the GAMESS-FMO program [37] with an exception of the periodic RI-MP2 method.

Nakai resarch group also implemented the fragmentation-based linear-scaling DC-MP2 method into the GAMESS package (for review, see Refs. [38,39]). The DC method was firstly proposed by Yang and coworkers [40,41] in the framework of the one-body approximation such as the HF method and DFT. Nakai resarch group investigated

its performance for calculations including HF exchange interactions [42–44] and have applied the method to static and dynamic (hyper)polarizability calculations [45,46]. After basic assessments of the DC-HF method by Nakai resarch group, He and Merz [47] independently developed the DC-HF code and assessed its effectiveness in calculations of realistic closed-shell proteins. Furthermore, its extensions to MP2 and the other electron correlation theories (namely, a series of CC methods) were handled by Nakai resarch group in a different fashion [29–31,48,49] with the assistance of EDA [50]. Recently the DC-MP2 module in GAMESS has been interfaced to the IMS-MP2 code [51]. The history of the DC method is well described in a recent review paper [39].

The applications of the DC method were limited to the closed-shell systems until the author utilized the UHF or UDFT scheme to the DC method [52]. The DC-UHF/UDFT methods have an important advantage over the other fragmentation-based linear-scaling open-shell treatments [53–57], because they do not require an artificial guess for the position of excess spins or charges. In the elongation method [55,56], where the spin-delocalized π-conjugated systems have been treated with reasonable accuracy, each piecewise calculation is performed for an integer number of electrons, and the number of electrons for the fragment that is frozen in the forthcoming calculation should be specified in integer number. On the other hand, in the DC method, no artificial prediction related to the positions of the spin and/or charge is required because the distribution of electrons in the system under consideration is uniformly settled by the common Fermi level. However, no *ab initio* electron correlation theories have been practiced in the DC calculations of open-shell systems.

In this Chapter, the author extends the DC-MP2 method to the unrestricted orbital based open-shell calculations, which the author calls DC-UMP2. The organization of this Chapter is as follows. Section 3.2 presents the theoretical aspects of the DC-UMP2 method after a brief summary of the DC-UHF/UDFT method. Numerical applications of the DC-UMP2 scheme are given in Section 3.3 in calculations of the charge- and spin-delocalized polyene cation systems. The conclusion follows as Section 3.4.

3.2. Theory

The electron correlation energy of the MP2 method can be expressed in terms of active occupied orbitals $\{\varphi_i, \varphi_j\}$ and virtual orbitals $\{\varphi_a, \varphi_b\}$ with the two-electron integral notations as follows:

$$\Delta E_{\mathrm{corr}} = -\sum_{i<j}^{\mathrm{occ}} \sum_{a<b}^{\mathrm{vir}} \frac{\left|\langle ij|ab\rangle - \langle ij|ba\rangle\right|^2}{\varepsilon_a + \varepsilon_b - \varepsilon_i - \varepsilon_j}, \tag{3.1}$$

in spin-orbital notation. In the UMP2 theory, the correlation energy can be rewritten with spatial orbitals as sum of up-spin, down-spin, and cross terms as follows:

$$\begin{aligned}\Delta E_{\mathrm{UMP2}} = & \sum_{i^\uparrow<j^\uparrow}^{\mathrm{occ}} \sum_{a^\uparrow<b^\uparrow}^{\mathrm{vir}} \left\langle i^\uparrow j^\uparrow \middle| a^\uparrow b^\uparrow \right\rangle \left[\tilde{} \qquad \tilde{} \qquad \right] \\ & + \sum_{i^\downarrow<j^\downarrow}^{\mathrm{occ}} \sum_{a^\downarrow<b^\downarrow}^{\mathrm{vir}} \left\langle i^\downarrow j^\downarrow \middle| a^\downarrow b^\downarrow \right\rangle \left[\tilde{} \qquad \tilde{} \qquad \right] \\ & + \sum_{i^\uparrow}^{\mathrm{occ}} \sum_{j^\downarrow}^{\mathrm{occ}} \sum_{a^\uparrow}^{\mathrm{vir}} \sum_{b^\downarrow}^{\mathrm{vir}} \left\langle i^\uparrow j^\downarrow \middle| a^\uparrow b^\downarrow \right\rangle \tilde{t}_{i^\uparrow j^\downarrow, a^\uparrow b^\downarrow},\end{aligned} \tag{3.2}$$

where $\tilde{t}_{i^\sigma j^{\sigma'}, a^\sigma b^{\sigma'}}$ represents an effective two-electron excitation coefficient as follows:

$$\tilde{t}_{i^\sigma j^{\sigma'}, a^\sigma b^{\sigma'}} = -\frac{\left\langle a^\sigma b^{\sigma'} \middle| i^\sigma j^{\sigma'} \right\rangle}{\varepsilon_a^\sigma + \varepsilon_b^{\sigma'} - \varepsilon_i^\sigma - \varepsilon_j^{\sigma'}}. \tag{3.3}$$

In the DC-based correlation theory, the total correlation energy is estimated by summing up correlation energies corresponding to individual subsystems. The author has extend this strategy to the UMP2 theory:

$$\Delta E_{\mathrm{DC\text{-}UMP2}} = \sum_{s}^{\mathrm{subsystem}} \Delta E_{\mathrm{UMP2}}^{s}. \tag{3.4}$$

Here, the correlation energy of subsystem *s* is estimated using subsystem orbitals, which are constructed in the localization region, containing not only the central region but also the buffer region. While the buffer regions overlap in several subsystems, the central ones have no overlap. To avoid double counting, the correlation energies corresponding to the central regions should be estimated. Thus, the author adopts the EDA technique [50] to the UMP2 correlation energy representation as follows:

$$\Delta E^{s}_{\mathrm{UMP2}} = \sum_{\sigma}^{\uparrow,\downarrow} \sum_{i^{\sigma} < j^{\sigma}}^{\mathrm{occ}} \sum_{a^{\sigma} < b^{\sigma}}^{\mathrm{vir}} \sum_{\mu \in \boldsymbol{S}(s)} C^{\sigma *}_{\mu i} \left\langle \mu j^{\sigma} \middle| a^{\sigma} b^{\sigma s} \right\rangle \Big[\tilde{} \qquad \tilde{} \qquad \Big]$$

$$+ \sum_{i^{\uparrow s}}^{\mathrm{occ}} \sum_{j^{\downarrow s}}^{\mathrm{occ}} \sum_{a^{\uparrow s}}^{\mathrm{vir}} \sum_{b^{\downarrow s}}^{\mathrm{vir}} \sum_{\mu \in \boldsymbol{S}(s)} \frac{1}{2} \Big(C^{\uparrow s *}_{\mu i} \left\langle \mu j^{\downarrow s} \middle| a^{\uparrow s} b^{\downarrow s} \right\rangle \qquad (3.5)$$

$$+ C^{\downarrow s *}_{\mu j} \left\langle i^{\uparrow s} \mu \middle| a^{\uparrow s} b^{\downarrow s} \right\rangle \Big) \tilde{t}^{s}_{i^{\uparrow} j^{\downarrow}, a^{\uparrow} b^{\downarrow}},$$

$\tilde{t}^{s}_{i^{\sigma} j^{\sigma'}, a^{\sigma} b^{\sigma'}}$ represents an effective two-electron excitation coefficient for subsystem *s* as follows:

$$\tilde{t}^{s}_{i^{\sigma} j^{\sigma'}, a^{\sigma} b^{\sigma'}} = - \frac{\left\langle a^{\sigma} b^{\sigma'} \middle| i^{\sigma} j^{\sigma' s} \right\rangle}{\varepsilon^{\sigma}_{a} + \varepsilon^{\sigma'}_{b} - \varepsilon^{\sigma}_{i} - \varepsilon^{\sigma' s}_{j}}. \qquad (3.6)$$

In the calculations, the author utilizes the dual-buffer DC scheme, where the buffer regions used for the DC-based correlation calculation are set to be smaller than those for the DC-HF calculation. This scheme, described in detail in Ref. 31, reduces the computational efforts for the evaluation of the correlation energy with keeping its accuracy. Furthermore, the DC-HF procedure can be substituted with the standard HF by taking the limit of infinite buffer size. Although the computational cost for the conventional HF calculation scales as $O(n^3)$, it is usually significantly less than the cost for the MP2 calculation.

A quantity that specifically appears in unrestricted open-shell calculations is the expected value of the squared spin operator $\hat{S}^2$, which indicates the degree of spin contamination. One should care more about the issue of spin contamination when adopting the UHF or UMP2 method than UDFT. Although the spin-projection methods such as projected UHF and UMP2 [58] are the possible candidates for regaining from the spin contamination, they violate the size-consistency, which must be maintained in the DC scheme. $\left\langle \hat{S}^2 \right\rangle$ is generally given with the reduced two-electron density matrix Γ as [59]

$$\left\langle \hat{S}^2 \right\rangle = S_z{}^2 + \frac{n_{\uparrow} + n_{\downarrow}}{2} + \sum_{p^{\uparrow} q^{\downarrow} r^{\downarrow} s^{\uparrow}} \left\langle p^{\uparrow} \middle| r^{\downarrow} \right\rangle \left\langle q^{\downarrow} \middle| s^{\uparrow} \right\rangle \Gamma_{p^{\uparrow} q^{\downarrow} r^{\downarrow} s^{\uparrow}}, \qquad (3.7)$$

where n_{σ} is the number of σ-spin electrons and $S_z = \left(n_{\uparrow} - n_{\downarrow} \right) / 2$. In the DC-UHF method [52], the third term of Eq. (3.7) can be evaluated with the DC-UHF density matrices. However, no one has derived the DC-MP2 density matrix so far. The author will report the scheme to evaluate $\left\langle \hat{S}^2 \right\rangle$ in the DC-UMP2 elsewhere.

3.3. Numerical assessment

The DC-UMP2 method was assessed in calculations of polyene cation doublet $C_nH_{n+2}^+$. All calculations were performed with the modified version of the GAMESS program package [36]. C_2H_4 (or C_2H_5 for the edges) was adopted as a central region and several adjacent C_2H_4 (or C_2H_5) units were treated as the corresponding buffer region. The size of buffer region is denoted by n_b^{corr} that indicates the number of carbon atoms in each left and right buffer region. The following calculations were performed with the 6-31G** basis set [60] unless otherwise noted. Applying the dual-buffer DC correlation scheme, only the electron correlation was treated with the DC approach after the standard UHF calculations for clearly showing that the errors reported in the present study originate only in the DC-UMP2 approximation.

Table 3.1 shows the correlation buffer size (n_b^{corr}) dependence of the correlation energies obtained by the DC-UMP2 calculations of polyene cation $C_{30}H_{32}^+$. The energies of neutral polyene $C_{30}H_{32}$ obtained by the restricted MP2 calculations are also tabulated for comparison. The conventional MP2 correlation energies are listed on the bottom line, and the differences between DC and standard energies are presented in parentheses in mhartree. As the correlation buffer size n_b^{corr} increases, the energy error became small. The energy errors for $n_b^{corr} \geq 6$ were less than 1.4 mhartree that achieves so-called chemical accuracy (1 kcal/mol). It was also found that the errors by the DC-UMP2 calculations are comparable to those by the closed-shell DC-MP2 calculations except for the case adopting the smallest buffer size of $n_b^{corr} = 4$, where the so-called error cancellation may occur. Note that the correlation energy errors of the neutral polyene system reported in the results were slightly larger than those in Ref. 48, where the smaller 6-31G basis set was adopted, although they were comparable to those in Ref. 49 adopting the same 6-31G** basis set in the CCSD(T) level of theory.

Table 3.2 compares the total energies of polyene cation systems $C_nH_{n+2}^+$ (n = 10, 20, 26, 30, 40, and 60) obtained by the DC and conventional UMP2 methods. The correlation buffer size was fixed to n_b^{corr} = 8 in the DC calculations, which is larger than in the DC-CC studies [48,49] because the cost for the MP2 correlation calculation is significantly lower than that for CC calculation. The differences between DC and conventional energies are shown in parentheses in mhartree. The energy error for n = 10 became zero because all localization regions contain the entire system when using n_b^{corr} = 8. It was found that the errors introduced by the DC method keep less than 0.5 mhartree for n = 20–40 by using n_b^{corr} = 8.

Table 3.1. Correlation buffer-size dependence of DC-MP2 correlation energies (in hartree) of the neutral and cation polyenes, $C_{30}H_{32}$ and $C_{30}H_{32}^{+}$, at the 6-31G** level. The closed-shell neutral polyene was calculated adopting the restricted orbitals. DC scheme was only applied to the correlation calculation after the standard HF calculation. Energy deviations from conventional MP2 results are shown in parentheses in mhartree.

	Neutral		Cation	
$n_{\mathrm{b}}^{\mathrm{corr}}$	ΔE_{RMP2} [hartree]	(diff.) [mhartree]	ΔE_{UMP2} [hartree]	(diff.) [mhartree]
4	–3.992941	(+2.780)	–3.774790	(–0.452)
6	–3.994383	(+1.339)	–3.772970	(+1.367)
8	–3.995231	(+0.490)	–3.773936	(+0.402)
10	–3.995582	(+0.140)	–3.774274	(+0.064)
Conventional	–3.995721	-	–3.774338	-

Table 3.2. System-size dependence of DC and conventional UMP2 total energies (in hartree) of the polyene cation $C_nH_{n+2}^{+}$ at the 6-31G** level with $n_{\mathrm{b}}^{\mathrm{corr}} = 8$. DC scheme was only applied to the correlation calculation after the standard UHF calculation. Energy deviations from conventional UMP2 results are shown in parentheses in mhartree.

n	E_{UMP2} [hartree]	$E_{\mathrm{DC\text{-}UMP2}}$ [hartree]	(diff.) [mhartree]
10	–386.646383	–386.646383	(–0.000)
20	–772.401788	–772.401678	(+0.105)
26	–1003.812448	–1003.812359	(+0.090)
30	–1158.112941	–1158.112539	(+0.402)
40	–1543.817715	–1543.817507	(+0.209)
60	–	–2315.223720	–

The efficiency of the DC-UMP2 method was examined by measuring the CPU time. An Intel Xeon X5470 (3.33 GHz) processor was used on a single core. Table 3.3 shows the system-size dependence of the CPU times and required memory sizes for the DC and conventional UMP2 calculations of polyene cation systems $C_nH_{n+2}^+$ (n = 10, 20, 26, 30, 40, and 60) with the correlation buffer-size n_b^{corr} = 8. The CPU times and required memory sizes are plotted in Figs. 3.1(a) and (b), respectively. Note that the time for the HF iterations preceding the MP2 calculation is not included because the author utilized the standard full SCF procedure for both DC and conventional calculations. As expected from the closed-shell DC-MP2 presented in the previous paper [30], the DC-UMP2 method drastically reduced the CPU time from the conventional UMP2 time. For $n \leq 20$ the times for DC-UMP2 calculations were larger than those for the conventional calculations, because the median localization region contains up to 18 carbon atoms. However, for $n \geq 26$, the DC method becomes faster than the conventional method. According to the scaling analysis by the double-logarithmic plot, the CPU times scaled with $O(n^{5.57})$ and $O(n^{1.53})$ for conventional and DC-UMP2 calculations, respectively, which are slightly larger than the theoretical asymptotic values of $O(n^5)$ and $O(n^1)$. The implementation is based on the UMP2 code in the GAMESS program, which requires heavy disk I/O. The disk I/O may reduce the effectiveness of both conventional and DC-MP2 from their theoretical limit. For n = 10, where all localization regions contain the entire system, the required memory size for the DC-UMP2 calculation is approximately twice as large as that for the conventional UMP2 calculation because the evaluation of the correlation energy corresponding to the central region requires additional memories to the conventional UMP2 calculation. For $n \geq 26$, however, the memory size required for the DC-UMP2 calculation is constant with respect to the system size n, while that for the conventional calculation increases quasi-proportionally to n^3.

Table 3.3. System-size dependence of DC and conventional UMP2 CPU times (in min) and required memory size (in MB) of the polyene cation $C_nH_{n+2}^+$ at the 6-31G** level with n_b^{corr} = 8. An Intel Xeon X5470 (3.33 GHz) processor was used on a single core.

n	CPU time [min]		Required memory size [MB]	
	Conventional UMP2	DC-UMP2	Conventional UMP2	DC-UMP2
10	2.0	16.7	76.4	150.2
20	31.3	139.8	558.8	783.0
26	319.6	264.3	1203.1	751.4
30	697.1	347.0	1831.8	751.4
40	3514.8	551.2	4278.5	751.4
60	-	960.9	-	751.4

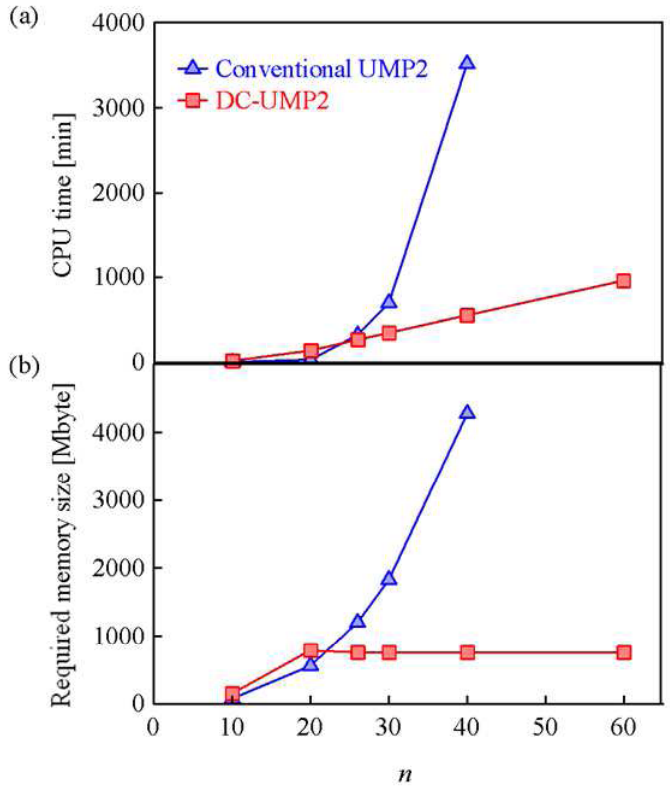

Fig. 3.1. System size dependences of UMP2 (a) CPU times (in min) and (b) required memory size (in MB) for the DC and conventional UMP2 calculations of the polyene cation $C_nH_{n+2}^+$ at the 6-31G** level with n_b^{corr} = 8. An Intel Xeon X5470 (3.33 GHz) processor was used on a single core.

Finally, Table 3.4 shows the basis-set dependence of the total energies obtained by the DC-UMP2 calculations of polyene cation $C_{40}H_{42}^{+}$. STO-6G [61], 6-31G [62], 6-311G [63], and 6-311G** [63] basis sets were adopted in addition to the 6-31G** set. The correlation buffer size was fixed to $n_{\mathrm{b}}^{\mathrm{corr}} = 8$. The differences between DC and conventional energies are presented in parentheses in mhartree. The energy errors did not show significant dependence on the basis set adopted and were comparatively small: less than 0.4 mhartree. Therefore, the use of larger basis set did not deteriorate the effectiveness of the method, unless diffuse functions are added. The issue on the diffuse functions in the DC method should be resolved elsewhere.

Table 3.4. Basis-set dependence of DC and conventional UMP2 total energies (in hartree) of the polyene cation $C_{40}H_{42}^{+}$ with $n_{\mathrm{b}}^{\mathrm{corr}} = 8$. DC scheme was only applied to the correlation calculation after the standard UHF calculation. Energy deviations from conventional UMP2 results are shown in parentheses in mhartree.

Basis set	E_{UMP2} [hartree]	$E_{\mathrm{DC\text{-}UMP2}}$ [hartree]	(diff.) [mhartree]
STO-6G	–1536.939441	–1536.939354	(+0.087)
6-31G	–1541.380225	–1541.380017	(+0.208)
6-31G**	–1543.817715	–1543.817507	(+0.209)
6-311G	–1541.873844	–1541.873865	(–0.021)
6-311G**	–1544.368953	–1544.368583	(+0.370)

3.4. Conclusion

In the previous Chapter, the author has introduced the unrestricted orbital scheme to the DC-SCF method for treating large open-shell systems. In this Chapter, the author developed the correlated open-shell treatment in the framework of the DC-based correlation method. The DC-UMP2 method was implemented into the GAMESS program and was assessed in calculations of the spin- and charge-delocalized polyene cation systems $C_nH_{n+2}^+$. Numerical assessments revealed that the DC-UMP2 method has the advantageous features of the closed-shell DC-MP2 method: the correlation energy errors are generally small achieving the chemical accuracy and are controllable with the buffer size, the CPU time scales quasi-linearly with respect to the system size, and the required memory size becomes constant.

In the recent computer architecture, the development of an efficient parallelization is important as well as acceleration on a single core. Because the correlation energy of a subsystem is evaluated independently of the other subsystems in the DC-MP2 method, straightforward parallelization over subsystems will enhance the parallel efficiency in DC-MP2 calculation. In the case of closed-shell systems, the DC-MP2 code applied to the GDDI was developed in order to achieve a two-level hierarchical parallelization under the collaboration with Katouda and Nagase [51]. The use of this parallelization scheme as well as the development of the individual MP2 algorithm that is appropriate for the recent computer architecture will extend the applicability of the DC-(U)MP2 method to huge systems, including nano magnetic materials, carbon materials, metalloenzymes, and heme proteins.

References

1. C. Møller, M. S. Plesset, Phys. Rev. 46 (1934) 618.
2. P. Pulay, S. Saebø, Theor. Chim. Acta. 69 (1986) 357.
3. S. Saebø, P. Pulay, Annu. Rev. Phys. Chem. 44 (1993) 213.
4. S. Saebø, P. Pulay, J. Chem. Phys. 115 (2001) 3975.
5. M. Schütz, G. Hetzer, H. J. Werner, J. Chem. Phys. 111 (1999) 5691.
6. P. E. Maslen, M. Head-Gordon, Chem. Phys. Lett. 283 (1998) 102.
7. I. M. B. Nielsen, C. L. Janssen, J. Chem. Theory Comput. 3 (2007) 71.
8. J. Almlöf, Chem. Phys. Lett. 183 (1991) 319.
9. M. Häser, Theor. Chim. Acta. 87 (1993) 147.
10. P. Y. Ayala, G. E. Scuseria, J. Chem. Phys. 110 (1999) 3660.
11. G. E. Scuseria, P. Y. Ayala, J. Chem. Phys. 111 (1999) 8330.
12. D. S. Lambrecht, B. Doser, C. Ochsenfeld, J. Chem. Phys. 123 (2005) 184102.
13. P. R. Surján, Chem. Phys. Lett. 406 (2005) 318.
14. M. Kobayashi, H. Nakai, Chem. Phys. Lett. 420 (2006) 250.
15. B. Doser, D. S. Lambrecht, J. Kussmann, C. Ochsenfeld, J. Chem. Phys. 130 (2009) 064107.
16. M. Feyereisen, G. Fitzgerald, A. Komornicki, Chem. Phys. Lett. 208 (1993) 359.
17. A. P. Rendell, T. J. Lee, J. Chem. Phys. 101 (1994) 400.
18. H. Koch, A. Sánchez de Merás, T. B. Pedersen, J. Chem. Phys. 118 (2003) 9481.
19. T. B. Pedersen, A. M. J. Sánchez de Merás, H. Koch, J. Chem. Phys. 120 (2004) 8887.
20. D. G. Fedorov, K. Kitaura, J. Chem. Phys. 121 (2004) 2483.
21. Y. Mochizuki, S. Koikegami, T. Nakano, S. Amari, K. Kitaura, Chem. Phys. Lett. 396 (2004) 473.
22. T. Ishikawa, K. Kuwata, Chem. Phys. Lett. 474 (2009) 195.
23. Y. Okiyama, T. Nakano, K. Yamashita, Y. Mochizuki, N. Taguchi, Chem. Phys. Lett. 490 (2010) 84.
24. K. Baku, S. R. Gadre, J. Comput. Chem. 24 (2003) 484.
25. V. Ganesh, R. K. Dongare, P. Balanarayan, S. R. Gadre, J. Chem. Phys. 125 (2006) 104109.
26. A. P. Rahalkar, M. Katouda, S. R. Gadre, S. Nagase, J. Comput. Chem. 31 (2010) 2405.
27. J. Friedrich, M. Dolg, J. Chem. Phys. 129 (2008) 244105.
28. J. Friedrich, M. Dolg, J. Chem. Theory Comput 5 (2009) 287.
29. M. Kobayashi, T. Akama, H. Nakai, J. Chem. Phys. 125 (2006) 204106.

30. M. Kobayashi, Y. Imamura, H. Nakai, J. Chem. Phys. 127 (2007) 074103.
31. M. Kobayashi, H. Nakai, Int. J. Quantum Chem. 109 (2009) 2227.
32. K. Ishimura, P. Pulay, S. Nagase, J. Comput. Chem. 27 (2006) 407.
33. K. Ishimura, P. Pulay, S. Nagase, J. Comput. Chem. 28 (2007) 2034.
34. M. Katouda, S. Nagase, Int. J. Quantum Chem. 109 (2009) 2121.
35. M. Katouda, S. Nagase J. Chem. Phys. 133 (2010) 184103.
36. M.W. Schmidt, K. K. Baldridge, J. A. Boatz, S. T. Elbert, M. S. Gordon, J. H. Jensen, S. Koseki, N. Matsunaga, K. A. Nguyen, S. Su, T. L. Windus, M. Dupuis, J. A. Montgomery, Jr., J. Comput. Chem. 14 (1993) 1347.
37. D. G. Fedorov, K. Kitaura, J. Phys. Chem. A 111 (2007) 6904.
38. M. Kobayashi, T. Akama, H. Nakai, J. Comput. Chem. Jpn. 8 (2009) 1.
39. M. Kobayashi, H. Nakai Divide-and-conquer approaches to quantum chemistry: Theory and implientation. In Papadopoulos MG, Zalesny R, Mezey PG, Leszczynski J (eds) Linear-scaling techniques in computational chemistry and physics. Springer, Berlin, (2011) pp 97–127.
40. W. Yang, Phys. Rev. Lett. 66 (1991) 1438.
41. W. Yang, T. S. Lee, J. Chem. Phys. 103 (1995) 5674.
42. T. Akama, M. Kobayashi, H. Nakai, J. Comput. Chem. 28 (2007) 2003.
43. T. Akama, A. Fujii, M. Kobayashi, H. Nakai, Mol. Phys. 105 (2007) 2799.
44. M. Kobayashi, T. Kunisada, T. Akama, D. Sakura, H. Nakai, J. Chem. Phys. 134 (2011) 034105.
45. T. Touma, M. Kobayashi, H. Nakai, Chem. Phys. Lett. 485 (2010) 247.
46. T. Touma, M. Kobayashi, H. Nakai, Theor. Chem. Acc. 130 (2011) 701.
47. X. He, K. M. Merz Jr, J. Chem. Theory Comput. 6 (2010) 405.
48. M. Kobayashi, H. Nakai, J. Chem. Phys. 129 (2008) 044103.
49. M. Kobayashi, H. Nakai, J. Chem. Phys. 131 (2009) 114108.
50. H. Nakai, Chem. Phys. Lett. 363 (2002) 73.
51. M. Katouda, M. Kobayashi, H. Nakai, S. Nagase, J. Comput. Chem. 32 (2011) 2756.
52. M. Kobayashi, T. Yoshikawa, H. Nakai, Chem. Phys. Lett. 500 (2010) 172.
53. S. R. Pruitt, D. G. Fedorov, K. Kitaura, M. S. Gordon, J. Chem. Theory Comput. 6 (2010) 1.
54. Advance/BioStation version 3.2, Advance Soft, Tokyo.
55. J. Korchowiec, F. L. Gu, Y. Aoki, Int. J. Quantum Chem. 105 (2005) 875.
56. Y. Orimoto, F. L. Gu, J. Korchowiec, A. Imamura, Y. Aoki, Theor. Chem. Acc. 125 (2010) 493.
57. J. Friedrich, M. Hanrath, M. Dolg, J. Phys. Chem. A 112 (2008) 8762.

58. H. B. Schlegel, J. Chem. Phys. 84 (1986) 4530.
59. A. I. Krylov, J. Chem. Phys. 113 (200) 6052.
60. P. C. Hariharan, J. A. Pople, Theor. Chim. Acta. 28 (1973) 213.
61. W. J. Hehre, R. F. Stewart, J. A. Pople, J. Chem. Phys. 51 (1969) 2657.
62. W. J. Hehre, R. Ditchfield, J. A. Pople, J. Chem. Phys. 56 (1972) 2257.
63. K. Raghava-chari, J. S. Binkley, R. Seeger, J. A. Pople, J. Chem. Phys. 72 (1980) 650.

Part II

Linear-Scaling Divide-and-Conquer Method for Excited-State Calculation

Chapter 4
Divide-and-Conquer Symmetry Adapted Cluster Method: Synergistic Effect of Subsystem Fragmentation and Configuration Selection

4.1. Introduction

In the field of quantum chemistry, the cluster expansion of the wavefunction provides accurate ground-state theories, including a series of CC [1,2] and SAC [3,4] methods. They also give a good starting point to excited-state calculations by means of the LR theory, yielding the SACCI [5–7], CC-LR [8,9], and the EOM-CC [2,10] methods. Several theoretical and practical differences exist between the CC and SAC methods, although they adopt the similar wavefunction structures. A notable advantage of the practical SAC implementation over CC one is that the amplitude of each configuration contributing to the focusing state is estimated *a priori* and the configurations of which great contributions are expected are only involved in the wavefunction. This configuration selection significantly reduces the computational cost of the cluster expansion and makes the SAC/SACCI methods applicable to wide varieties of systems. On the contrary, the reduction of the configurations leads to less inclusion of the total correlation energy. Its efficient implementation has been completed using the direct algorithm [11] and been distributed as a part of Gaussian program package [12]. To further diminish its computational cost, Nakatsuji and coworkers developed the fragmentation-based acceleration approach, called the giant SAC/SACCI method [13].

There have been many other fragmentation-based approaches that have realized the low-scaling computation of the cluster expansion methods. Several examples are the FMO method [14–16], the incremental correlation scheme [17,18], the natural linear-scaled CC [19,20], and the molecular tailoring approach [21–23], which are all capable of performing CC calculations with single, double, and partial triple excitations such as CCSD(T) [24] and CCSDT-3 [25] models. The author has also developed the fragmentation-based linear-scaling methods based on the DC method. The DC method for density functional theory was firstly proposed by Yang and coworkers [26,27]. Nakai research has assessed the DC method in HF calculations of closed- [28–31] and open-shell [32,33] systems, and applied it to the static and dynamic (hyper)polarizability calculations [34–36]. Furthermore, Nakai research has extended to electron correlation methods: the MP2 [37–39] and CC theories [40,41] with the

assistance of the EDA [42]. Unlike the other fragmentation-based method, the DC method requires no artificial prediction related to the positions of the spin and/or charge because the distribution of electrons in the system under consideration is uniformly settled by the common Fermi level. It enables the accurate treatment of large π-conjugated systems. In recent years, the groups of Bettens and Gadre have assessed its effectiveness in calculations of beta carotene and other conjugated systems by other fragmentation-based method [43,44].

In this Chapter, the author implemented the DC method into the SAC program, employing the configuration selection. The present DC-SAC method is expected to be computationally less demanding than the DC-CC method, since the cost of the SAC calculation of each fragment is lower than that of the CC one. Moreover, the author found that the subsystem fragmentation in the DC method can reduce the loss in the correlation energy by the configuration selection. The organization of this Chapter is as follows. Section 4.2 presents the theoretical aspects of the present DC-SAC method after brief summaries of the DC-HF and standard SAC theories. The performance of this combined method is numerically assessed in Section 4.3. Conclusion will follow as Section 4.4.

4.2. Theory

4.2.1. SAC method

For the closed-shell HF single determinant Φ_0, the SAC expansion for a totally symmetric singlet ground state is expressed as

$$\Psi_{\mathrm{SAC}} = \left(\hat{S}\right)\Phi_0 \tag{4.1}$$

$\hat{S}$ represents a symmetry-adapted single and double excitation operators as

$$\hat{S} = \hat{S}_{\mathrm{S}} + \hat{S}_{\mathrm{D}} = \sum_{i}^{\mathrm{occ}}\sum_{a}^{\mathrm{vir}} \qquad \sum_{i,j}^{\mathrm{occ}}\sum_{a,b}^{\mathrm{vir}}\left(c_{ij,ab}\hat{S}_{ij,ab} + d_{ij,ab}\hat{R}_{ij,ab}\right), \tag{4.2}$$

where

$$\hat{S}_{i,a} = \left(a^{\dagger}_{a\alpha}a_{i\alpha} + a^{\dagger}_{a\beta}a_{i\beta}\right)\Big/\sqrt{2}, \tag{4.3}$$

$$\hat{S}_{ij,ab} = \left(a^{\dagger}_{a\alpha}a_{i\alpha}a^{\dagger}_{b\beta}a_{j\beta} + a^{\dagger}_{a\beta}a_{i\beta}a^{\dagger}_{b\alpha}a_{j\alpha} + a^{\dagger}_{a\alpha}a_{i\alpha}a^{\dagger}_{b\beta}a_{j\beta} + a^{\dagger}_{a\beta}a_{i\beta}a^{\dagger}_{b\alpha}a_{j\alpha}\right)\Big/4, \tag{4.4}$$

$$\begin{aligned}\hat{R}_{ij,ab} = \big(&2a^{\dagger}_{a\alpha}a_{i\alpha}a^{\dagger}_{b\alpha}a_{j\alpha} + 2a^{\dagger}_{a\beta}a_{i\beta}a^{\dagger}_{b\beta}a_{j\beta} + a^{\dagger}_{a\alpha}a_{i\alpha}a^{\dagger}_{b\beta}a_{j\beta} + a^{\dagger}_{a\beta}a_{i\beta}a^{\dagger}_{b\alpha}a_{j\alpha} \\ &- a^{\dagger}_{b\alpha}a_{i\alpha}a^{\dagger}_{a\beta}a_{j\beta} - a^{\dagger}_{b\beta}a_{i\beta}a^{\dagger}_{a\alpha}a_{j\alpha}\big)\Big/4\sqrt{3}.\end{aligned} \tag{4.5}$$

Here, subscripts $\{i, j\}$ and $\{a, b\}$ refer to occupied and virtual orbitals, and $a_{q\sigma}$ and $a^{\dagger}_{q\sigma}$ represent the annihilation and creation operators for spatial orbital q of σ spin, respectively. The expansion coefficients $c_{i,a}$, $c_{ij,ab}$, and $d_{ij,ab}$ are determined by solving the nonvariational equation

$$\left\langle \Phi_0 \middle| \hat{H} - E_{\mathrm{SAC}} \middle| \Psi_{\mathrm{SAC}} \right\rangle = 0, \tag{4.6}$$

where $\hat{H}$ and E_{SAC} are the Hamiltonian and the SAC energy composed of the HF energy, E_{HF}, and the SAC correlation energy, ΔE_{SAC}. The SAC correlation energy can be calculated with the two-electron integral notation as follows

$$\Delta E_{\mathrm{SAC}} = \langle ij|ab\rangle\left(2c_{i,a}c_{j,b} - c_{i,b}c_{j,a} + c_{ij,ab} + \sqrt{3}d_{ij,ab}\right). \tag{4.7}$$

The SAC method introduces the perturbative configuration selection for reducing computational time. Namely, the double excitation operators $\hat{S}_{\mu} \in \left\{\hat{S}_{ij,ab}, \hat{R}_{ij,ab}\right\}$ whose second-order contribution to the energy E_{μ}, given in Eq. (4.8), is greater than a given threshold, λ_{g} hartree, are only included in the cluster expansion.

$$E_\mu = \frac{\left|H_{0\mu}\right|^2}{H_{\mu\mu} - H_{00}}, \quad H_{\mu\nu} = \left\langle \Phi_\mu \middle| \hat{H} \middle| \Phi_\nu \right\rangle . \tag{4.8}$$

4.2.2. DC-SAC method

In the DC-based correlation theory, the total correlation energy is estimated by summing up correlation energies corresponding to individual subsystems. The author extends this strategy to the SAC theory:

$$\Delta E_{\text{DC-SAC}} = \sum_{s}^{\text{subsystem}} \Delta E^s_{\text{SAC}} . \tag{4.9}$$

Here, the SAC correlation energy of subsystem *s* is estimated using subsystem orbitals, which are constructed in the localization region, containing not only the central region but also the buffer region. While the buffer regions overlap in several subsystems, the central ones are disjoint each other. To avoid double counting, the SAC correlation energies corresponding to the central regions should be estimated. Thus, the author applies the philosophy of EDA [42] to the SAC correlation energy representation as follows:

$$\Delta E^s_{\text{DC-SAC}} = \sum_{i,j}^{\text{occ}} \sum_{a,b}^{\text{vir}} \sum_{\mu \in \mathbf{S}(s)} C^{s*}_{\mu i} \left\langle \mu j^s \middle| a^s b^s \right\rangle \left(2c^s_{i,a} c^s_{j,b} - c^s_{i,b} c^s_{j,a} + c^s_{ij,ab} + \sqrt{3} d^s_{ij,ab} \right) . \tag{4.10}$$

In the present calculations, the author utilizes the dual-buffer DC scheme [36] where the buffer size used for the DC-based correlation calculation is set to be smaller than that for the DC-HF calculation. In the dual-buffer scheme, the orbitals used in the DC-SAC calculation are obtained by diagonalizing the small submatrices of the converged Fock matrix that is obtained by the preceding standard HF calculation, or DC-HF calculation with larger buffer size. This scheme reduces the computational efforts for the evaluation of the SAC energy with keeping its accuracy. Although the computational cost for the standard HF calculation scales as $O(n^3)$, it is usually significantly less than the cost for the SAC calculation.

4.3. Numerical assessment

The present DC-SAC method was first assessed by calculations of one-dimensional hydrogen fluoride $(HF)_n$ clusters (Fig. 4.1) by comparing the findings with the standard SAC results. Individual HF molecule was adopted as a central region and several adjacent HF molecules were treated as the corresponding buffer region. The size of buffer region is denoted by n_b^{corr} that indicates the number of HF molecules in each left or right buffer region. Applying the dual-buffer DC correlation scheme, only the electron correlation was treated with the DC approach after the standard HF calculations for clearly showing that the errors reported in the present study originate only in the present DC-SAC approximation.

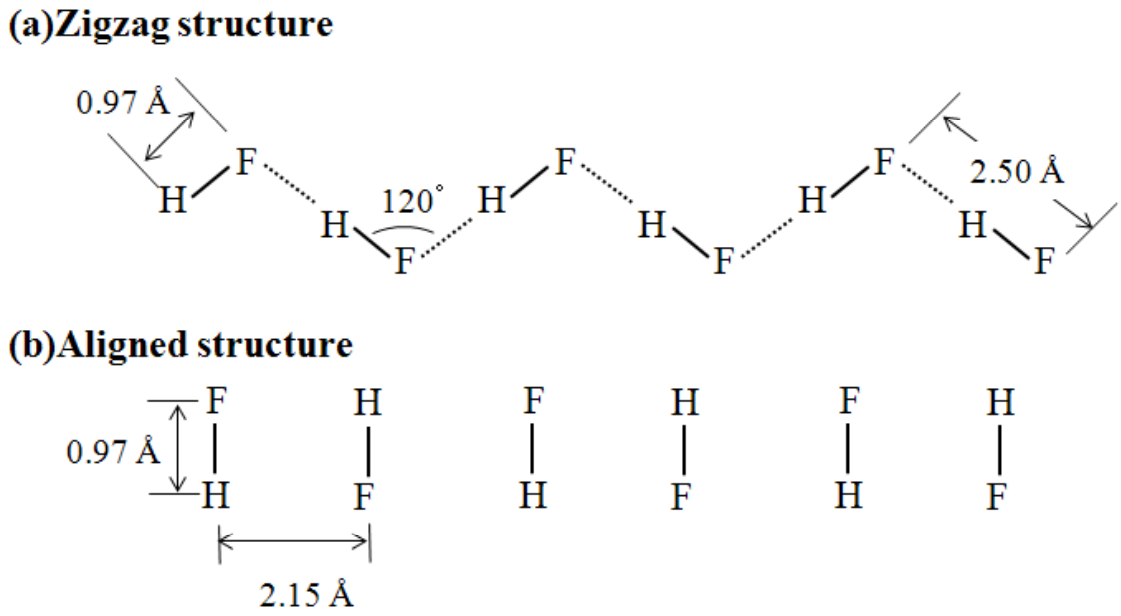

Fig. 4.1. (a) Zigzag and (b) aligned structures of hydrogen fluoride clusters $(HF)_6$

Fig. 4.2 shows the buffer-size (n_b^{corr}) dependence of the correlation energies obtained by the DC-SAC and DC-CCSD calculations of a zigzag hydrogen fluoride cluster $(HF)_6$ (Fig. 4.1(a)) with the 4-31G basis set [47]. The energies are tabulated in Table 4.1. In the SAC method, $\lambda_g = 0$ represents that no configuration selection is adopted. The energy errors from the standard SAC ($\lambda_g = 0$) or CCSD result are given in parentheses. The buffer size was varied in DC calculations. Note that in the DC calculations with $n_b^{corr} = 5$, each localization region contains the entire system. The standard CCSD and SAC energies are given with dashed lines in Fig. 4.2.

The CCSD and SAC ($\lambda_g = 0$) energy errors from the standard results rapidly converge to 0 and are less than 1.5 mhartree even with $n_b^{corr} = 5$. Adopting the configuration selection decreases the standard SAC correlation energies by 161 and 77 mhartree for $\lambda_g = 10^{-5}$ and 10^{-6}, respectively. However, in the DC-SAC calculations, the decrease in the SAC correlation energy becomes smaller as the buffer size decreases.

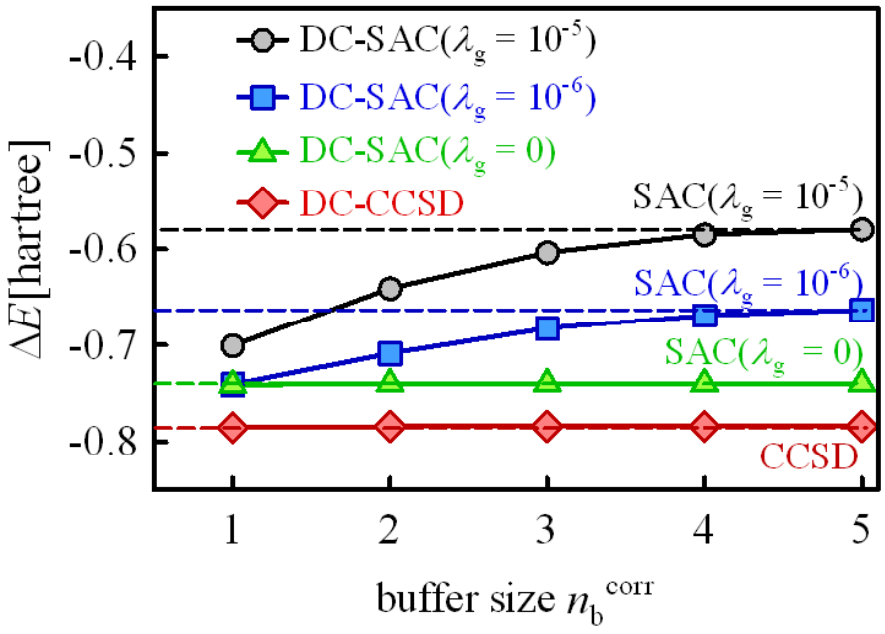

Fig. 4.2. Buffer-size dependence of the correlation energies (in eV) obtained by the DC and standard SAC and CCSD calculations of a zigzag hydrogen fluoride cluster $(HF)_6$ with the 4-31G basis set.

Table 4.1. Correlation buffer-size dependence of the DC-SAC and CCSD correlation energies (in hartree) of a zigzag hydrogen fluoride cluster $(HF)_6$ with the 4-31G basis set. Energy deviations from standard SAC with $\lambda_g = 0$ and CCSD results are shown in parentheses in mhartree.

n_b^{corr}	ΔE_{SAC} [hartree]						ΔE_{CCSD}	
	$\lambda_g = 10^{-5}$		$\lambda_g = 10^{-6}$		$\lambda_g = 0$		[hartree]	
1	–0.70038	(+39.71)	–0.74091	(–0.82)	–0.74122	(–1.13)	–0.78535	(–1.52)
2	–0.64035	(+99.74)	–0.70871	(+31.37)	–0.74009	(0.00)	–0.78384	(0.00)
3	–0.60340	(+136.69)	–0.68220	(+57.89)	–0.74009	(0.00)	–0.78383	(0.00)
4	–0.58468	(+155.41)	–0.66892	(+71.17)	–0.74009	(0.00)	–0.78384	(0.00)
5	–0.57915	(+160.93)	–0.66268	(+77.40)	–0.74009	(0.00)	–0.78384	(0.00)
standard	–0.57915	(+160.93)	–0.66268	(+77.40)	–0.74009	-	–0.78384	-

Table 4.2. Threshold λ_g dependence of the number of the configuration N_{conf} and SAC correlation energy (in hartree) with or without the localized orbitals of 1, 3-butadiene with the 6-31G** basis set.

λ_g	Canonical		Boys	
	N_{conf}	ΔE_{SAC} [hartree]	N_{conf}	ΔE_{SAC} [hartree]
10^{-3}	850	–0.05617	861	–0.12143
10^{-4}	1744	–0.20202	1589	–0.29835
10^{-5}	11041	–0.37956	5458	–0.43269
10^{-6}	40477	–0.47873	20079	–0.50192
10^{-7}	71177	–0.50767	55506	–0.52775
10^{-8}	86098	–0.51531	119625	–0.53622
0	341550	–0.51889	341550	–0.54045

This paradoxal result is derived from the localization of orbitals used in the SAC calculation, which was addressed by Toyota et al. [48] in the standard SAC calculations with the localized orbitals. Table 4.2 lists the threshold λ_g dependence of the correlation energy of 1,3-butadiene obtained by SAC/6-31G** [49] calculations with canonical and Boys localized orbitals [50], together with the number of the configurations satisfying $|E_\mu| > \lambda_g$. Comparing the results with the same λ_g, the correlation energy obtained with the Boys localized orbitals is commonly larger (in absolute value) than that with the

canonical orbitals, although the numbers of configurations with the Boys localized orbitals are less than those with the canonical orbitals, except for $\lambda_g = 10^{-3}$ and 10^{-8}. It means that the use of the Boys localized orbitals screens the important contribution more effectively than using the canonical orbitals. The subsystem orbitals constructed in a small localization region are expected to bring about the similar effect. In DC-SAC calculations, it was found that the deterioration in the accuracy accompanying with the reduction of the buffer size compensates with the improvement in the configuration selection by the localization of orbitals.

In the SAC method, the total energy is significantly affected by the configuration selection. Therefore, the relative energy will provide a good indicator to judge its performance. Table 4.3 shows the threshold dependence of standard and DC-SAC energies of zigzag and aligned $(HF)_6$ clusters with the 4-31G basis set. The reorganization energies ($E_R = E_{aligned} - E_{zigzag}$) of the zigzag cluster from the aligned structure are listed together in kcal/mol. The differences from the standard SAC ($\lambda_g = 0$) results are shown in parentheses. In DC calculations, the correlation buffer size was fixed at $n_b^{corr} = 1$. Compared with the standard SAC ($\lambda_g = 0$) result, the reorganization energy errors introduced by the configuration selection are non-negligible, 16 and 5 kcal/mol for $\lambda_g = 10^{-5}$ and 10^{-6}, respectively, which are considerably larger than 0.6 kcal/mol of the error by the DC method. However, the combination of the DC method with the configuration selection behaves significantly better, i.e., the error is less than 2 kcal/mol even with $\lambda_g = 10^{-5}$.

Table 4.3. Threshold λ_g dependence of the total energies (in hartee) of zigzag and aligned $(HF)_6$ clusters obtained by the DC and standard SAC calculations with the 4-31G basis set. The reorganization energy (E_R) of the zigzag cluster from the aligned structure is also given. Energy deviations from the standard SAC result with $\lambda_g = 0$ are shown in parentheses.

Method		Aligned [hartree]	(diff.) [mhartree]	Zigzag [hartree]	(diff.) [mhartree]	E_R [kcal/mol]	(diff.) [kcal/mol]
DC-SAC	$\lambda_g = 10^{-5}$	–600.049311	(+45.252)	–600.100018	(+42.503)	31.820	(+1.726)
	$\lambda_g = 10^{-6}$	–600.090627	(+3.936)	–600.140550	(+1.971)	31.327	(+1.233)
	$\lambda_g = 0$	–600.093888	(+0.675)	–600.140861	(+1.660)	29.476	(–0.618)
SAC	$\lambda_g = 10^{-5}$	–599.905104	(+189.459)	–599.978796	(+163.725)	46.242	(+16.148)
	$\lambda_g = 10^{-6}$	–600.006691	(+87.872)	–600.062323	(+80.198)	34.909	(+4.815)
	$\lambda_g = 0$	–600.094563	-	–600.142521	-	30.094	-

The efficiency of the DC-SAC method was examined by measuring the CPU time. An Intel Xeon X5365 (3.00 GHz) processor was used on a single core. Fig. 4.3 shows the system-size dependence of the CPU times for the DC and standard SAC calculations of $(HF)_n$ zigzag clusters (n = 2, 4, 6, and 10). The threshold λ_g was set to be 10^{-6}. In DC calculations, the correlation buffer size was fixed at $n_b^{corr} = 1$. Note that the time for the HF calculation preceding the SAC calculation is not included because the author utilized the standard full SCF procedure for both DC and standard calculations. The CPU times of the DC-SAC method are shorter than those of the standard SAC method except for n = 2, where all localization regions in the DC calculation contain the entire system. According to the scaling analysis by the double-logarithmic plot, the times scale with $O(n^{4.3})$ and $O(n^{1.4})$ for standard and DC-SAC calculations, respectively.

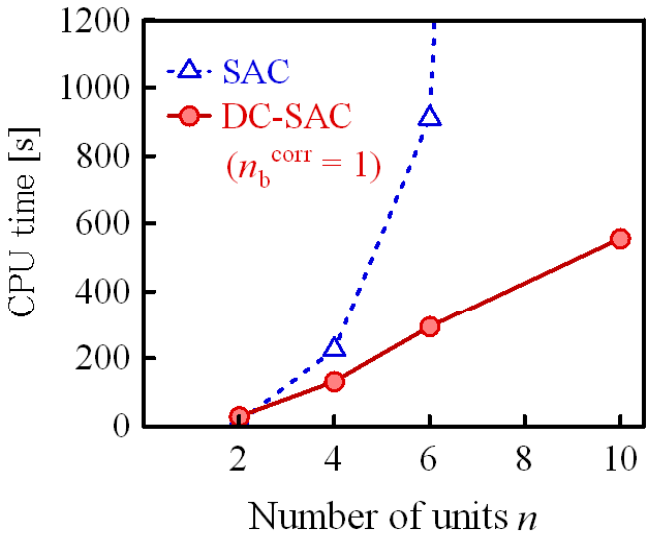

Fig. 4.3. System-size dependence of the CPU times (in s) for the DC and standard SAC calculations of zigzag $(HF)_n$ clusters with the 4-31G basis set. An Intel Xeon X5365 (3.00 GHz) processor was used on a single core.

Finally, the DC-SAC method was assessed by the calculations of π-conjugated systems, namely bond alternating (BA) and uniform (U) polyene chains, $C_{10}H_{12}$ (Fig. 4.4). In the BA chain, all C=C, C−C, and C−H lengths were fixed to 1.37, 1.43, and 1.10 Å, while the all C−C lengths in the U chain were 1.40 Å. In the DC calculation, C_2H_2 (or C_2H_3 for the edges) was adopted as a central region and left-and-right one C_2H_2 (or C_2H_3) units were treated as the corresponding buffer region. Again, the author adopted the dual-buffer scheme, i.e., only the electron correlation was treated with the DC approach after the standard HF calculations. 6-31G [51], 6-31G*[49], 6-31G** [49], 6-311G [52], and 6-311G* [52] basis sets were adopted. Table 4.4 shows the basis-set dependence of the reorganization energy ($E_R = E_U - E_{BA}$) of the BA chain from the U chain. The differences from the standard CCSD energies are shown in parentheses. Although the buffer size adopted in the DC-SAC calculation was small, the calculated reorganization energies well reproduced the standard CCSD results with $\lambda_g = 10^{-6}$: the deviations are less than 1.7 kcal/mol. The combination of the DC method with the SAC configuration selection is effective even in calculations of delocalized π-conjugated systems.

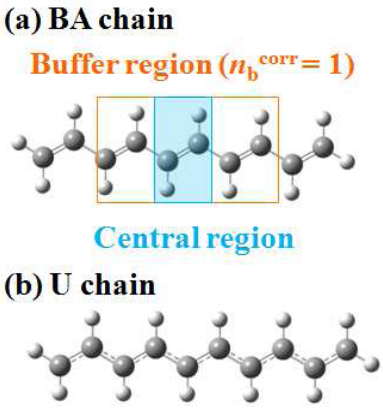

Fig. 4.4. (a) Bond alternating (BA) and (b) uniform (U) polyene chain $C_{10}H_{12}$. The schematic of the central and buffer regions in the DC calculation with $n_b^{corr} = 1$ is also shown.

Table 4.4. Basis-set dependence of the reorganization energy (in kcal/mol) of the BA polyene chain $C_{10}H_{12}$ from the U chain calculated with the DC-SAC and standard CCSD methods. Energy deviations from the standard CCSD results are shown in parentheses.

Basis set	DC-SAC [kcal/mol]				CCSD
	$\lambda_g = 10^{-5}$		$\lambda_g = 10^{-6}$		[kcal/mol]
6-31G	6.887	(–0.694)	8.161	(+0.580)	7.581
6-31G*	7.270	(–1.673)	8.832	(+0.889)	8.943
6-31G**	5.060	(–3.977)	7.431	(–1.606)	9.037
6-311G	10.664	(+2.775)	8.839	(+0.951)	7.888
6-311G*	3.072	(–5.840)	7.519	(–1.392)	8.912

4.4. Conclusion

In this Chapter, the author developed the DC-based SAC method. In the numerical assessments of the present method, the author confirmed that the local orbitals constructed in the DC method improve the performance of the configuration selection in the SAC calculations, as well as that the computational time scales quasi-linearly with respect to the system size.

As mentioned in the section 4.1 the SAC wavefunction provides a good starting point to excited-state calculations, called the SACCI method. The extension of the present DC-SAC method to the SACCI theory will open up excited-state calculations of huge systems such as biomolecules and nanomaterials.

References

1. T. D. Crawford, H. F. Schaefer, III, In *Reviews in Computational Chemistry*; Wiley: New York, 2000; Vol. 14, pp 33-136.
2. I. Shavitt, R. J. Bartlett, *Many-Body Methods in Chemistry and Physics*; Cambridge University Press: Cambridge, 2009.
3. H. Nakatsuji, K. Hirao, J. Chem. Phys. 68 (1978) 2053.
4. H. Nakatsuji, Chem. Phys. Lett. 59 (1978) 362.
5. H. Nakatsuji, Chem. Phys. Lett. 67 (1979) 329.
6. H. Nakatsuji, Chem. Phys. Lett. 67 (1979) 334.
7. M. Ehara, J. Hasegawa, H. Nakatsuji, In *Theory and Applications of Computational Chemistry: The First Forty Years*; C. E. Dykstra, G. Frenking, K. S. Kim, G. E. Scuseria, Eds.; Elsevier: Amsterdam, 2005; pp 1099-1141.
8. H. J. Monkhorst, Int. J. Quantum Chem. Symp. 11 (1977) 421.
9. D. Mukherjee, P. K. Mukherjee, Chem. Phys. 39 (1979) 325.
10. H. Sekino, R. J. Bartlett, Int. J. Quantum Chem. Symp. 18 (1984) 255.
11. R. Cammi, R. Fukuda, M. Ehara, H. Nakatsuji, J. Chem. Phys. 133 (2010) 024104.
12. M. Frisch, G. W. Trucks, H. B. Schlegel, G. E. Scuseria, M. A. Robb, J. R. Cheeseman, G. Scalmani, V. Barone, B. Mennucci, G. A. Petersson, H. Nakatsuji, M. Caricato, X. Li, H. P. Hratchian, A. F. Izmaylov, J. Bloino, G. Zheng, J. L. Sonnenberg, M. Hada, M. Ehara, K. Toyota, R. Fukuda, J. Hasegawa, M. Ishida, T. Nakajima, Y. Honda, O. Kitao, H. Nakai, T. Vreven, J. A. Montgomery Jr., J. E. Peralta, F. Ogliaro, M. Bearpark, J. J. Heyd, E. Brothers, K. N. Kudin, V. N. Staroverov, R. Kobayashi, J. Normand, K. Raghavachari, A. Rendell, J. C. Burant, S. S. Iyengar, J. Tomasi, M. Cossi, N. Rega, J. M. Millam, M. Klene, J. E. Knox, J. Cross, V. Bakken, C. Adamo, J. Jaramillo, R. Gomperts, R. E. Stratmann, O. Yazyev, A. J. Austin, R. Cammi, C. Pomelli, J. W. Ochterski, R. L. Martin, K. Morokuma, V. G. Zakrzewski, G. A. Voth, P. Salvador, J. J. Dannenberg, S. Dapprich, A. D. Daniels, O. Farkas, J. B. Foresman, V. J. Ortiz, J. Cioslowki, D. J. Fox, Gaussian 09, Revision A.02; Gaussian, Inc: Wallingford, CT, 2009.
13. H. Nakatsuji, T. Miyahara, R. Fukuda, J. Chem. Phys. 126 (2007) 084104.
14. K. Kitaura, E. Ikeo, T. Asada, T. Nakano, M. Uebayasi, Chem. Phys. Lett. 313 (1999) 701.
15. D. G. Fedorov, K. Kitaura, J. Chem. Phys. 123 (2005) 134103.
16. D. G. Fedorov, K. Kitaura, Eds.; *The Fragment Molecular Orbital Method*; CRC Press: Boca Raton, 2009.

17. H. Stool, Chem. Phys. Lett. 191 (1992) 548.
18. J. Friedrich, M. Dolg, J. Chem. Theory Comput. 5 (2009) 287.
19. N. Flocke, R. J. Bartlett, J. Chem. Phys. 121 (2004) 10935.
20. T. F. Hughes, N. Flocke, R. J. Bartlett, J. Phys. Chem. A 112 (2008) 5994.
21. S. Gadre, R. N. Shirsat, A. C. Limaye, J. Phys. Chem. 98 (1994) 9165.
22. S. R. Gadre, K. V. Jovan Jose, A. P. Rahalkar, J. Chem. Sci. 122 (2010) 47.
23. A. P. Rahalkar, B. K. Mishra, V. Ramanathan, S. R. Gadre, Theor. Chem. Acc. 130 (2011) 491.
24. K. Raghavachari, G. W. Trucks, J. A. Pople, M. Head-Gordon, Chem. Phys. Lett. 157 (1989) 479.
25. M. Urban, J. Noga, S. J. Cole, R. J. Bartlett, J. Chem. Phys. 83 (1985) 4041.
26. W. Yang, Phys. Rev. Lett. 66 (1991) 1438.
27. W. Yang, T. S. Lee, J. Chem. Phys. 103 (1995) 5674.
28. T. Akama, M. Kobayashi, H. Nakai, J. Comput. Chem. 28 (2007) 2003.
29. T. Akama, A. Fujii, M. Kobayashi, H. Nakai, Mol. Phys. 105 (2007) 2799.
30. T. Akama, M. Kobayashi, H. Nakai, Int. J. Quantum Chem. 109 (2009) 2706.
31. M. Kobayashi, T. Kunisada, D. Sakura, H. Nakai, J. Chem. Phys. 134 (2011) 034105.
32. M. Kobayashi, T. Yoshikawa, H. Nakai, Chem. Phys. Lett. 500 (2010) 172.
33. M. Kobayashi, H. Nakai, Phys. Chem. Chem. Phys. 14 (2012) 7629.
34. T. Touma, M. Kobayashi, H. Nakai, Chem. Phys. Lett. 485 (2010) 247.
35. T. Touma, M. Kobayashi, H. Nakai, Theor. Chem. Acc. 130 (2011) 701.
36. M. Kobayashi, T. Touma, H. Nakai, J. Chem. Phys. 136 (2012) 084108.
37. M. Kobayashi, T. Akama, H. Nakai, J. Chem. Phys. 125 (2006) 204106.
38. M. Kobayashi, Y. Imamura, H. Nakai, J. Chem. Phys. 127 (2007) 074103.
39. T. Yoshikawa, M. Kobayashi, H. Nakai, Theor. Chem. Acc. 130 (2011) 411.
40. M. Kobayashi, H. Nakai, J. Chem. Phys. 129 (2008) 044103
41. M. Kobayashi, H. Nakai, J. Chem. Phys. 131 (2009) 114108.
42. H. Nakai, Chem. Phys. Lett. 363 (2002) 73.
43. H.-A.Le, H.-J. Tan, J. F. Ouyang, R. P. A. Bettens, J. Chem. Theory Comput. 8 (2011) 469.
44. S. D. Yeole, S. R. Gadre, J. Phys. Chem. A 115 (2011) 12769.
45. M. Kobayashi, H. Nakai, In *Linear-scaling Techniques in Computational Chemistry and Physics*; Papadopoulos, M. G.; Zalesny, R.;Mezey, P. G.; Leszczynski, J., Eds.;Springer: Berlin, 2011; pp 97-127.
46. M. Kobayashi, H. Nakai, Int. J. Quantum Chem. 27 (2006) 407.

47. R. Ditchfield, W. J. Hehre, J. A. Pople, J. Chem. Phys. 54 (1971) 724.
48. K. Toyota, M. Ehara, H. Nakatsuji, Chem. Phys. Lett. 356 (2002) 1.
49. P. C. Hariharan, J. A. Pople, Theor. Chim. Acta. 28 (1973) 213.
50. S. F. Boys, Rev. Mod. Phys. 32 (1960) 306.
51. W. J. Hehre, R. Eitchfield, J. A. Pople, J. Chem. Phys. 56 (1972) 2257.
52. R. Krishnan, J. S. Binkley, R. Seeger, J. A. Pople, J. Chem. Phys. 72 (1980) 650.

Chapter 5
Divide-and-Conquer Symmetry Adapted Cluster Configuration Interaction Method

5.1. Introduction

Many biochemical systems, such as rhodopsin in vertebrate eyes and PYP in purple bacteria, are photoactive. The absorption wavelength of a photoactive protein is affected by the photon-absorbing pigment as well as interactions between the pigment and its neighboring residues, which cause red- or blue-shifts from the excitation energy of the free pigment. Although computational predictions of the shifts in biomolecular systems are in demand, quantum chemical excited-state calculations of large biomolecules are difficult because of the high computational cost.

Recently, excited-state calculations based on SACCI theory [1,2], which is one of the most accurate excited-state theories, have successfully explained and predicted the mechanisms of photoactive biomolecular systems using an active-site model selected from the system [3,4]. Although active-site models work reasonably well for many biomolecular systems, their calculations overlook interactions between the pigment and outside residues, which may be important for accurate evaluation of the excitation energy.

Several fragmentation-based approaches that enable to reduce the computation cost for excited-state theories have been reported. For example, the FMO method was applied to the CIS [5–7] and TDDFT [8,9]. The density-fragment interaction approach [10] enables large-scale TDDFT calculations by describing the interactions between many quantum-mechanical fragments. AO-based TDDFT [11,12] enables linear-scaling computation via prescreening techniques and sparse matrix algebra. There are several approaches that utilize localized MOs, including fragment-localized MO TDDFT [13], local-excitation-approximation CIS and TDDFT [14], and the local CIS approach [15]. Also, linear-scaling TDDFT with a local density matrix [16,17] has been proposed. A giant SACCI scheme [18] was proposed for the excited-state calculation of molecular crystals.

The author developed fragmentation-based linear-scaling methods for ground-state theories based on the DC method. The DC method for density functional theory was first proposed by Yang and coworkers [19,20]. Unlike other fragmentation-based methods, the DC method requires no artificial prediction related to the positions of the spin and/or charge, because the distribution of electrons in the

system under consideration is uniformly settled by the common Fermi level; this enables accurate treatment of large π-conjugated systems. The author assessed the DC method using HF calculations of closed-shell [21–24] and open-shell [25,26] systems, and applied it to static and dynamic (hyper)polarizability calculations [27–29]. Furthermore, the author extended the DC method to electron-correlation theories, such as the MP2 [30-34], CC [35,36], and SAC theories [37] with the assistance of EDA [38]. Energy gradient schemes for the DC method were also recently established [39,40]. For biomolecules, the author successfully elucidated interactions between viral peptides and their inhibitors [41,42]. Although the application of the DC method to excited-state theories is desired for the accurate prediction of the excitation energies of biomolecules, it has not yet been attempted.

In this chapter, the author extended the DC methodology to excited-state theories, specifically CIS, TDDFT, and SACCI. In these DC-based excited-state theories, the subsystem that contains the chromophore or pigment is first selected as the excitation subsystem. Excited-state calculation of the ES yields the excitation energies, which includes the effect of factors outside the ES through the electrostatic potential. The organization of this chapter is as follows: Section 5.2 presents the theoretical aspects of the DC-CIS, DC-TDDFT, and DC-SAC/SACCI methods after a brief summary of the DC-SCF method; section 5.3 shows the numerical applications of the present scheme via calculations of formaldehyde in water, conjugated aldehyde, and PYP; and section 5.4 comprises the conclusion.

5.2. Theory

5.2.1. DC-based excited-state theory

The DC-based excited-state theory utilizes the subsystem MOs obtained from the preceding DC-HF or DC-DFT calculations. Following the ground-state DC calculation, the subsystem that includes the pigment is selected as the ES. The excited-state wavefunctions of the ES are constructed from its MOs, which can be classified as either occupied or virtual via the Fermi level.

5.2.1.1. DC-CIS/TDDFT

In the DC-CIS method, the n^{th} excited-state wavefunction in the ES is expressed as the linear combination of singly-excited determinants, $\left|\Phi_{i,a}^{\text{ES}}\right\rangle$, from the reference determinant, $\left|\Phi_{0}^{\text{ES}}\right\rangle$, as follows:

$$\left|\Psi_{\text{CIS}}^{\text{ES}(n)}\right\rangle = \sum_{i}^{\text{occ(ES)}} \sum_{a}^{\text{vir(ES)}} d_{i,a}^{\text{ES}(n)} \left|\Phi_{i,a}^{\text{ES}}\right\rangle . \tag{5.1}$$

Here, $\left|\Phi_{0}^{\text{ES}}\right\rangle$ is defined as the Slater determinant of the occupied MOs in the ES that have lower energies than the Fermi level determined via the DC-HF calculation; the subscripts $\{i, j\}$ and $\{a, b\}$ refer to occupied and virtual MOs, respectively. Hereafter, $\boldsymbol{d}^{\text{ES}(n)}$is referred to as the CI coefficients that are deduced as the normalized eigenvectors of the Hamiltonian matrix, $\boldsymbol{A}^{\text{ES}}$, which is expressed using the two-electron integral notation, as follows:

$$A_{ia,jb}^{\text{ES}} = \left\langle \boldsymbol{\Phi}_{i,a}^{\text{ES}} \middle| \hat{H} - E_0^{\text{ES}} \middle| \boldsymbol{\Phi}_{j,b}^{\text{ES}} \right\rangle = \left(\varepsilon_a^{\text{ES}} - \varepsilon_i^{\text{ES}}\right)\delta_{ij}\delta_{ab} - \left\langle j^{\text{ES}} a^{\text{ES}} \middle\| i^{\text{ES}} b^{\text{ES}} \right\rangle . \tag{5.2}$$

where $E_0^{\text{ES}} = \left\langle \boldsymbol{\Phi}_0^{\text{ES}} \middle| \hat{H} \middle| \boldsymbol{\Phi}_0^{\text{ES}} \right\rangle$. The excitation energies, $\omega^{\text{ES}(n)}$, can be obtained from the eigenvalues of the matrix.

The dual-buffer DC scheme, which was first proposed in the post-HF electron-correlation calculation [33] can be applied to the excited-state calculation. In the scheme, the Fock matrix, $\boldsymbol{F}$, is first constructed from the density matrix converged with the preceding conventional HF calculation. Then, the Roothaan-Hall equation for the ES is solved to construct the MOs used for the excited-state calculation, as follows:

$$\boldsymbol{F}^{\text{ES}} \boldsymbol{C}_p^{\text{ES}} = \varepsilon_p^{\text{ES}} \boldsymbol{S}^{\text{ES}} \boldsymbol{C}_p^{\text{ES}} . \tag{5.3}$$

The Fermi level that separates the occupied and virtual MOs is determined as the middle of the highest occupied and lowest virtual MO energies that obtained from the preceding conventional HF calculation. Alternatively, it can also be defined by

calculating the MOs in all the subsystems.

The procedure can also be applied to TDDFT calculations by substituting the CIS Hamiltonian of (5.2) with that of TDDFT [43].

5.2.1.2. DC-SAC/SACCI

In the previous Chapter, the author proposed the ground-state DC-SAC theory. Here, the author briefly summarizes the conventional SAC/SACCI and DC-SAC theories and present the DC-SACCI method.

The SAC expansion for a totally symmetric singlet ground state is expressed as

$$\left|\Psi_{\mathrm{SAC}}\right\rangle = \exp\left(\hat{S}\right)\left|\Phi_0\right\rangle, \tag{5.4}$$

where $\hat{S}$ represents the symmetry-adapted single and double excitation operators, as Eqs. (4.2)–(4.5). The SAC expansion coefficients, i.e., $c_{i,a}$, $c_{ij,ab}$, and $c'_{ij,ab}$, are determined by solving the following non-variational equations:

$$\left\langle \Phi_0 \left| \hat{R}_K \left(\hat{H} - E_{\mathrm{SAC}} \right) \right| \Psi_{\mathrm{SAC}} \right\rangle = 0, \tag{5.5}$$

Here E_{SAC} is the SAC energy, which comprises the HF energy, E_{HF}, and the SAC correlation energy, ΔE_{SAC}. The SAC correlation energy can be calculated as

$$\Delta E_{\mathrm{SAC}} = \left\langle ij \middle| ab \right\rangle \left(2c_{i,a}c_{j,b} - c_{i,b}c_{j,a} + c_{ij,ab} + \sqrt{3}c'_{ij,ab} \right), \tag{5.6}$$

Based on the SAC wavefunction, the SACCI expansion for the *n*-th excited state is expressed as

$$\left|\Psi^{(n)}_{\mathrm{SACCI}}\right\rangle = \sum_K d^{(n)}_K \hat{P}\hat{R}^{\dagger}_K \left|\Psi_{\mathrm{SAC}}\right\rangle, \tag{5.7}$$

where $\{\hat{R}^{\dagger}_K\}$ represents a set of excitations, each of which generates a basis for the target state. $\hat{P} = 1 - \left|\Psi_{\mathrm{SAC}}\right\rangle\left\langle\Psi_{\mathrm{SAC}}\right|$ is the projection operator that projects out the ground-state wavefunction. The SACCI coefficients, $d^{(n)}_K$, and the excitation energies, $\omega^{(n)}$, are calculated by solving the non-variational equation, as follows:

$$\left\langle \Phi_0 \left| \hat{R}_K \left(\hat{H} - E_{\mathrm{SAC}} - \omega^{(n)} \right) \right| \Psi^{(n)}_{\mathrm{SACCI}} \right\rangle = 0. \tag{5.8}$$

In the DC-SAC/SACCI theory, the ground-state SAC wavefunction for the ES is

$$\left|\Psi^{\mathrm{ES}}_{\mathrm{SAC}}\right\rangle = \exp\left(\hat{S}^{\mathrm{ES}}\right)\left|\Phi^{\mathrm{ES}}_0\right\rangle, \tag{5.9}$$

where $\hat{S}^{\mathrm{ES}}$ represents the symmetry-adapted single and double excitation operator from the reference determinant, $\left|\Phi^{\mathrm{ES}}_0\right\rangle$, in the ES, as follows:

$$\hat{S}^{\mathrm{ES}} = \sum_{i}^{\mathrm{occ(ES)}} \sum_{a}^{\mathrm{vir(ES)}} \hat{S}_{i,a}^{\mathrm{ES}} + \sum_{i,j}^{\mathrm{occ(ES)}} \sum_{a,b}^{\mathrm{vir(ES)}} \left(c_{ij,ab}^{\mathrm{ES}} \hat{S}_{ij,ab}^{\mathrm{ES}} + c'^{\mathrm{ES}}_{ij,ab} \hat{S}'^{\mathrm{ES}}_{ij,ab} \right). \tag{5.10}$$

$\hat{S}_{i,a}^{\mathrm{ES}}$, $\hat{S}_{ij,ab}^{\mathrm{ES}}$, and $\hat{S}'^{\mathrm{ES}}_{ij,ab}$ are the same as in Eqs. (4.3)–(4.4), but are defined using the annihilation and creation operators of the MOs in the ES, i.e., $a_{p\sigma}^{\mathrm{ES}}$ and $a_{p\sigma}^{\mathrm{ES}\dagger}$. The expansion coefficients are determined by solving the non-variational equation for the ES, as follows:

$$\left\langle \Phi_0^{\mathrm{ES}} \middle| \hat{H} - E_{\mathrm{SAC}}^{\mathrm{ES}} \middle| \Psi_{\mathrm{SAC}}^{\mathrm{ES}} \right\rangle = 0, \tag{5.11}$$

Here, $E_{\mathrm{SAC}}^{\mathrm{ES}}$ is the SAC energy of the ES. Note that $E_{\mathrm{SAC}}^{\mathrm{ES}}$ is not the ground-state DC-SAC energy that was presented in the previous chapter; instead, it is defined as

$$\begin{aligned} E_{\mathrm{SAC}}^{\mathrm{ES}} &= E_0^{\mathrm{ES}} + \Delta E_{\mathrm{SAC}}^{\mathrm{ES}} \\ &= E_0^{\mathrm{ES}} + \left\langle i^{\mathrm{ES}} j^{\mathrm{ES}} \middle| a^{\mathrm{ES}} b^{\mathrm{ES}} \right\rangle \left(2c_{i,a}^{\mathrm{ES}} c_{j,b}^{\mathrm{ES}} - c_{i,b}^{\mathrm{ES}} c_{j,a}^{\mathrm{ES}} + c_{ij,ab}^{\mathrm{ES}} + \sqrt{3} c'^{\mathrm{ES}}_{ij,ab} \right). \end{aligned} \tag{5.12}$$

Based on the SAC wavefunction in the ES, the DC-SACCI expansion for the *n*-th excited state is

$$\left| \Psi_{\mathrm{SACCI}}^{\mathrm{ES}(n)} \right\rangle = \sum_{K} d_K^{\mathrm{ES}(n)} \hat{P}^{\mathrm{ES}} \hat{R}_K^{\mathrm{ES}\dagger} \left| \Psi_{\mathrm{SAC}}^{\mathrm{ES}} \right\rangle, \tag{5.13}$$

where $\{ \hat{R}_K^{\mathrm{ES}\dagger} \}$ represents a set of excitations, each of which generates a basis for the target state in the ES. $\hat{P}^{\mathrm{ES}} = 1 - \left| \Psi_{\mathrm{SAC}}^{\mathrm{ES}} \right\rangle \left\langle \Psi_{\mathrm{SAC}}^{\mathrm{ES}} \right|$ is the projection operator that projects out the ground-state wavefunction in the ES. The DC-SACCI coefficients, $d_K^{\mathrm{ES}(n)}$, and excitation energies, $\omega^{\mathrm{ES}(n)}$, are calculated by solving the following non-variational equation:

$$\left\langle \Phi_0^{\mathrm{ES}} \middle| \hat{R}_{\mathrm{K}}^{\mathrm{ES}} \left(\hat{H} - E_{\mathrm{SAC}}^{\mathrm{ES}} - \omega^{\mathrm{ES}(n)} \right) \middle| \Psi_{\mathrm{SACCI}}^{\mathrm{ES}(n)} \right\rangle = 0. \tag{5.14}$$

5.3. Numerical assessment

In this section, the performance of the presented DC-CIS, DC-TDDFT, and DC- SACCI methods are numerically assessed by comparing the results with those of conventional CIS, TDDFT, and SACCI calculations. All CIS and TDDFT calculations were performed using a modified version of the GAMESS program [44], while SACCI calculations were performed using a modified version of the Gaussian09 program [45]. In the section, only the excited-state calculations were performed using the DC scheme following conventional calculation of the ground states. All chemical core orbitals are frozen during the excited-state calculations. For the TDDFT calculations, the LCBLYP exchange-correlation functional [46-48] was adopted unless otherwise noted. The perturbation selection with a Level Three threshold in the Gaussian program was used for the SACCI calculations.

5.3.1. Formaldehyde in water

The author first assessed the DC-based excited-state theory through calculations of the n–π^* and σ–π^* excitation energies of a formaldehyde molecule in 16 explicit water molecules, i.e., H_2CO + $16H_2O$. The ES comprises the H_2CO molecule and atoms in the union of spheres centered at the four atoms of the H_2CO molecule within radius r_{ex}. Fig. 5.1 and Table 5.1 show the ES-size (r_{ex}) dependence of the n–π^* and σ–π^*excitation energies obtained via DC-based and conventional CIS, TDDFT, and SACCI calculations of H_2CO + $16H_2O$ using the 6-31G** basis set [49]. The conventional CIS, TDDFT, and SACCI excitation energies are shown as dashed lines in Fig. 5.1. In Table 5.1, deviations of the DC excitation energies from those derived from conventional methods are presented in parentheses. For all three methods, the DC-based excited-state calculations showed 0.16 eV or less absolute-value excitation-energy deviations for the ES size of $r_{ex} \geq 3.0$Å. The excitation energy deviations converge to zero when the ES is enlarged in the DC method, while the n–π^* excitation energy deviation for the DC-TDDFT calculation with r_{ex} = 2.0 Å is smaller than that with r_{ex} = 2.5 Å; this is probably due to error cancelation.

Next, the author increased the number of water molecules in the calculation to investigate convergence with respect to the size of the solvation sphere. Here, the ES size was fixed as r_{ex} = 3.5 Å, and the 6-31G** basis set was adopted. Table 5.2 shows the dependence of the n–π^* excitation energy of H_2CO on the number of explicit water molecules; the gas-phase results calculated using conventional methods are also included, and the deviations of the calculated excitation energies from experimental

values are presented in parentheses. Empirically, the n–π^* excitation energy of formaldehyde in the gas phase is 4.07 eV [50], while that in water is 4.28 eV [51]; this indicates a blue-shift of 0.21 eV. In the gas-phase calculations, the SACCI method gives the best result with a deviation of 0.12 eV. The deviation of the results of the TDDFT method is also small (0.15 eV), while the deviation of the results of the CIS method is relatively large. By increasing the number of water molecules, the excitation energies determined using the CIS and SACCI methods decrease gradually and approach the experimental value, while it increases gradually for TDDFT method. The SACCI result for $H_2CO + 61H_2O$ gives the closest excitation energy (4.41 eV) to the empirical value with a shift from the gas-phase results of 0.22 eV.

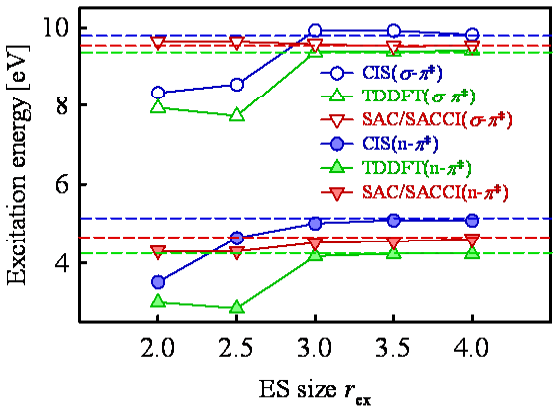

Fig. 5.1. ES-size (r_{ex}) dependence of the excitation energies (in eV) obtained via DC-based CIS, TDDFT, and SACCI calculations of the $H_2CO + 16H_2O$ system using the 6-31G** basis set. The conventional CIS, TDDFT, and SACCI excitation energies are indicated by dashed lines

Table 5.1. ES-size (r_{ex}) dependence of the n–π * and σ–π* excitation energies (in eV) obtained via DC-based CIS, TDDFT, and SACCI calculations of a H_2CO + $16H_2O$ system using the 6-31G** basis set. The results of conventional CIS, TDDFT, and SACCI methods are shown at the bottom. The deviations of the calculated excitation energies from the conventional results are shown in parentheses.

	CIS				TDDFT				SACCI			
r_{ex}[Å]	n–π* [eV]	(diff.) [eV]	σ–π* [eV]	(diff.) [eV]	n–π* [eV]	(diff.) [eV]	σ–π* [eV]	(diff.) [eV]	n–π* [eV]	(diff.) [eV]	σ–π* [eV]	(diff.) [eV]
2.0	3.51	(−1.58)	8.34	(−1.44)	3.00	(−1.24)	7.93	(−1.49)	4.31	(−0.37)	9.65	(+0.15)
2.5	4.64	(−0.46)	8.55	(−1.23)	2.84	(−1.40)	7.72	(−1.70)	4.30	(−0.38)	9.65	(+0.15)
3.0	5.01	(−0.09)	9.92	(+0.15)	4.17	(−0.07)	9.38	(−0.05)	4.52	(−0.16)	9.58	(+0.08)
3.5	5.09	(−0.00)	9.92	(+0.15)	4.23	(−0.01)	9.40	(−0.03)	4.55	(−0.13)	9.53	(+0.03)
4.0	5.09	(−0.01)	9.82	(+0.04)	4.23	(−0.01)	9.41	(−0.01)	4.61	(−0.07)	9.54	(+0.04)
Conv.	5.10		9.78		4.24		9.42		4.68		9.50	

Table 5.2. Dependence of the n–π^* excitation energy (in eV) of H_2CO on the number of explicit water molecules (n). The gas-phase results (n = 0) obtained via conventional calculations are also presented. The deviations of the calculated excitation energies from experimental values are presented in parentheses.

	$H_2CO + nH_2O$									
	n = 0 [eV]	(diff.) [eV]	n = 16 [eV]	(diff.) [eV]	n = 20 [eV]	(diff.) [eV]	n = 39 [eV]	(diff.) [eV]	n = 61 [eV]	(diff.) [eV]
CIS	4.58	(+0.51)	5.09	(+0.81)	5.03	(+0.75)	5.01	(+0.73)	4.92	(+0.65)
TDDFT	3.92	(−0.15)	4.23	(−0.05)	4.43	(+0.15)	4.46	(+0.18)	4.61	(+0.33)
SACCI	4.19	(+0.12)	4.55	(+0.27)	4.46	(+0.18)	4.45	(+0.17)	4.41	(+0.13)
Exptl.	4.07[a]		4.28[b]		4.28[b]		4.28[b]		4.28[b]	

[a]Ref. [50]. [b]Ref. [51]

5.3.2. Conjugated aldehyde

Next, the author applied the present methods to the n–π^* excited-state calculations of a conjugated aldehyde, i.e., $C_{16}H_{17}CHO$, which is depicted in Fig. 5.2. The C=C, C–C, C=O, and C–H lengths are fixed at 1.36, 1.46, 1.22, and 1.10 Å, respectively, and all atoms lie in the same plane. The ES consists of the terminal CHO group and several C_2H_2 units, the number of which is denoted by n_{ex} (see Fig. 5.2, which shows an example for $n_{ex} = 2$). Fig. 5.3 shows the ES-size (n_{ex}) dependence of the n–π^* excitation energies obtained via DC-based CIS, TDDFT, and SACCI calculations of $C_{16}H_{17}CHO$ using the 6-31G** basis set. The conventional CIS, TDDFT, and SACCI excitation energies are represented by dashed lines in Fig. 5.3. For all three methods, the results of the DC-based excited-state calculations show smooth convergence with respect to the ES size and deviate by an absolute value of 0.12 eV or less for the ES size of $n_{ex} \geq 3$.

The efficiencies of the DC-based CIS and TDDFT methods were determined by measuring the CPU time required using an Intel Xeon X5470 (3.33 GHz) processor on a single core. For diagonalization of the Hamiltonian matrix, the Davidson algorithm was adopted; the maximum number of expansion vectors used by the solver's iterations was set at 50. The lowest 10 singlet excited states were obtained. Table 5.3 shows the CPU times for the DC-based CIS and TDDFT calculations of $C_{16}H_{17}CHO$ using the 6-31G** basis set. The times required for the preceding HF or DFT calculation are not included. It was confirmed that the DC method drastically reduces the required computational time with only a slight energy error.

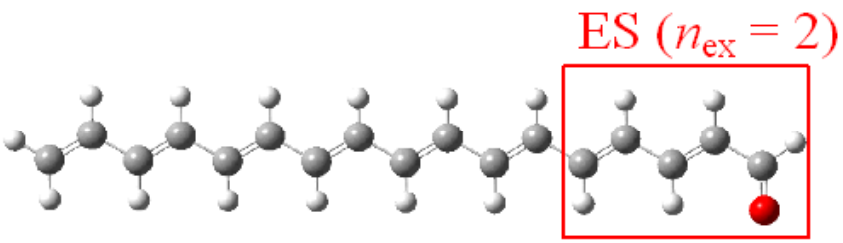

Fig. 5.2. Structure of the $C_{16}H_{17}CHO$ molecule and schematic of the ES in the DC calculation.

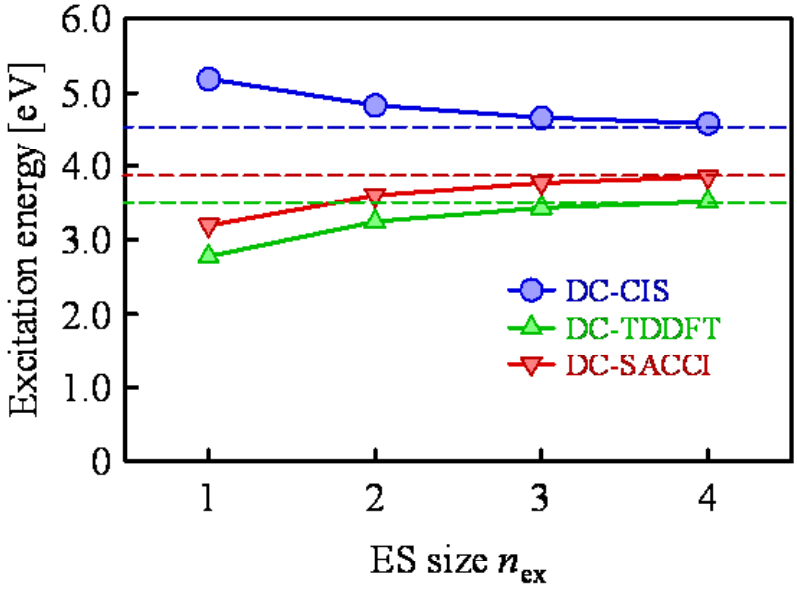

Fig. 5.3. ES-size (n_{ex}) dependence of the excitation energies (in eV) obtained via DC-based CIS, TDDFT, and SACCI calculations of $C_{16}H_{17}CHO$ using the 6-31G** basis set. The conventional CIS, TDDFT, and SACCI excitation energies are indicated by dashed lines.

Table 5.3. CPU times (in s) of the DC-CIS and TDDFT calculations of $C_{16}H_{17}CHO$ using the 6-31G** basis set. The times required for the preceding HF or DFT calculation are not included. An Intel Xeon X5470 (3.33 GHz) processor was used on a single core.

n_{ex}	CIS [s]	TDDFT [s]
1	14	114
2	49	402
3	179	1290
4	242	1944
Conv.	708	4530

Table 5.4 shows the basis-set dependence of the n–π^*excitation energies obtained via the DC-CIS, TDDFT, and SACCI calculations. 6-31G [52], 6-311G [53], 6-311G** [53], cc-pVDZ [54], and cc-pVTZ [54] basis sets were adopted in addition to the 6-31G** set; note that conventional SACCI with cc-pVTZ could not be performed due to the large computational cost. The ES size was fixed at $n_{ex} = 3$. In Table 5.4, the deviations of the DC excitation energies from those obtained using conventional methods are presented in parentheses. The energy deviations do not show a significant dependence on the adopted basis set and, at a maximum of 0.15 eV, are quite small. Therefore, the use of a larger basis set does not reduce the effectiveness of the present method.

Table 5.4. Basis-set dependence of the n–π^* excitation energy (in eV) of $C_{16}H_{17}CHO$ obtained using DC- and conventional CIS, TDDFT, and SACCI calculations. The energy deviations from the conventional results are shown in parentheses. The ES size of n_{ex} = 3 was adopted for the DC calculations.

Basis set	CIS [eV]	DC-CIS [eV]	(diff) [eV]	TDDFT [eV]	DC-TDDFT [eV]	(diff.) [eV]	SACCI [eV]	DC-SACCI [eV]	(diff.) [eV]
6-31G	4.41	4.34	(−0.07)	3.48	3.39	(−0.09)	3.85	3.82	(−0.03)
6-31G**	4.64	4.58	(−0.06)	3.53	3.50	(−0.03)	3.87	3.76	(−0.11)
6-311G	4.41	4.31	(−0.10)	3.48	3.63	(+0.15)	3.84	3.80	(−0.04)
6-311G**	4.61	4.49	(−0.12)	3.51	3.49	(−0.02)	3.79	3.69	(−0.10)
cc-pVDZ	4.59	4.51	(−0.08)	3.49	3.46	(−0.02)	3.84	3.76	(−0.08)
cc-pVTZ	4.63	4.58	(−0.06)	3.50	3.46	(−0.04)	–	3.78	–

Finally, the accuracies of the DC-TDDFT excitation energies obtained using typical functionals, i.e., SVWN [55,56], BLYP [56,57], B3LYP [57], and LCBLYP, were examined. Table 5.5 shows the functional dependence of the n–π* excitation energies obtained via DC (with n_{ex} = 3) and conventional TDDFT methods. The excitation energies obtained using pure DFT functionals (i.e., SVWN and BLYP) were lower than those obtained using wavefunction-based correlated SACCI, i.e., 3.87 and 3.76 eV by the conventional and DC-SACCI methods, respectively (Table 5.4). The hybrid DFT functionals (i.e., B3LYP and LCBLYP) provided closer results. The results from TDHF, which are listed in Table 5.5, overestimated the excitation energy as compared to the SACCI results. For all the functionals, the DC-TDDFT calculations reproduced the excitation energies obtained using the conventional method within 0.15 eV.

Table 5.5. DFT functional dependence of the n–π* excitation energy (in eV) of a conjugated aldehyde $C_{16}H_{17}CHO$ obtained using DC- and conventional TDDFT methods. The deviations of the energies from the conventional results are shown in parentheses. An ES size of n_{ex} = 3 was adopted for the DC calculations.

Functional	Conv. [eV]	DC [eV]	(diff.) [eV]
SVWN	2.15	2.30	(+0.15)
BLYP	2.31	2.45	(+0.14)
B3LYP	3.17	3.15	(−0.03)
LCBLYP	3.53	3.50	(−0.03)
HF	4.48	4.42	(−0.06)

5.3.3. Photoactive yellow protein

The present method was applied to PYP; the crystal structure, which is depicted in Fig. 5.4(a), is registered under the accession code 2PHY in the Protein Data Bank [58]. PYP is a photoreceptor protein that comprises 125 amino acid residues and a pigment, which is deprotonated 4-hydroxycinnamic acid (HC4) linked with Cys69 by a thioester bond. PYP shows an absorption maximum at 446 nm (2.78 eV); corresponds to the lowest π–π* excitation energy from HOMO to LUMO), while the absorption maximum of HC4 is at 284 nm (4.37 eV) in water [59]. Thus, a large red-shift of 1.59 eV is induced via binding of the pigment to the apoprotein. It is possible to separately quantify the effects of the pigment on the absorption maximum using quantum chemical calculations. The author theoretically investigated the red-shift in PYP using DC-CIS,

TDDFT, and SACCI calculations. Accordingly, the author constructed three models of the system, of which the schematic is depicted in Fig. 5.4(b): (i) The AC model, which comprises HC4, Tyr42, Glu46, Thr50, Arg52, and Cys69, and is depicted in blue, (ii) the first coordination sphere (C1) model, which comprises AC, Ala67, Pro68, Phe96, and Thr98, and is depicted in green, and (iii) the entire PYP protein, which is depicted in orange. The 6-31G basis set was adopted for the following calculations.

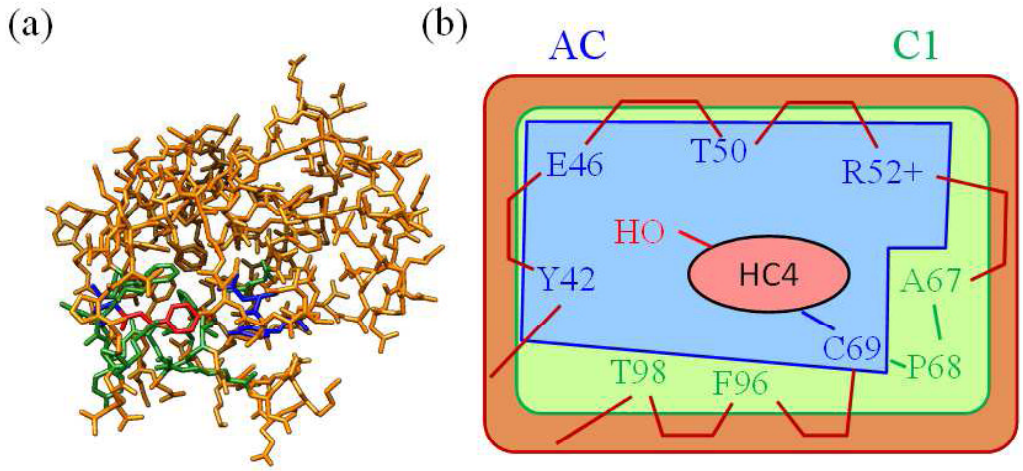

Fig. 5.4. (a) Structure of PYP. (b) Schematic of the three-model systems: (i) AC model [HC4, Tyr42, Glu46, Thr50, Arg52, and Cys69] (blue), (ii) C1 model [AC, Ala67, Pro68, Phe96, and Thr98] (green), and (iii) the entire PYP protein (orange).

First, the author evaluated the π–π^* excitation energy of a HC4 molecule in water solvent. The solvent effect was accounted for using the integral equation formulation of the polarizable continuum model [60]. The excitation energies calculated using the conventional CIS, TDDFT, and SACCI methods are given in Table 5.6 together with the experimental results. The differences between the calculated and experimental excitation energies are presented in parentheses. Although the SACCI method gives the best result, with 0.15 eV deviation from the experimental value, the deviations of the CIS and TDDFT results are also small, i.e., < 0.3 eV.

Table 5.6 shows the excitation energies for the AC model obtained using conventional CIS, TDDFT, and SACCI methods. In contrast to HC4, the excitation-energy results significantly depend on the methodology. Note that all the

excitation energies exhibit red-shifts from those of HC4, which are caused by the formation of the thioester bond with Cys69 and deprotonation of the OH group in HC4. The SACCI method, which gives the lowest excitation energy, still has an excitation-energy deviation of 0.81 eV. Therefore, it is evident that the simple AC model could not sufficiently reproduce the experimental shift; this is due to the lack of interactions with the outside residues.

The author attempted to include the effects of the outside residues by using the ONIOM method [61] with the Gaussian09 program [45]; the method has been widely used for calculating biomolecules in quantum chemistry. The AC model was adopted as the high-level layer where the CIS and TDDFT methods were applied (note that ONIOM-SACCI is not implemented in Gaussian). The other atoms in the PYP system were treated using the universal force field. [62] The calculated and experimental excitation energies are shown in Table 5.6. Although the excitation energies obtained using the ONIOM method are red-shifted from the results of the AC model, they still did not reach the experimental value. The ONIOM method with a classical electrostatic field for the low-layer region also could not reproduce the experimental value.

Table 5.6. Excitation energies (in eV) of the HC4 (4-hydroxycinnamic acid; pigment), AC (active center; HC4, Tyr42, Glu46, Thr50, Arg52, and Cys69), and entire PYP models. The HC4 and AC models were calculated using the conventional method and the PYP model was calculated using the ONIOM scheme. The deviations of the excitation energies from the experimental values are shown in parentheses.

	HC4 [eV]	(diff.) [eV]	AC [eV]	(diff.) [eV]	PYP [eV]	(diff.) [eV]
CIS	4.64	(+0.27)	4.40	(+1.61)	4.33	(+1.55)
TDDFT	4.60	(+0.23)	3.83	(+1.06)	3.38	(+0.60)
SACCI	4.52	(+0.15)	3.59	(+0.81)	–	–
Exptl.	4.37 [a]		2.78 [a]		2.78 [a]	

[a] Ref. [59].

Next, the author performed DC-CIS, TDDFT, and SACCI calculations on the C1 and PYP model systems; the results are given in Table 5.7. The AC region is adopted as the ES. Although the excitation energies of the C1 model are red-shifted from the results for the AC model (Table 5.6), they still do not match the experimental value. However, the results for the whole PYP model with TDDFT and SACCI are close to the experimental results; in particular, the DC-SACCI method reproduces the excitation energy within 0.11 eV. Comparing the DC result with the ONIOM one given in Table 5.6, DC-TDDFT treatment of the entire PYP system leads to additional 0.23 eV shift from the ONIOM-TDDFT excitation energy. Therefore, it was confirmed that the inclusion of the classical electrostatic effects from the outside residues is not enough to reproduce the biochemical excitation shift, but the QM treatment of the whole PYP system using a highly accurate excited-state method is required.

The efficiency of the DC-SACCI method was examined by measuring the CPU time required using an Intel Xeon X5470 (3.33 GHz) processor on a single core. Table 5.8 shows the CPU times for conventional SACCI calculation of the AC model and for DC-SACCI calculations of the C1 and PYP models. The CPU time remained nearly constant because the SACCI calculation was only performed on the same ES region, i.e., the AC region. The SAC/SACCI method introduces the perturbative configuration selection for reducing computational time. The numbers of configurations selected in the ground- and excited-state calculations, N_{gr} and N_{ex}, respectively, are listed in Table 5.8. The number of configurations selected in the calculation of the AC model is larger than those of the C1 and PYP models because ten hydrogen atoms are added at the cleavages of the covalent bonds that are formed when constructing the active-site model. By using DC-SACCI methodology, the author could accelerate the excited-state calculations while maintaining high accuracy.

Table 5.7. Excitation energies (in eV) of C1 (first coordination sphere; AC, Ala67, Pro68, Phe96, and Thr98) and entire PYP models calculated using the DC scheme. The deviations of the excitation energy from the experimental values are shown in parentheses.

	C1 [eV]	(diff.) [eV]	PYP [eV]	(diff) [eV]
CIS	4.22	(+1.44)	4.23	(+1.46)
TDDFT	3.52	(+0.74)	3.15	(+0.37)
SACCI	3.29	(+0.52)	2.89	(+0.11)
Exptl.	2.78		2.78	

Table 5.8. CPU times (in min) for conventional and DC-SACCI calculations of the AC (active center; HC4, Tyr42, Glu46, Thr50, Arg52, and Cys69), C1 (first coordination sphere; AC, Ala67, Pro68, Phe96, and Thr98), and entire PYP models. An Intel Xeon X5470 (3.33 GHz) processor was used on a single core. The numbers of the configurations selected in the ground and excited states, N_{gr} and N_{ex} are listed together.

Model	CPU time [min]	N_{gr}	N_{ex}
AC	897.0	340013	444369
C1	852.6	318392	326815
PYP	662.4	305349	274343

5.4. Conclusion

In the previous Chapter, the author developed the DC-SAC theory as a starting point for highly accurate excited-state calculations. In this Chapter, the author developed the DC-based SACCI theory in conjunction with the DC-based CIS theory and TDDFT. To demonstrate the high accuracy and effectiveness of our approach, the author calculated the excited states of both a formaldehyde molecule in 16 explicit water molecules and a conjugated aldehyde. The excitation energy errors are generally small, indicating that high chemical accuracy is achieved. It was confirmed that the present scheme enabled efficient excited-state calculation of large systems.

To demonstrate the DC-SACCI method, the author calculated the lowest singlet excitation energy of PYP. The obtained value of 2.89 eV is in reasonable agreement with the experimental absorption energy of 2.78 eV.

References

1. H. Nakatsuji, K. Hirao, J. Chem. Phys. 68 (1978) 2053.
2. H. Nakatsuji, Chem. Phys. Lett. 67 (1979) 334.
3. K. Fujimoto, S. Hayashi, J. Hasegawa, H. Nakatsuji, J. Chem. Theory Comput. 3 (2007) 605.
4. N. Nakatani, J. Hasegawa, H. Nakatsuji, J. Am. Chem. Soc. 129 (2007) 8756.
5. Y. Mochizuki, S. Koikegami, S. Amari, K. Segawa, K. Kitaura, T. Nakano, Chem. Phys. Lett. 406 (2005) 283.
6. Y. Mochizuki, K. Tanaka, K. Yamashita, T. Ishikawa, T. Nakano, S. Amari, K. Segawa, T. Murase, H. Tokiwa, M. Sakurai, Theor. Chem. Acc. 117 (2007) 541.
7. J. B. Foresman, M. Head-Gordon, J. A. Pople, M. J. Frisch, J. Phys. Chem. 96 (1992) 135.
8. M. Chiba, D. G. Fedorov, K. Kitaura, J. Chem. Phys. 127 (2007) 104108.
9. E. Runge, E. K. U. Gross, Phys. Rev. Lett. 52 (1984) 997.
10. K. Fujimoto, W. Yang, J. Chem. Phys. 129 (2008) 054102.
11. S. J. A. Gisbergen, C. F. Guerra, E. J. Baerends, J. Comput. Chem. 21 (2000) 1511.
12. S. Coriani, S. Høst, B. Jansik, L. Thøgersen, J. Olsen, P. Jørgensen, S. Reine, F. Pawlowski, T. Helgaker, P. Salek, J. Chem. Phys. 126 (2007) 154108.
13. F. Wu, W. Liu, Y. Zhang, Z. Li, J. Chem. Theory Comput. 7 (2011) 3643.
14. M. Miura, Y. Aoki, J. Comput. Chem. 30 (2009) 2213.
15. Q. Li, Z. Shuai, Synth. Met. 158 (2008) 330.
16. C. Y. Yam, S. Yokojima, G. H. Chen, Phys. Rev. B 68 (2003) 153105.
17. F. Wang, C. Y. Yam, G.-H. Chen, J. Chem. Phys. 126 (2007) 244102.
18. H. Nakatsuji, T. Miyabara, R. Fukuda, J. Chem. Phys. 126 (2007) 084104.
19. W. Yang, Phys. Rev. Lett. 66 (1991) 1438.
20. W. Yang, T. S. Lee, J. Chem. Phys. 103 (1995) 5674.
21. T. Akama, M. Kobayashi, H. Nakai, J. Comput. Chem. 28 (2007) 2003.
22. T. Akama, A. Fujii, M. Kobayashi, H. Nakai, Mol. Phys. 105 (2007) 2799.
23. T. Akama, M. Kobayashi, H. Nakai, Int. J. Quantum Chem. 109 (2009) 2706.
24. M. Kobayashi, H. Nakai, *Linear-Scaling Techniques in Computational Chemistry and Physics: Methods and Applications, Challenges and Advances in Computational Chemistry and Physics* vol. 13; Springer: New York, USA, 2011, pg. 97.
25. M. Kobayashi, T. Yoshikawa, H. Nakai, Chem. Phys. Lett. 500 (2010) 172.
26. M. Kobayashi, H. Nakai, Phys. Chem. Chem. Phys. 14 (2012) 7546.

27. T. Touma, M. Kobayashi, H. Nakai, Chem. Physl. Lett. 485 (2010) 247.
28. T. Touma, M. Kobayashi, H. Nakai, Theor. Chem. Acc. 130 (2011) 701.
29. M. Kobayashi, T. Touma, H. Nakai, J. Chem. Phys. 136 (2012) 084108.
30. M. Kobayashi, T. Akama, H. Nakai, J. Chem. Phys. 125 (2006) 204106.
31. M. Kobayashi, Y. Imamura, H. Nakai, J. Chem. Phys. 127 (2007) 074103.
32. M. Katouda, M. Kobayashi, H. Nakai, S. Nagase, J. Comput. Chem. 32 (2011) 2756.
33. M. Kobayashi, H. Nakai, Int. Quantum Chem. 109 (2009) 2227.
34. T. Yoshikawa, M. Kobayashi, H. Nakai, Theor. Chem. Acc. 130 (2011) 411.
35. M. Kobayashi, H. Nakai, J. Chem. Phys. 129 (2008) 044103.
36. M. Kobayashi, H. Nakai, J. Chem. Phys. 131 (2009) 114108.
37. T. Yoshikawa, M. Kobayashi, H. Nakai, Int. J. Quantum Chem. 113 (2013) 218.
38. H. Nakai, Chem. Phys. Lett. 368 (2002) 73.
39. M. Kobayashi, T. Kunisada, T. Akama, D. Sakura, H. Nakai, J. Chem. Phys. 134 (2011) 034105.
40. M. Kobayashi, H. Nakai, J. Chem. Phys. 138 (2013) 044102.
41. P. Saparpakorn, M. Kobayashi, S. Hannongbua, H. Nakai, Int. J. Quantum Chem. 113 (2013) 510.
42. P. Saparpakorn, M. Kobayashi, H. Nakai, Bull. Chem. Soc. Jpn. 86 (2013) 67.
43. M. E. Casida, *Recent Advances in Density Functional Methods* vol. 1; World Scientific: Singapore, 1998, pg. 155.
44. M.W. Schmidt, K. K. Baldridge, J. A. Boatz, S.T. Elbert, M.S. Gordon, J.H. Jensen, S.Koseki, N. Matsunaga, K.A. Nguyen, S. Su,T.L. Windus,M. Dupuis, J.A. Montgomery Jr., J. Comput. Chem. 14 (1993) 1347.
45. M. Frisch, G. W. Trucks, H. B. Schlegel, G. E. Scuseria, M. A. Robb, J. R. Cheeseman, G. Scalmani, V. Barone, B. Mennucci, G. A. Petersson, H. Nakatsuji, M. Caricato, X. Li, H. P. Hratchian, A. F. Izmaylov, J. Bloino, G. Zheng, J. L. Sonnenberg, M. Hada, M. Ehara, K. Toyota, R. Fukuda, J. Hasegawa, M. Ishida, T. Nakajima, Y. Honda, O. Kitao, H. Nakai, T. Vreven, J. A. Montgomery Jr., J. E. Peralta, F. Ogliaro, M. Bearpark, J. J. Heyd, E. Brothers, K. N. Kudin, V. N. Staroverov, R. Kobayashi, J. Normand, K. Raghavachari, A. Rendell, J. C. Burant, S. S. Iyengar, J. Tomasi, M. Cossi, N. Rega, J. M. Millam, M. Klene, J. E. Knox, J. Cross, V. Bakken, C. Adamo, J. Jaramillo, R. Gomperts, R. E. Stratmann, O. Yazyev, A. J. Austin, R. Cammi, C. Pomelli, J. W. Ochterski, R. L. Martin, K. Morokuma, V. G. Zakrzewski, G. A. Voth, P. Salvador, J. J. Dannenberg, S. Dapprich, A. D. Daniels, O. Farkas, J. B. Foresman, V. J. Ortiz, J. Cioslowki, D. J. Fox, Gaussian 09, Revision A.02; Gaussian, Inc: Wallingford, CT, 2009.

46. A. D. Becke, Phys. Rev. A 38 (1988) 3098.
47. C. Lee, W. Yang, R. G. Parr, Phys. Rev. B 37 (1988) 785.
48. H. Iikura, T. Tsuneda, T. Yanai, K. Hirao, J. Chem. Phys. 115 (2001) 3540.
49. P. C. Hariharan, J. A. Pople, Theor. Chim. Acta 28 (1973) 213.
50. T. M. Nymand, P. Linse, J. Chem. Phys. 112 (2000) 6152.
51. M. B. Rubin, *Higher Excited States of Polyatomic Molecules*, vol. III; Academic press: New York, USA, 1985.
52. W. J. Hehre, R. Ditchfield, J. A. Pople, J. Chem. Phys. 56 (1972) 2257.
53. R. Krishnan, J. S. Binkley, R. Seeger, J. A. Pople, J. Chem. Phys. 72 (1980) 650.
54. T. H. Dunning Jr, J. Chem. Phys. 90 (1989) 1007.
55. S. H. Vosko, L. Wilk, M. Nusair, Can. J. Phys. 58 (1989) 1200.
56. J. C. Slater, Phys. Rev. 81 (1951) 385.
57. P. J. Stephens, F. J. Devlin, C. F. Chablowski, M. J. Frisch, J. Phys. Chem. 98 (1994) 11623.
58. http://www.rcsb.org/
59. M. Yoda, H. Houjou, Y. Inoue, M. Sakurai, J. Phys. Chem. B 105 (2001) 9887.
60. G. Scalmani, M. Frisch, J. Chem. Phys. 124 (2006) 094107.
61. T. Vreven, K. Morokuma, Theor, Chem. Acc. 109 (2003) 125.
62. A. K. Pappe, C. J. Casewit, K. S. Colwell, W. M. Skiff, J. Am. Chem. Soc. 114 (1992) 10024.

Chapter 6
Efficient Pole-Search Algorithm for Dynamic Polarizability toward Alternative Excited-State Calculation

6.1. Introduction

Charge-transfer excitations, where light absorption causes a charge transfer from a donor to an acceptor, play an important role in novel photovoltaic phenomena and many biological reactions. The development of *ab initio* methods that allow for both accurate treatment and low computational cost of charge-transfer excitations is a topic of recent scientific interest. Various acceleration techniques for large-scale molecules have been reported [1–5]. In excited-state theories, most of these techniques are based on multilayer theories, which select one or more active centers and perform the excited-state calculations there. The multilayer theories have been largely successful for treating local excitations. It is difficult to treat delocalized excitations such as spread charge-transfer excitations for large molecules.

One of the solutions to the delocalized excitation problem is to calculate the excited state indirectly from dynamic polarizabilities, as proposed by Roy et al [6]. The frequency-dependent response properties implicitly obtain the information about the electronic excited states. The computational cost of the dynamic polarizability calculations is drastically reduced by using linear-scaling method while maintaining accuracy [7–11]: the cost scales linear. Especially, DC method, originally proposed by Yang et al [12,13], has a wide applicability to systems with delocalized electrons and/or spins. A combination of the DC and the excited-state methods based on dynamic polarizability calculations can deal with large delocalized systems [11,14]. Excited-state methods based on dynamic polarizability calculations are required to develop an efficient algorithm because of the large amount of dynamic poralizability calculations.

In this chapter, the author proposes and assesses an algorithm to perform excited-state calculations with dynamic polarizability calculations. Section 6.2 reviews the relationship between excited state and dynamic polarizability, and proposes a novel scheme for searching the poles of dynamic polarizability. Section 6.3 describes the numerical assessments of the proposed algorithm to determine its accuracy and efficiency. Section 6.4 concludes the discussion.

6.2. Theory and implementation

6.2.1. Relation of excited state and dynamic polarizability

This subsection briefly introduces the excited-state method using dynamic polarizabilities $\alpha(\omega)$ at frequencies ω, which are based on the theory proposed by Roy et al [6]. The polarizability can be expressed by two formulae. First, as a derivative of the total dipole moment d with respect to the external electric field E.

$$\alpha(\omega) = \frac{\partial d}{\partial E}, \tag{1}$$

which is obtained by solving the time-dependent Schrödinger equation under the external perturbation E. Second, as the sum-over-state formula:

$$\alpha(\omega) = \sum_n \frac{f_n}{\omega_n^2 - \omega^2}, \tag{2}$$

where ω_n and f_n are the excitation energy and oscillator strength from the ground state to the n-th excited state, respectively, and n runs all excited states. Around the pole corresponding to the n-th excited state, the dynamic polarizability is approximated as

$$\alpha(\omega) \approx \frac{f_n}{\omega_n^2 - \omega^2} \quad . \tag{3}$$

Thus, the excitation energy ω_n and oscillator strength f_n by two different polarizabilities from Eq. (1) for frequencies ω_{n+} and ω_{n-}, sufficiently close to ω_n, are obtained as:

$$\omega_n = \sqrt{\frac{\alpha(\omega_{n+})\omega_{n+}^2 - \alpha(\omega_{n-})\omega_{n-}^2}{\alpha(\omega_{n+}) - \alpha(\omega_{n-})}}, \tag{4}$$

$$f_n = -\frac{\omega_{n+}^2 - \omega_{n-}^2}{\frac{1}{\alpha(\omega_{n+})} - \frac{1}{\alpha(\omega_{n-})}}. \tag{5}$$

This evaluation is independent of the method of dynamic polarizability calculations for Eq. (1), such as TDCPHF, TDCPDFT, CC-LR.

6.2.2. Pole-search algorithm for dynamic polarizability

In this subsection, the author explains a new algorithm based on the theoretical design of the excited-state calculation by using dynamic polarizabilities. As Eq. (2) shows, the dynamic polarizability monotonically increases with respect to frequency, except when the frequency corresponding to one pole is stepped over. A decrease in polarizability means that at least one excitation state exists between the two frequencies. First, the author calculates dynamic polarizabilities at a constant frequency interval ω_{Int} from Eq. (1). After detecting the regions showing decrease in $\alpha(\omega_{int})$, the poles are searched by the bisection method, which consists of three steps. In Step 1, ω_n and f_n are obtained from the two frequencies $\omega_{\mathrm{n+}}$ and $\omega_{\mathrm{n-}}$ corresponding to the decreasing region. In Step 2, the polarizability at the middle frequency ω' between the two polarizabilities $\alpha(\omega_{\mathrm{n+}})$ and $\alpha(\omega_{\mathrm{n-}})$, is calculated from Eq. (1). In Step 3, ω_n and f_n are estimated by two polarizabilities corresponding to a new decreasing region. Steps 2 and 3 are iterated until ω_n and f_n converge.

When one decreasing region contains multiple poles at a large ω_{Int}, the bisection method would pass over one more poles. Herein, the author discusses the case of two poles in one decreasing region, because the cases of more than two poles can be easily considered as extensions of the two-pole case. All three cases of decreasing regions containing two poles are shown in Figs. 1(a)–(c). The middle frequency ω' exists between the two poles corresponding to the smaller excitation energy E_{ex1} and larger excitation energy E_{ex2}. While the case of Fig. 1(a) detects both E_{ex1} and E_{ex2} from the two decreasing regions, the cases of Figs. 1(b) and (c) detect only E_{ex1} and E_{ex2}, respectively, from the one decreasing region. A subtracting process, which clarifies the influence of the undetected poles, is introduced to detect all the poles. Figs. 2(a)–(c) show the polarizabilities before and after subtracting the contributions for the detected excitations, corresponding to the cases of Figs. 6.1(a)–(c). In the case of Fig. 6.2(a), both detected poles disappear. The cases of Figs. 6.2(b) and (c) detect a new decreasing region for E_{ex2} and E_{ex1}, respectively, by subtracting the contribution for the detected pole.

The scheme of excited-state calculation using dynamic polarizabilities based on the above theoretical design is shown as a flow chart in Fig. 6.3. The details of implementation are as follows. First, the dynamic polarizabilities $\alpha(\omega)$ are calculated at a constant frequency interval ω_{Int}. All decreasing regions for the polarizability are searched for and detected. Next, ω_n and f_n for a new set of decreasing regions, N_{new}, are evaluated using the bisection method until ω_n and f_n converge for a threshold condition

λ. Finally, the subtracting process is performed to clarify the undetected poles. N_{new} is added to the number of detected excited sates N_{state}. Note that $N_{state} = N_{new}$ in the first iteration. The contributions of the $\alpha(\omega)$ corresponding to the detected poles are obtained by the sum-over-state by a set of excitation energies ω_n and oscillator strengths f_n as:

$$\tilde{\alpha}(\omega) = \sum_{n}^{N_{state}} \frac{f_n}{\omega_n^2 - \omega^2}, \tag{6}$$

where n signifies the number of all detected poles. The difference of the dynamic polarizability $\Delta\alpha(\omega)$, defined as $\Delta\alpha(\omega) = \alpha(\omega) - \tilde{\alpha}(\omega)$, is calculated. The initial decreasing region is searched by using the $\Delta\alpha(\omega)$ values. This serial procedure is repeated until no decreasing regions are detected.

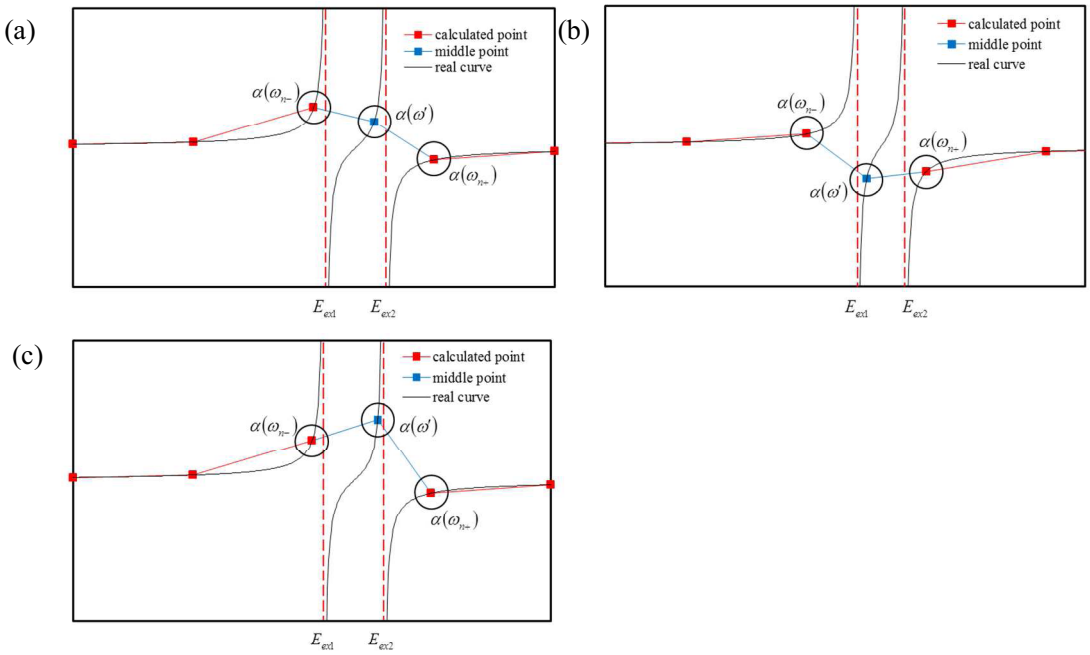

Fig. 6.1. Image of three patterns (a, b, and c) of bisection method when one decreasing point contains two poles.

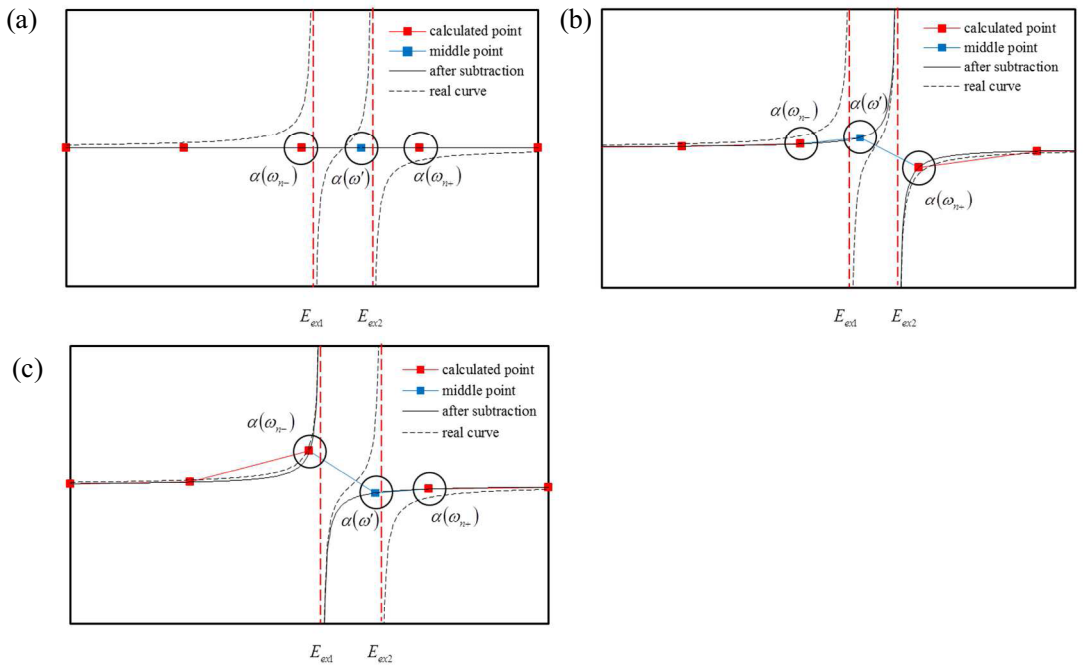

Fig. 6.2. Image of three patterns (a, b, and c) of dynamic polarizability before and after subtracting the contributions from detected excitation E_{ex1}.

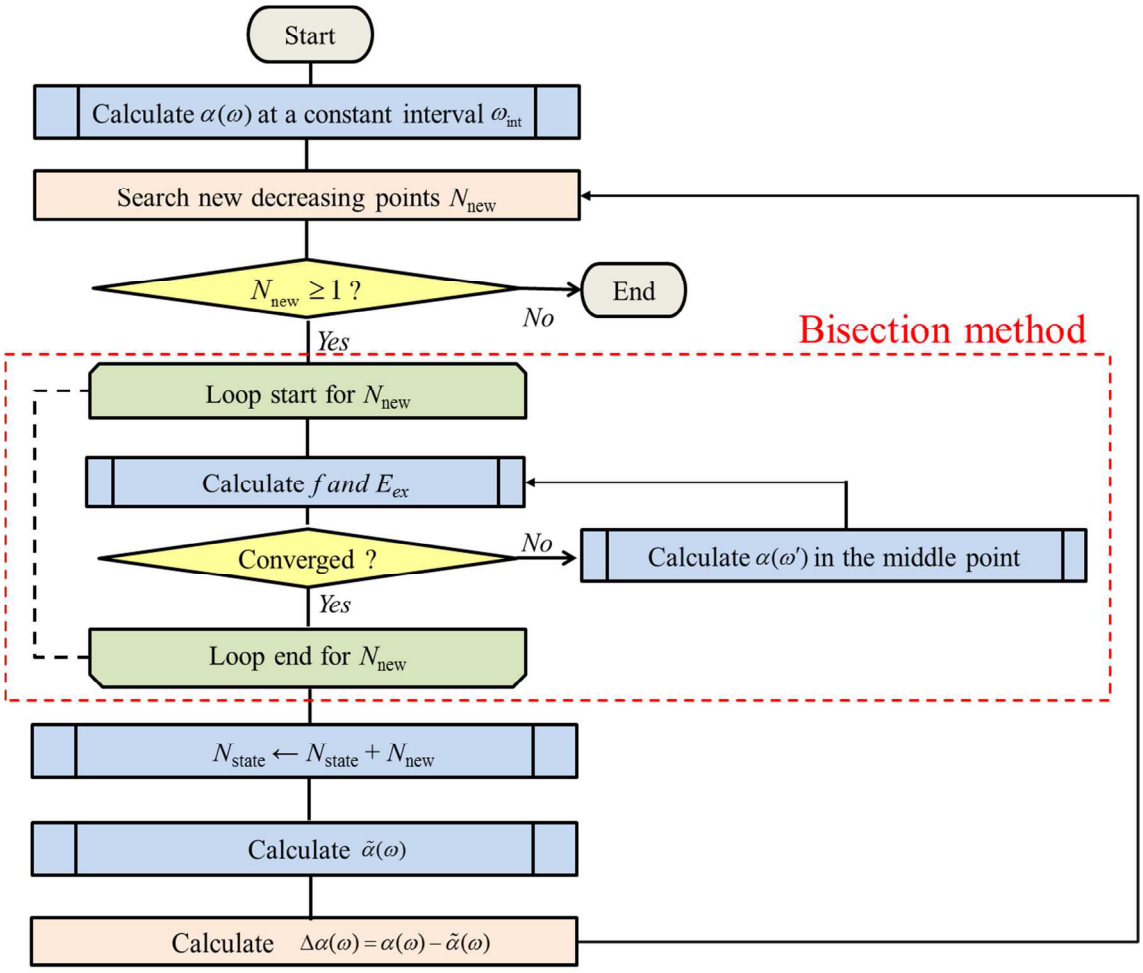

Fig. 6.3. Algorithm to calculate the excited state using dynamic polarizability.

6.3. Numerical assessments

In this section, the performance of the present excited-state calculation using dynamic polarizabilities, based on the simplest treatment such as TDCPHF calculations, is numerically assessed. The results are then compared to those obtained from conventional excited-state calculations such as TDHF calculations. All calculations were performed with the 6-31G** basis set [15,16] by using a modified version of the GAMESS program [17]. The Davidson algorithm [18] was adopted for diagonalization of the Hamiltonian matrix in conventional TDHF calculations, and the maximum number of expansion vector iterations used by the solver was set at 50.

The author first determined the convergence condition λ for the bisection method. Table 6.1 shows the λ-dependence of the errors in excitation energies (ΔE_{ex}) and in oscillator strengths (Δf) within the range 0–10 eV for bromobenzene. Excitation energies and oscillator strengths obtained by the TDHF method are also listed for reference. The listed excitations were detected with ω_{int} = 0.01 eV. No subtracting processes were performed. All allowed excited states except for the forbidden excited states A_2 corresponding to 7.524, 9.352, 9.563, and 9.995 eV were detected. For all the allowed excited states, absolute deviations of excitation energies were less than 0.001 eV for $\lambda \leq 0.1$. Compared with excitation-energy deviations, the deviations of the oscillator strengths slowly converged to zero. The oscillator-strength deviations had a tendency to increase with an increase in oscillator strengths. The absolute deviations of oscillator strengths were less than 0.001 for $\lambda \leq 0.001$. Therefore, all of the following calculations were performed with $\lambda = 0.001$.

Table 6.2 shows the ω_{int}-dependence of excited states within the range 0–10 eV for bromobenzene with ω_{int} = 1.0, 0.5, 0.1, 0.05, and 0.01 eV. No subtracting processes were performed. At ω_{int} = 1.0 and 0.5 eV, only four excited states $2A_1$, $4A_1$, $2B_1$, and $3B_1$ were detected; excited states with small oscillator strengths and quasi-degenerate excited states tend to be passed over, such as $3A_1$, $1B_1$, $4B_1$, $1B_2$, $2B_2$, $3B_2$, $4B_2$, and $5B_2$. The number of detected excited states increases with the decrease of ω_{int}. New four excited states $3A_1$, $4B_1$, $2B_2$, and $4B_2$ were detected at ω_{int} = 0.1 eV. The excited state $2B_1$ was passed over, because the pattern of polarizability for middle-point converted the patterns of Fig. 6.1(b) into those of Fig. 6.1(c). All excited states were detected for ω_{int} = 0.01 eV. The errors in excitation energies and in oscillator strengths (less than 0.001 in either case) were independent of ω_{int}.

Table 6.1. Convergence-condition λ dependence of the absolute errors of excitation energies ΔE_{ex} (in eV) and oscillator strengths Δf within the range 0–10 eV for bromobenzene.

state	TDHF		This work					
			$\lambda = 0.1$		$\lambda = 0.01$		$\lambda = 0.001$	
	E_{ex} [eV]	f	ΔE_{ex} [eV]	Δf	ΔE_{ex} [eV]	Δf	ΔE_{ex} [eV]	Δf
$2A_1$	5.383	0.172	0.000	0.000	0.000	0.000	0.000	0.001
$1B_1$	5.460	0.020	0.000	0.002	0.000	0.002	0.000	0.001
$2B_1$	7.264	0.424	0.000	0.008	0.000	0.003	0.000	0.000
$3A_1$	7.275	0.765	0.000	0.075	0.000	0.003	0.000	0.000
$1A_2$	7.524	0.000	-	-	-	-	-	-
$1B_2$	7.959	0.004	0.000	0.000	0.000	0.000	0.000	0.000
$2B_2$	8.722	0.002	0.000	0.000	0.000	0.000	0.000	0.000
$3B_2$	9.156	0.001	0.000	0.000	0.000	0.000	0.000	0.000
$2A_2$	9.352	0.000	-	-	-	-	-	-
$4A_1$	9.555	0.018	0.000	0.000	0.000	0.000	0.000	0.000
$3A_2$	9.563	0.000	-	-	-	-	-	-
$3B_1$	9.738	0.095	0.000	0.002	0.000	0.002	0.000	0.000
$4B_1$	9.848	0.030	0.000	0.001	0.000	0.001	0.000	0.000
$4B_2$	9.966	0.013	0.000	0.000	0.000	0.000	0.000	0.000
$5B_2$	9.994	0.001	0.000	0.000	0.000	0.000	0.000	0.000
$4A_2$	9.995	0.000	-	-	-	-	-	-

Table 6.2. Constant interval ω_{int} dependence of the errors of excitation energies ΔE_{ex} (in eV) and oscillator strengths Δf obtained within the range 0–10 eV for bromobenzene (ω_{int} = 1.0 eV).

State	TDHF		This work									
			ω_{int} = 1.0 [eV]		ω_{int} = 0.5 [eV]		ω_{int} = 0.1 [eV]		ω_{int} = 0.05 [eV]		ω_{int} = 0.01 [eV]	
	E_{ex} [eV]	f	ΔE_{ex} [eV]	Δf	ΔE_{ex} [eV]	Δf	ΔE_{ex} [eV]	Δf	ΔE_{ex} [eV]	Δf	ΔE_{ex} [eV]	Δf
$2A_1$	5.383	0.172	0.000	0.000	0.000	0.000	0.000	0.000	0.000	0.000	0.000	0.001
$1B_1$	5.460	0.020	-	-	-	-	-	-	0.000	0.000	0.000	0.001
$2B_1$	7.264	0.424	0.000	0.000	0.000	0.000	-	-	-	-	0.000	0.000
$3A_1$	7.275	0.765	-	-	-	-	0.000	0.000	0.000	0.000	0.000	0.000
$1A_2$	7.524	0.000	-	-	-	-	-	-	-	-	-	-
$1B_2$	7.959	0.004	-	-	-	-	-	-	0.000	0.000	0.000	0.000
$2B_2$	8.722	0.002	-	-	-	-	0.000	0.000	0.000	0.000	0.000	0.000
$3B_2$	9.156	0.001	-	-	-	-	-	-	0.000	0.000	0.000	0.000
$2A_2$	9.352	0.000	-	-	-	-	-	-	-	-	-	-
$4A_1$	9.555	0.018	0.000	−0.001	0.000	−0.001	0.000	0.000	0.000	0.000	0.000	0.000
$3A_2$	9.563	0.000	-	-	-	-	-	-	-	-	-	-
$3B_1$	9.738	0.095	0.000	−0.001	0.000	−0.001	0.000	−0.001	0.000	−0.001	0.000	0.000
$4B_1$	9.848	0.030	-	-	-	-	0.000	0.001	0.000	0.001	0.000	0.000
$4B_2$	9.966	0.013	-	-	-	-	0.000	0.000	0.000	0.000	0.000	0.000
$5B_2$	9.994	0.001	-	-	-	-	-	-	-	-	0.000	0.000
$4A_2$	9.995	0.000	-	-	-	-	-	-	-	-	-	-

To demonstrate the efficiency of the subtracting process, the author plotted the data of the polarizability $\alpha(\omega)$ for ω_{int} = 0.1 eV within the range 0–10 eV in Figs. 6.4(a)–(c). The black line and red dashed lines represent the dynamic polarizabilities obtained by TDCPHF and the allowed excitation energies obtained by TDHF, respectively. The author obtained only seven excited states $2A_1$, $3A_1$, $4A_1$, $3B_1$, $4B_1$, $2B_2$, and $4B_2$ without the subtracting process in Fig. 6.4(a). In the first subtracting process, four new excited states $1B_1$, $2B_1$, $5B_1$, and $1B_2$ were obtained, as shown in Fig. 6.4(b). By subtracting the contribution of the other excited states twice, all the allowed excited states were obtained and are shown in Fig. 6.4(c).

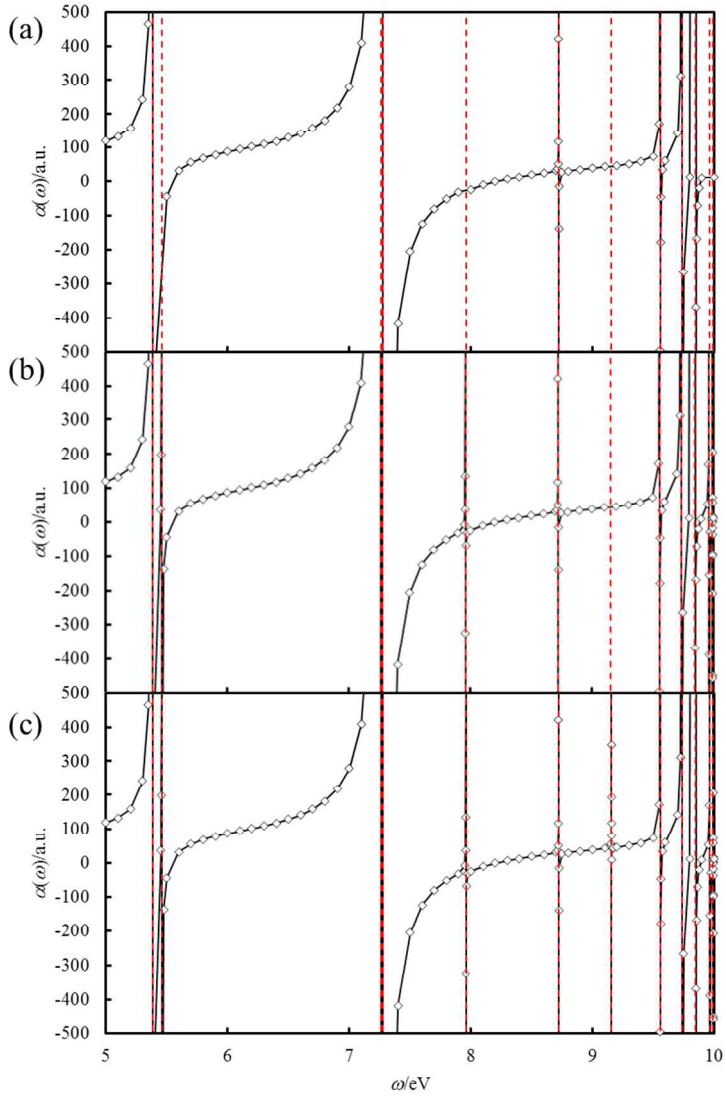

Fig. 6.4. Dynamic polarizability calculated (a) in preprocessing, (b) in the first subtracting, (c) in the second subtracting.

A proper ω_{int} should be determined in order to obtain all the allowed excited states efficiently. Table 6.3 shows the numbers of frequencies N_{freq} and detected excited states N_{state} obtained by the present algorithm within the range 0–10 eV for bromobenzene with ω_{int} = 1.0, 0.5, 0.1, 0.05, and 0.01 eV. The number of all the allowed excited states within the range 0–10 eV was 12. Subtracting processes were performed until no new decreasing regions appeared. The errors of ω_{int} = 1.0, 0.5, 0.1, 0.05, and 0.01 eV are shown in the supporting information. At ω_{int} = 1.0 and 0.5 eV, three excited states $2B_2$, $3B_2$, and $5B_2$ with oscillator strengths less than 0.002 were still passed over after more than one subtraction process, while at ω_{int} = 0.1 and 0.05 eV all the allowed excited states were obtained by using the subtracting process. Although all the allowed excited states were detected without the subtracting process at ω_{int} = 0.01 eV, a large amount of polarizability calculations (565 plots) were needed. The author concludes that a proper value for ω_{int} is 0.1 eV because of the minimum plot. All of the following calculation were performed with ω_{int} = 0.1 eV.

Table 6.3. Numbers of frequencies N_{freq} and detected excited states N_{state} obtained by the present algorithm within the range 0–10 eV for bromobenzene with ω_{int} = 1.0, 0.5, 0.1, 0.05, and 0.01 eV.

	ω_{int} = 1.0		ω_{int} = 0.5		ω_{int} = 0.1		ω_{int} = 0.05		ω_{int} = 0.01	
	N_{freq}	N_{state}	N_{freq}	N_{state}	N_{freq}	N_{state}	N_{freq}	N_{state}	N_{freq}	N_{state}
No subtraction	53	4	55	4	109	7	175	10	565	12
1st subtraction	20	3	20	3	30	4	16	2	-	-
2nd subtraction	19	2	19	2	12	1	-	-	-	-
Total	92	9	94	9	151	12	191	12	565	12

Finally, the author verified the combination of the present algorithm and the DC method on the push-pull polymer, $NH_2-(C_2H_2)_{18}-COOH$. Table 6.4 shows the errors from the TDHF calculations of excitation energies and oscillator strengths obtained by conventional and DC-TDCPHF calculations within the range 0–5 eV. In the DC calculation, a unit consisting of two C atoms in the main chain and the residues bonded to the C atoms was adopted as a central region; six units each to the left and right of these 2 C atoms were treated as the corresponding buffer region. Both conventional and DC-TDCPHF methods detected all the allowed excited state. 2A' was the charge-transfer excitation from HOMO to LUMO, as shown Fig. 6.5. DC as well as conventional methods could reproduce the spread charge-transfer excitation. The excitation-energy and oscillator-strength errors of the DC approximation were less than 0.03 and 0.05, respectively.

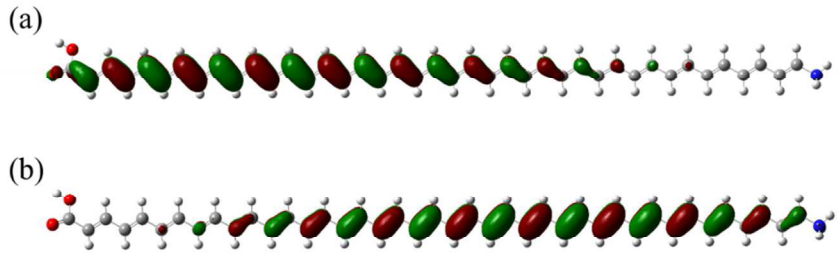

Fig. 6.5. (a) LUMO and (b) HOMO of push-pull polymer, $NH_2-(C_2H_2)_{18}-COOH$ by the HF/6-31G** calculation.

Table 6.4. The errors from the TDHF calculations of excitation energies ΔE_{ex} (in eV) and oscillator strengths Δf obtained by conventional and DC-TDCPHF calculations.

state	TDHF		TDCPHF		DC-TDCPHF	
	E_{ex} [eV]	f	ΔE_{ex} [eV]	Δf	ΔE_{ex} [eV]	Δf
2A’	3.052	9.992	0.000	0.001	0.021	0.047
3A’	3.530	0.001	0.000	0.000	0.013	0.000
4A’	4.056	0.798	0.000	0.001	-0.018	0.012
5A’	4.568	0.001	0.000	0.000	0.014	0.000

6.4. Conclusion

This paper presents the development and the numerical assessments of a pole-search algorithm for dynamic polarizability in order to obtain excited states. The key idea of the algorithm is that at least one pole exists in the region of descending dynamic polarizability with respect to increasing frequency. Once the descending region is detected, the pole is searched by the bisection method. Another key idea is that the influence of the undetected poles in multiple-pole systems is clarified by subtracting the influence of the detected poles. Thus, the algorithm involves iterative operations after the initial search by using a constant frequency interval. The numerical assessments investigated the dependence of excitation energies and oscillator strengths on the convergence condition λ and the constant frequency interval ω_{int}. By using the proper threshold λ and constant interval ω_{int}, the present algorithm effectively detects all the poles. The algorithm combined with DC as well as conventional TDCPHF methods could reproduce the large charge-transfer excitations.

References

1. S. Coriani, S. Høst, B. Jansik, L. Thøgersen, J. Olsen, P. Jørgensen, S. Reine, F. Pawłowski, T. Helgaker, P. Sałek, J. Chem. Phys. 126 (2007) 154108.
2. F. Wu, W. Liu, Y. Zhang, Z. Li, J. Chem. Theory Comput. 7 (2011) 3643.
3. M. Miura, Y. Aoki, J. Comput. Chem. 30 (2009) 2213.
4. Q. Li, Q. Li, Z. Shuai, Synth. Met. 158 (2008) 330.
5. H. Nakatsuji, T. Miyahara, R. Fukuda, J. Chem. Phys. 126 (2007) 084104.
6. H. P. Roy, A. Gupta, P. K. Mukherjee, Int. J. Quant. Chem. 4 (1975) 75.
7. G. P. Das, A. T. Yeates, D. S. Dudis, Int. J. Quant. Chem. 92 (2003) 22.
8. Y. Mochizuki, T. Ishikawa, K. Tanaka, H. Tokiwa, T. Nakano, S. Tanaka, Chem. Phys. Lett. 418 (2006) 418.
9. J. Kussman, C. Ochsenfeld, J. Chem. Phys. 127 (2007) 204103.
10. T. F. Hughes, R. J. Bartlett, J. Chem. Phys. 129 (2008) 054105.
11. T. Touma, M. Kobayashi, H. Nakai, Chem. Phys. Lett. 485 (2010) 247.
12. W. Yang, Phys. Rev. Lett. 66 (1991) 1438.
13. W. Yang, T. S. Lee, J. Chem. Phys. 103 (1995) 5674.
14. T. Touma, M. Kobayashi, H. Nakai, Chem. Physl. Lett. 485 (2010) 247.
15. T. Touma, M. Kobayashi, H. Nakai, Theor. Chem. Acc. 130 (2011) 701.
16. G. A. Petersson, M. A. Al-Laham, J. Chem. Phys. 94 (1991) 6081.
17. G. A. Petersson, A. Bennett, T. G. Tensfeldt, M. A. Al-Laham, W. A. Shirley, J. Mantzaris, J. Chem. Phys. 89 (1988) 2193.
18. M. W. Schmidt, K. K. Baldridge, J. A. Boatz, S. T. Elbert, M. S. Gordon, J. J. Jensen, S. Koseki, N. Matsunaga, K. A. Nguyen, S. Su, T. L. Windus, M. Dupuis, J. A. Montgomery, J. Comput. Chem. 14 (1993) 1347.
19. E. R. Davidson, J. Comput. Phys. 17 (1975) 87.

Part III

Acceleration of Divide-and-Conquer Method by Using Parallel Computations

Chapter 7
Divide-and-Conquer Method with Approximate Fermi Level for Parallel Computations

7.1. Introduction

Parallel computation has become a main stream to deal with large systems by quantum chemical methods. The parallel computations are categorized into shared, distributed, and hybrid memory models. The shared memory models are typified as OpenMP [1], GA [2], and DDI [3]. While each node shares the data within the same node on OpenMP, it shares the data among all nodes through network communications on GA, DDI, and the other global memory array models. The distributed memory model is typified as MPI [4]. Because each CPU core allocates each memory array on MPI, the available memory size per CPU core becomes small. One of the solutions is the hybrid model, in which internode and intranode parallel treatments are performed by MPI and OpenMP, respectively.

The quantum chemical computations with the global memory array and hybrid models can deal with large systems by allocating the large memory size through the network communications. Indeed, several quantum chemical program packages have been developed by global memory array [2,3,5,6] and hybrid models [7–12]. The network communications among multi nodes become the bottlenecks on the parallelization because of the slower internode than intranode communications. The decrease of the network communications is required on the multi-node parallelization. Fragmentation techniques, which divide an entire system into several fragments, could reduce the network communications by separately solving the local equation in each fragment [13–15]. Therefore, the fragmentation techniques have higher affinity with the multi-node parallelization than conventional quantum chemical calculations.

Nakai research group developed the fragmentation techniques based on the DC-SCF method originally proposed by Yang and coworkers [16,17]. The DC-SCF method has a high applicability to delocalized electron and/or spin systems due to the adoption of the common Fermi level for the entire system [18–21]. While the CPU time for determining the common Fermi level is less expensive, it requires a large amount of the network communications among multi nodes due to collecting the information of all fragments. In consequence, the computation of the Fermi level reduces the parallel efficiency compared with the other fragmentation techniques.

This Chapter proposes approximate techniques to estimate the Fermi level

without loss of accuracy to achieve high parallel efficiency. The rest of this chapter is organized as follows. Section 7.2 explains theory and implementation of the proposed techniques. In Section 7.3, numerical assessments are given. Finally, the concluding remarks are described.

7.2. Theory and implementation

7.2.1. DC-SCF with the common Fermi level

This subsection briefly describes the conventional DC-SCF method, which adopts the common Fermi level in every SCF iteration. In the DC-SCF method, the density matrix of the entire system, $\boldsymbol{D}$, is constructed from local density matrices for subsystems $\{s\}$, $\boldsymbol{D}^s$, as follows:

$$D_{\mu\nu} \approx D_{\mu\nu}^{\mathrm{DC}} = \sum_s P_{\mu\nu}^s D_{\mu\nu}^s, \tag{7.1}$$

where s runs all subsystems. In Eq. (7.1), $\boldsymbol{P}^s$ represents the partition matrix with elements of

$$P_{\mu\nu}^s = \begin{cases} 1 & \left[\quad \boldsymbol{S} \qquad \boldsymbol{S} \quad \right] \\ 1/2 & \left[\quad \boldsymbol{B} \qquad \boldsymbol{S} \quad \right] \left[\quad \boldsymbol{S} \qquad \boldsymbol{B} \quad \right] \\ 0 & \text{otherwise.} \end{cases} \tag{7.2}$$

$\boldsymbol{P}^s$ avoids the double counting for the electron numbers of the buffer region. $\boldsymbol{D}^s$ is obtained by the subsystem MO coefficients, $\boldsymbol{C}^s$, subsystem orbital energies, $\boldsymbol{\varepsilon}^s$, and common Fermi level, ε_{F}:

$$D_{\mu\nu}^s = \sum_p f_\beta(\varepsilon - \varepsilon^s) C_\mu^s C_{\mu p}^s . \tag{7.3}$$

where p runs all MOs of the subsystem s, i.e., $\boldsymbol{L}(s)$. $\boldsymbol{C}^s$ and $\boldsymbol{\varepsilon}^s$ are determined by solving the following Roothaan–Hall or Kohn–Sham equation for the subsystem s:

$$\boldsymbol{F}^s \boldsymbol{C}^s = \boldsymbol{\varepsilon}^s \boldsymbol{S}^s \boldsymbol{C}^s . \tag{7.4}$$

Here, $\boldsymbol{S}^s$ and $\boldsymbol{F}^s$ represent the local overlap and Fock matrices for subsystem s, i.e., submatrices of the entire overlap and Fock matrices in the basis of $\boldsymbol{L}(s)$. After solving the local equations, the common Fermi level can be determined via constraint of the total number of electrons, N_{e}:

$$N_{\mathrm{e}} = \mathrm{Tr}[\boldsymbol{D}^{\mathrm{DC}} \boldsymbol{S}]. \tag{7.5}$$

Similarly, the electron numbers of the subsystems $\{s\}$, n_e^s are determined by,

$$n_{\mathrm{e}}^s = \mathrm{Tr}[\boldsymbol{D}^s \boldsymbol{S}^s]. \tag{7.6}$$

Note that N_{e} is not equal to the sum of the electron numbers of subsystems, n_e^s:

$$N_{\mathrm{e}} \neq \sum_{s} n_{\mathrm{e}}^{s} \tag{7.7}$$

The total density matrix $\boldsymbol{D}^{\mathrm{DC}}$ is required in order to construct the Coulomb and exchange parts, i.e., $\boldsymbol{J}^{s}$ and $\boldsymbol{K}^{s}$ of local Fock matrices, $\boldsymbol{F}^{s}$:

$$J_{\mu\nu}^{s} = \sum_{\lambda,\sigma} \sum_{s'} (\mu\nu|\lambda\sigma) P_{\lambda\sigma}^{s'} D_{\lambda\sigma}^{s'}. \tag{7.8}$$

$$K_{\mu\nu}^{s} = \sum_{\lambda,\sigma} \sum_{s'} (\mu\sigma|\lambda\nu) P_{\lambda\sigma}^{s'} D_{\lambda\sigma}^{s'}. \tag{7.9}$$

Note that $\{\mu,\nu\}$ belong to the basis of $\boldsymbol{L}(s)$. Although $\{\lambda,\sigma\}$ in Eqs. (7.8) and (7.9) run all AOs of the entire system, the non-zero parts of $D_{\lambda\sigma}^{\mathrm{DC}}$ are limited in the basis of $\boldsymbol{L}(s')$ for each subsystem due to the property of $\boldsymbol{P}^{s'}$. As a result, the computational costs to construct $\boldsymbol{J}^{s}$ and $\boldsymbol{K}^{s}$ scale as $O(n^2)$ in the DC-SCF method, where n means the number of basis functions of the total system.

FMM, which divides the Coulomb interaction into near- and far-field contributions, reduces the computational costs for the construction of $\boldsymbol{J}^{s}$. In the FMM, the far-field contribution is evaluated by the multipole expansion using atomic charges. On the contrary, the explicit computations of the ERIs are required for the near field. The author here adopts the localization region $\boldsymbol{L}(s)$ as the near field.

$$J_{\mu\nu}^{s} \approx \sum_{\lambda,\sigma\in\boldsymbol{L}(s)} (\mu\nu|\lambda\sigma) \tilde{D}_{\lambda\sigma}^{s} + (\text{far-field term}) \tag{7.10}$$

$\tilde{\boldsymbol{D}}^{s}$ corresponds to the submatrix of the total density matrix $\boldsymbol{D}^{\mathrm{DC}}$ in the basis of $\boldsymbol{L}(s)$. Fig. 7.1 schematically illustrates the procedure of constructing this submatrix $\tilde{\boldsymbol{D}}^{s}$. Although the total density matrix $\boldsymbol{D}^{\mathrm{DC}}$ is constructed from local density matrices of all subsystems, submatrices $\tilde{\boldsymbol{D}}^{s}$ could be constructed from local density matrices of the subsystem s and its adjacent subsystems.

The exchange integral of local Fock matrix is also divided into near- and far-field contributions:

$$K_{\mu\nu}^{s} \approx \sum_{\lambda,\sigma\in\boldsymbol{L}(s)} (\mu\sigma|\lambda\nu) \tilde{D}_{\lambda\sigma}^{s} + (\text{far-field term}) \tag{7.11}$$

The exchange interaction is known to decay exponentially, at least, for insulators. Furthermore, our previous studies [18,19] clarified that the errors for neglecting the far-field exchange interaction can be reduced up to the chemical accuracy when adopting an adequate buffer region. Therefore, the author here neglects the far-field exchange contribution in the calculation of local exchange integral $\boldsymbol{K}^{s}$. In consequence, the combination with the FMM and the approximation of the exchange interaction lead to the

linear-scaling computational cost to evaluate the local Fock matrix $\boldsymbol{F}^s$.

The extension of the DC-SCF method to the unrestricted treatment for open-shell systems is straightforward. Note that for the unrestricted treatment, the common Fermi levels for up- and down-spins are individually determined via constraint of the total numbers of up- and down-spin electrons, respectively [21].

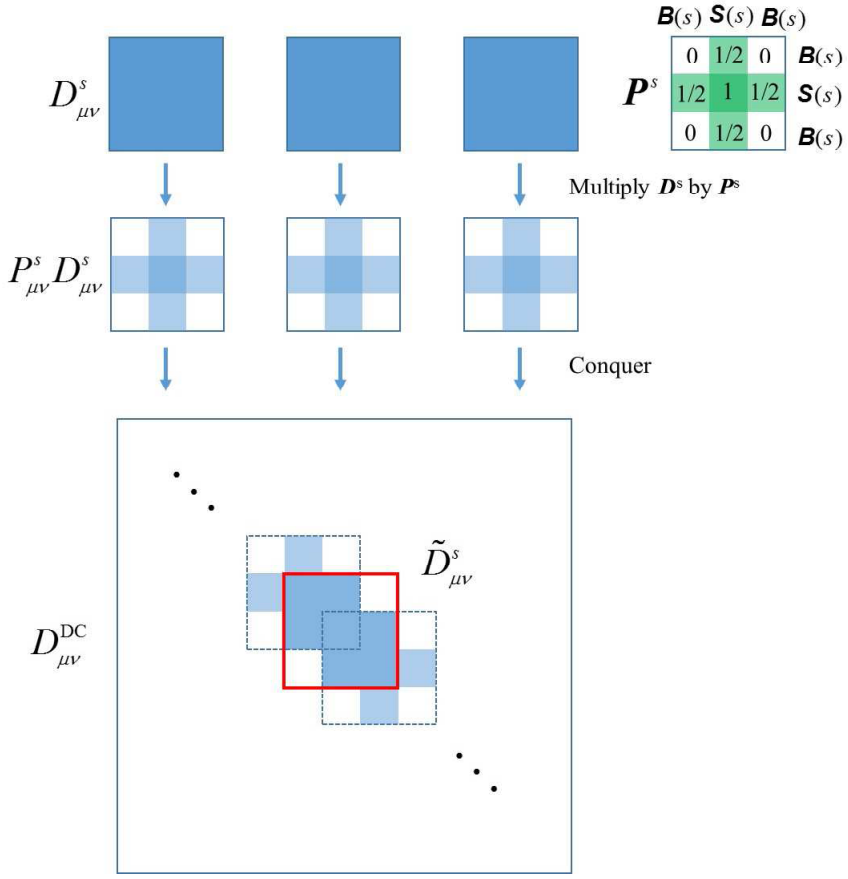

Fig. 7.1. Schematic illustration of construction of $\tilde{\boldsymbol{D}}^s$

7.2.2. Procedure of divide-and-conquer method for parallel computation

The DC-SCF method as well as other fragmentation techniques has higher affinity with the parallel computation than the conventional SCF calculations. Fig. 7.2 shows the schematic illustration of the DC-SCF procedure for parallel computations. In this case, one node is assigned to one subsystem. Note that the node assigned to subsystem #1 becomes a master node. The DC-SCF procedure consists of six steps. Step 1 constructs the local density matrix in Eq. (7.4) on each node. Step 2 constructs submatrix $\tilde{\boldsymbol{D}}^s$ on each node. The communication cost on each node is approximately constant, because each node communicates the local density matrix $\boldsymbol{D}^s$ to several nodes assigned to its adjacent subsystems, not all subsystems. Step 3 independently constructs and diagonalizes the local Fock matrix on each node. In Step 4, all nodes communicate the subsystem MO coefficients $\boldsymbol{C}^s$ and subsystem orbital energies $\boldsymbol{\varepsilon}^s$ to the master node. Step 5 determines the common Fermi level ε_{F} by Eq. (7.6) on the master node. In Step 6, the master node communicates ε_{F} to all nodes. The communication costs of Steps 4 and 6 increase with respect to the number of nodes because of communications among all nodes. The procedure is iterated until the total energy and local density matrices are converged.

Each step has a different parallel efficiency. Steps 1, 2, and 3 are expected to have high parallel efficiencies, because the operations are approximately local on each node as shown in Fig. 7.2. On the contrary, Steps 4, 5, and 6 might show low parallel efficiencies, because the master node must perform all computational tasks. In consequence, the determination of the common Fermi level in Steps 4, 5, and 6 might become one of the bottlenecks on the parallelization.

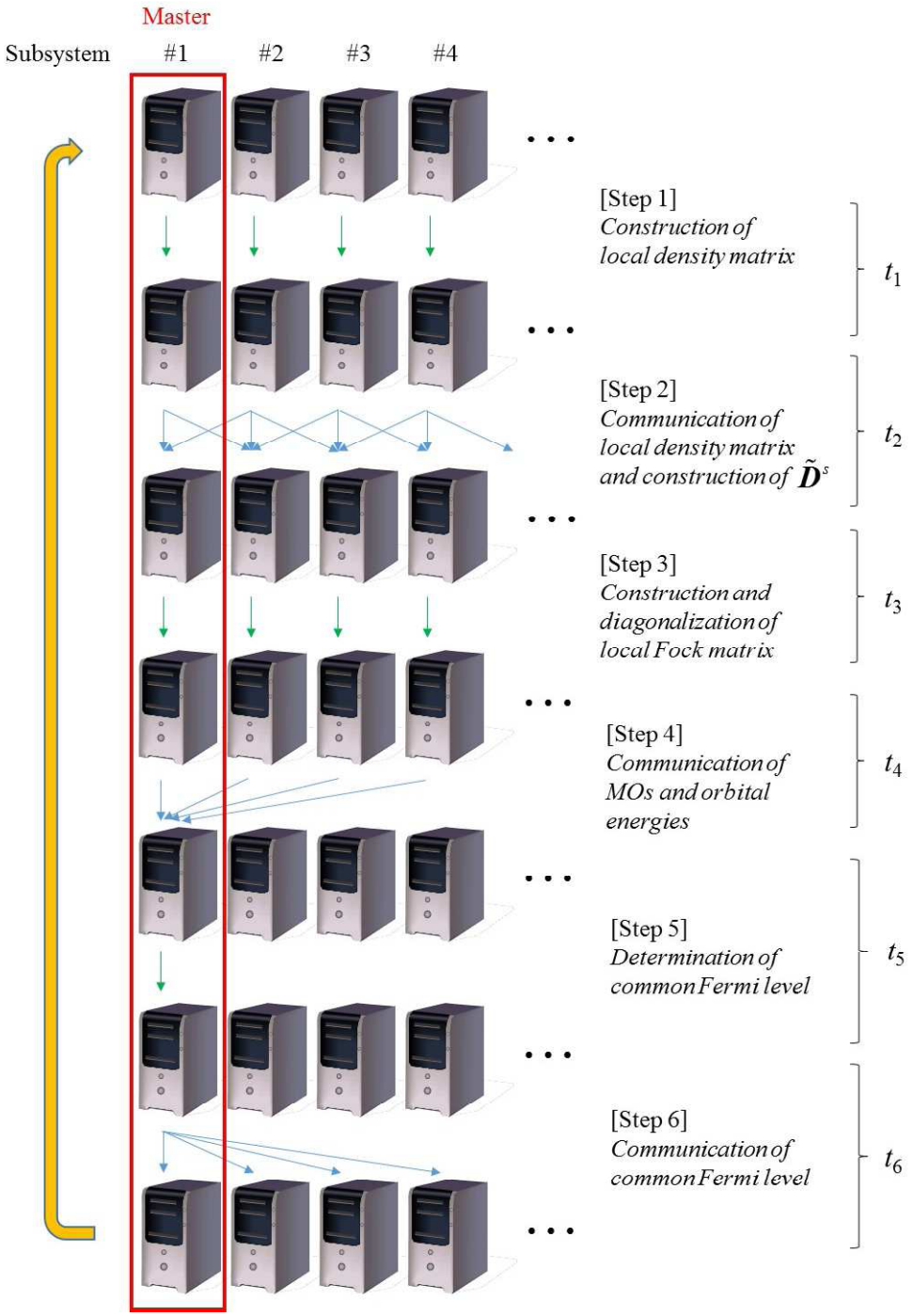

Fig. 7.2. Schematic illustration of the DC-SCF procedure for parallel computations.

7.2.3. Approximate determination of Fermi level

This subsection examines to improve the parallel efficiency of the DC-SCF calculations. As described in the previous subsection, the determination of the common Fermi level requires a large amount of network communications between the master and all the other nodes, which lead to reduction of the parallel efficiency. Thus, the author here proposes two approximations for the determination of Fermi level, which need no communications.

In general, the common Fermi level asymptotically approaches to the converged value during the DC-SCF iterations. Thus, the simplest way to approximate the common Fermi level is to adopt a quasi-converged value. The author calls this procedure as an AFL treatment. The quasi-converged Fermi level is determined by using a threshold, δ_{AFL}, for the Fermi level variation,

$$\left|\Delta\varepsilon_{\mathrm{F}}\right| = \left|\varepsilon_{\mathrm{F}}\left(N_{\mathrm{iter}}\right) - \varepsilon_{F}\left(N_{\mathrm{iter}}-1\right)\right| \le \delta_{\mathrm{AFL}} . \tag{7.12}$$

Once adopting the quasi-converged value, the common Fermi level is fixed. Since the density matrix is determined by using the quasi-converged Fermi level, Eq. (7.5) is not satisfied exactly; namely, the total number of electrons is not kept in the DC-SCF calculations. However, the choice of the adequate threshold, δ_{AFL}, would reduce the error. The electron number of each subsystem is also determined by using the quasi-converged Fermi level.

During the DC-SCF iteration, the electron numbers of individual subsystems approach asymptotically to converged values, respectively. Thus, the second approximation is the adoption of the quasi-converged electron numbers of individual subsystems. The author calls it an AEN treatment. The SCF iteration to firstly achieve the quasi-convergence is determined by using the threshold, δ_{AEN}, for the maximum variation of the subsystem electron numbers,

$$\max\left|\Delta n_{\mathrm{e}}^{s}\right| = \max\left|n_{\mathrm{e}}^{s}\left(N_{\mathrm{iter}}\right) - n_{\mathrm{e}}^{s}\left(N_{\mathrm{iter}}-1\right)\right| \le \delta_{\mathrm{AEN}} . \tag{7.13}$$

Once satisfying the condition in Eq. (7.13), the subsystem electron numbers are fixed to the quasi-converged values, respectively. To keep this condition, the Fermi level is relaxed and determined individually for each subsystem by Eq. (7.6). Namely, the Fermi level of each subsystem is no longer common value. Furthermore, Eq. (7.5) is not satisfied exactly, although the electron number of each subsystem is kept. The choice of the adequate threshold, δ_{AEN}, would reduce the error.

7.2.4. Implementations of AFL and AEN methods

The author implemented the AFL and AEN treatments for parallel computations. Fig. 7.3 presents the pseudocode for the AFL and AEN treatments, which consist of six steps similar to the conventional DC-SCF method. The wall-clock times for the individual steps are defined as t_1, t_2, t_3, t_4, t_5, and t_6. The convergence of the common Fermi level ε_{F} or the subsystem electron numbers n_e^s is checked after Step 6 in the AFL and AEN methods, respectively. After the convergence, the AFL and AEN methods skip Steps 4, 5, and 6. The AEN method determines individual Fermi levels $\varepsilon_{\mathrm{F}}^s$ via the constraint by Eq. (7.6), of which the wall-clock time is included in t_5. The procedure is iterated until the energy and local density matrices are converged.

The author developed a two-level hierarchical parallelization scheme for DC-SCF calculations as well as DC-MP2 calculations [22]. The combination of coarse-grain and fine-grain parallel treatments is realized using the GDDI [23]. The coarse-grain and fine-grain parallel treatments are accomplished by assigning one subsystem to one node and distributing the computational task of each subsystem in the same node, respectively. Parallel implementations by GDDI are straightforward using the MPI communicator. When the number of subsystems is larger than that of nodes, the subsystems are cyclically assigned to each node in descending order of the computational cost estimated by the number of basis functions of $\boldsymbol{L}(s)$, m, namely dynamic load balancing. The estimated cost of each subsystem is obtained by construction costs of the local Fock matrix as the largest computational cost of each subsystem, that is, $O(m^4)$.

Loop N_{iter}
  Loop subsystem s
    Construction of $\boldsymbol{D}^s$
  End Loop subsystem s
  } Step 1: t_1

  Loop subsystem s
    Communication of $\boldsymbol{D}^s$
    Construction of $\tilde{\boldsymbol{D}}^s$
  End Loop subsystem s
  } Step 2: t_2

  Loop subsystem s
    Construction and diagonalization of $\boldsymbol{F}^s$
  End Loop subsystem s
  } Step 3: t_3

  If ($\delta_{\text{AFL}} \le |\Delta\varepsilon_{\text{F}}|$ or $\delta_{\text{AEN}} \le \max\left(\left|\Delta n_e^s\right|\right)$) then
    Communication of $\boldsymbol{C}^s$ and $\boldsymbol{\varepsilon}^s$
  } Step 4: t_4
    Determination of ε_{F}
  } Step 5: t_5
  End if

  Communication of ε_{F}
  } Step 6: t_6

  Check convergence for E and $\boldsymbol{D}^s$
  Check convergence for ε_{F} or n_e^s

  If (AEN method and $\delta_{\text{AEN}} \le \max\left(\left|\Delta n_e^s\right|\right)$)
    Loop subsystem s
      Determination of ε_{F}^s
    End Loop subsystem s
  End if
End Loop N_{iter}

Fig. 7.3. Pseudocode of the AFL and AEN algorithms.

7.3. Numerical assessment

This section assesses the performances of the proposed AFL and AEN methods by comparing to the standard DC-SCF method. The 6-31G** basis sets [24] were adopted. The DC-SCF calculations were performed at the HF level. All calculations were performed by using the modified version of the GAMESS program package [25] and employing 16 nodes of an octa-core processor personal computer cluster connected with gigabit Ethernet, where each node has 2.9 GHz processor (Intel Xeon E5-2690).

First of all, the convergences of the common Fermi level ε_F and electron numbers of individual subsystem n_e^s were verified in the standard DC-SCF calculation. The adopted system was a push-pull conjugated polymer, $(CN)_2C{=}C{-}(CH{=}CH)_{18}{-}C_6H_5NH_2$, as depicted in Fig. 7.4. This molecule has a delocalized electronic structure. Furthermore, the electronic structures of the subsystems are expected to be heterogeneous, because the electron-accepting and -donating groups exist at the left- and right-hand sides, respectively. In general, the delocalized and heterogeneous electronic structures are difficult to treat by the fragmentation technique. In the DC-SCF calculations, a unit consisting of two C atoms in the main chain and residues bonding to the C atoms was adopted as a central region; the left-and-right seven units were treated as the corresponding buffer region. Subsystems were numbered from the left edge as shown in Fig. 7.4.

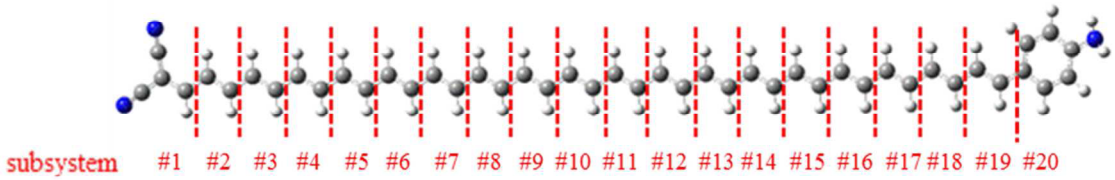

Fig. 7.4. Structure of push-pull polyene, $(CN)_2C{=}C{-}(CH{=}CH)_{18}{-}C_6H_5NH_2$.

Figs. 7.5 (a) and (b) show the absolute variations of the common Fermi level $|\Delta\varepsilon_F|$ and electron numbers $|\Delta n_e^s|$ for subsystems #1, #10, and #20. The absolute variations of the total energy $|\Delta E| = |E(N_{\text{iter}}) - E(N_{\text{iter}} - 1)|$ are plotted in Figs. 7.5 (a) and (b). The total energy and density matrix were converged at $N_{\text{iter}} = 22$. The convergence processes of $|\Delta\varepsilon_F|$ and $|\Delta n_e^s|$ are comparable to that of $|\Delta E|$. The convergence processes of $|\Delta n_e^s|$ depended on the site of the polymer. $|\Delta n_e^{s(\#20)}|$ was rapidly converged because of smaller charge for subsystem #20 than subsystems #1 and #10; the charges for subsystems #1, #10, and #20 are +0.0259, +0.0070, and 0.0000, respectively. $|\Delta n_e^s|$ for the other subsystems were smaller than $|\Delta n_e^s|$ for subsystem #1. While $|\Delta\varepsilon_F|$ that became less than 10^{-2}, 10^{-3}, and 10^{-4} hartree were at $N_{\text{iter}} = 5$, 9, and 14, $|\Delta n_e^s|$ that became less than 10^{-2}, 10^{-3}, and 10^{-4} hartree were at $N_{\text{iter}} = 9$, 11, and 16, respectively.

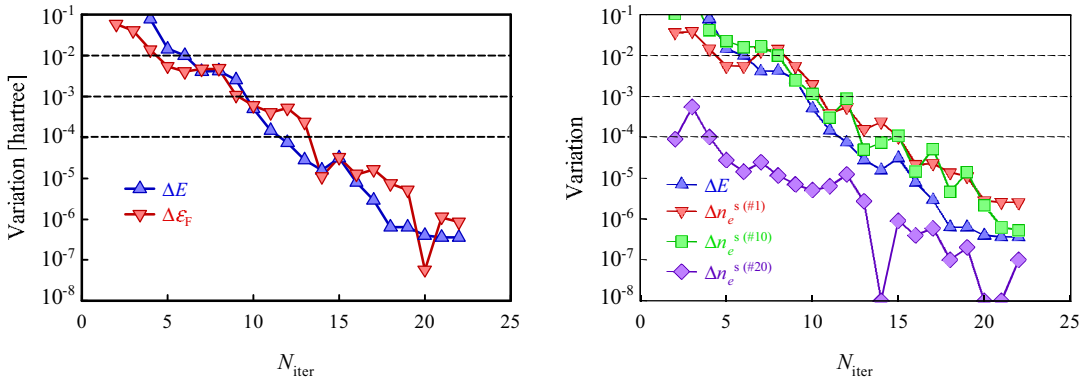

Fig. 7.5. Absolute variations (in atomic unit) of the total energy $|\Delta E|$ (in hartree), (a) common Fermi level $|\Delta\varepsilon_F|$ (in hartree) and (b) electron numbers $|\Delta n_e^s|$ for subsystems #1, #10, and #20 from the converged values in the DC calculation.

Next, the author examined the performance of the AFL method using the push-pull conjugated polymer, $(CN)_2C{=}C{-}(CH{=}CH)_{18}{-}C_6H_5NH_2$. Fig. 7.6 shows the changes of the common Fermi level ε_F with respect to the SCF iteration in the standard DC-SCF calculation and the AFL treatments with $\delta_{\text{AFL}} = 10^{-2}$, 10^{-3}, and 10^{-4} hartree. In the standard DC-SCF calculation, the common Fermi level changes at every SCF iteration. On the contrary, the common Fermi levels were fixed after $N_{\text{iter}} = 5$, 9, and 14 in the AFL calculations with $\delta_{\text{AFL}} = 10^{-2}$, 10^{-3}, and 10^{-4} hartree, respectively. In this scale, the result for $\delta_{\text{AFL}} = 10^{-4}$ hartree overlap with that of the standard calculation. Note that in the three AFL calculations, the SCF iterations to converge the total energy and density matrix were the same as the standard DC-SCF calculation: i.e., $N_{\text{iter}} = 22$.

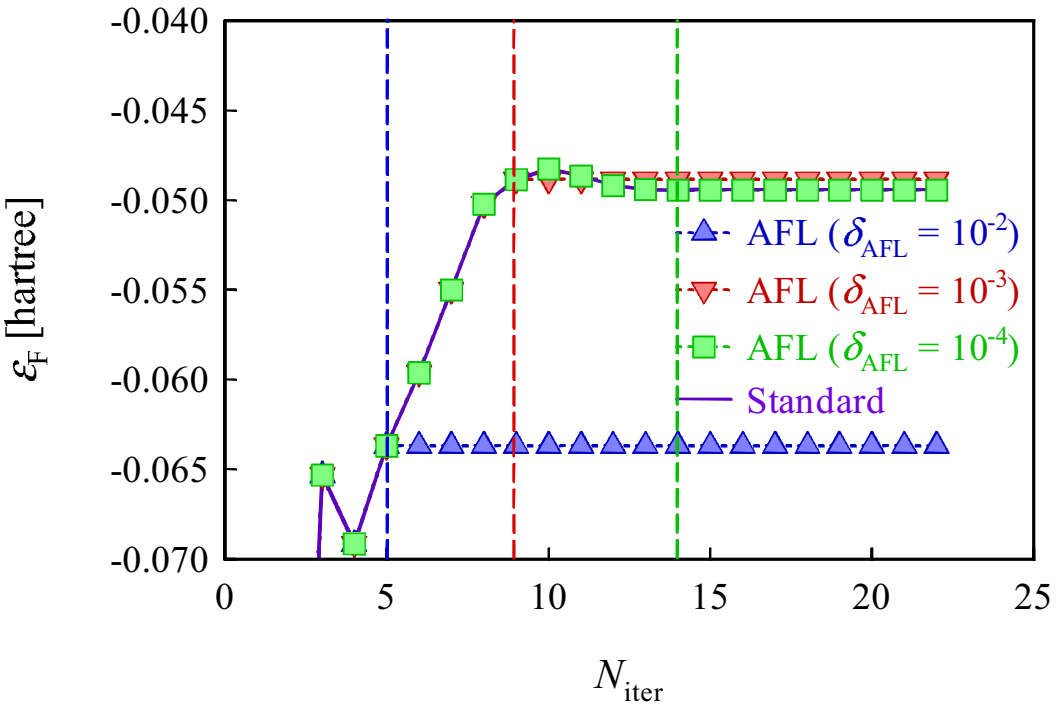

Fig. 7.6. Common Fermi level ε_F (in hartree) with respect to the SCF iteration in the standard DC-SCF calculation and the AFL treatments with δ_{AFL} = 10^{-2}, 10^{-3}, and 10^{-4} hartree.

Fig. 7.7 shows the changes of the electron numbers n_e^s for subsystems #1, #10, and #20 in the standard DC-SCF calculation and the AFL method with δ_{AFL} = 10^{-2}, 10^{-3}, and 10^{-4}. As expected, the errors of the quasi-converged electron numbers of the subsystems increase as larger δ_{AFL}; For example, namely, at subsystem #1, the errors are -0.0243, +0.0061, and +0.0001 for δ_{AFL} = 10^{-2}, 10^{-3}, and 10^{-4} hartree, respectively. Furthermore, the errors become smaller in the order of the subsystems #1, #10, and #20, which is the same order of the subsystem charges as mentioned above. A careful observation clarifies that the underestimated ε_F with δ_{AFL} = 10^{-2} hartree led to the underestimation of the subsystem electron number, while the slightly overestimated ε_F with δ_{AFL} = 10^{-3} hartree led to the slight overestimation. The adoption of ε_F using δ_{AFL} = 10^{-4} hartree ensured high accuracy of the subsystem electron numbers.

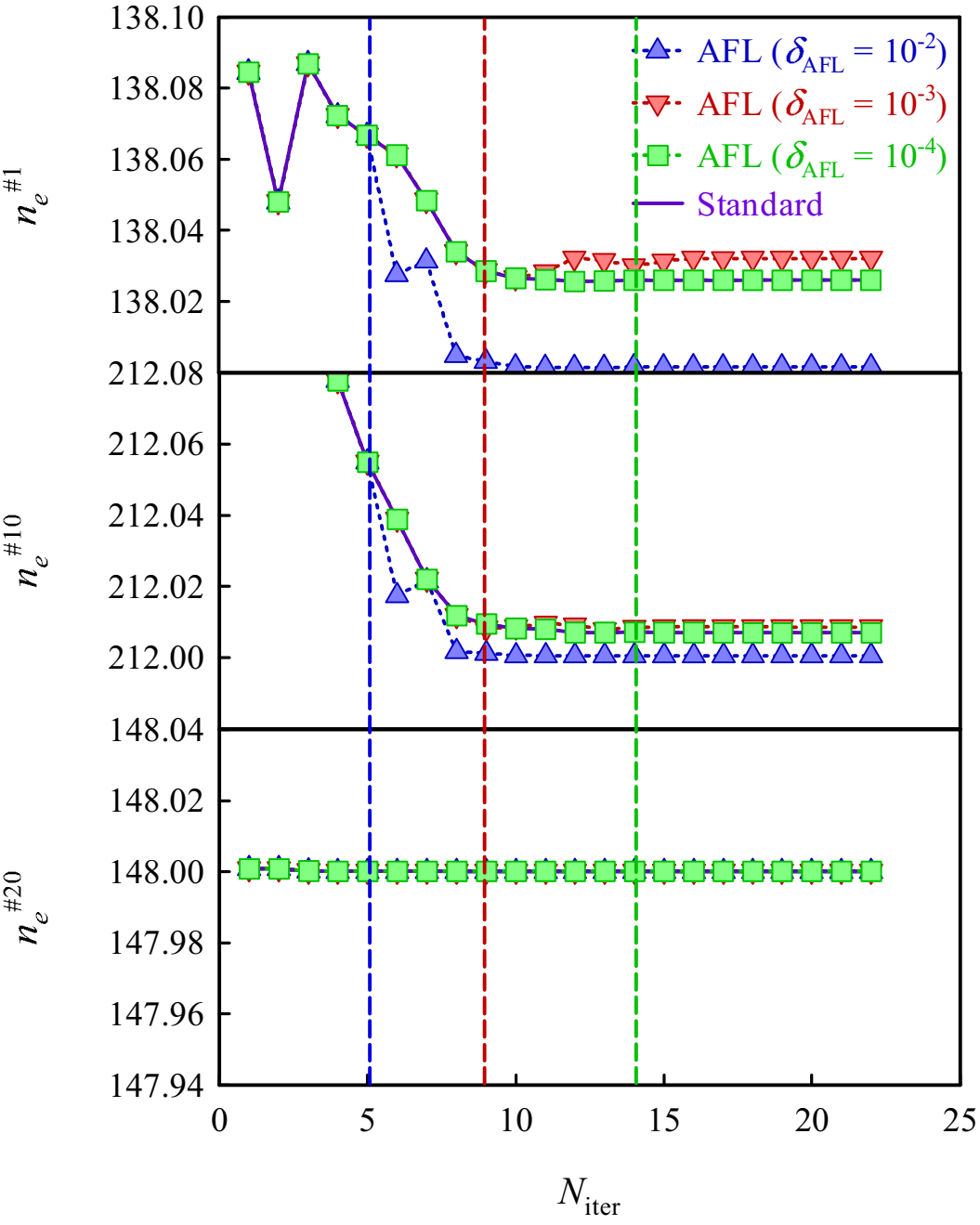

Fig. 7.7. Electron numbers n_e^s for subsystems #1, #10, and #20 in the standard DC-SCF calculation and the AFL method with δ_{AFL} = 10^{-2}, 10^{-3}, and 10^{-4} hartree.

The author further investigated the performance of the AEN method adopting $(CN)_2C{=}C{-}(CH{=}CH)_{18}{-}C_6H_5NH_2$. Fig. 7.8 shows the changes of the electron numbers n_e^s for subsystems #1, #10, and #20 in the standard DC-SCF calculation and the AEN treatments with $\delta_{AEN} = 10^{-2}$, 10^{-3}, and 10^{-4}. In the standard DC-SCF calculation, the subsystem electron numbers changed at every SCF iteration due to the variation of the common Fermi level. On the contrary, the subsystem electron numbers were fixed after $N_{iter} = 9$, 11, and 16 in the three AEN calculations, respectively. The SCF iterations to converge the total energy and density matrix were different: i.e., $N_{iter} = 27$, 23, and 22 for $\delta_{AEN} = 10^{-2}$, 10^{-3}, and 10^{-4}, respectively. In consequence, the results for $\delta_{AEN} = 10^{-4}$ overlapped with those of the standard calculation.

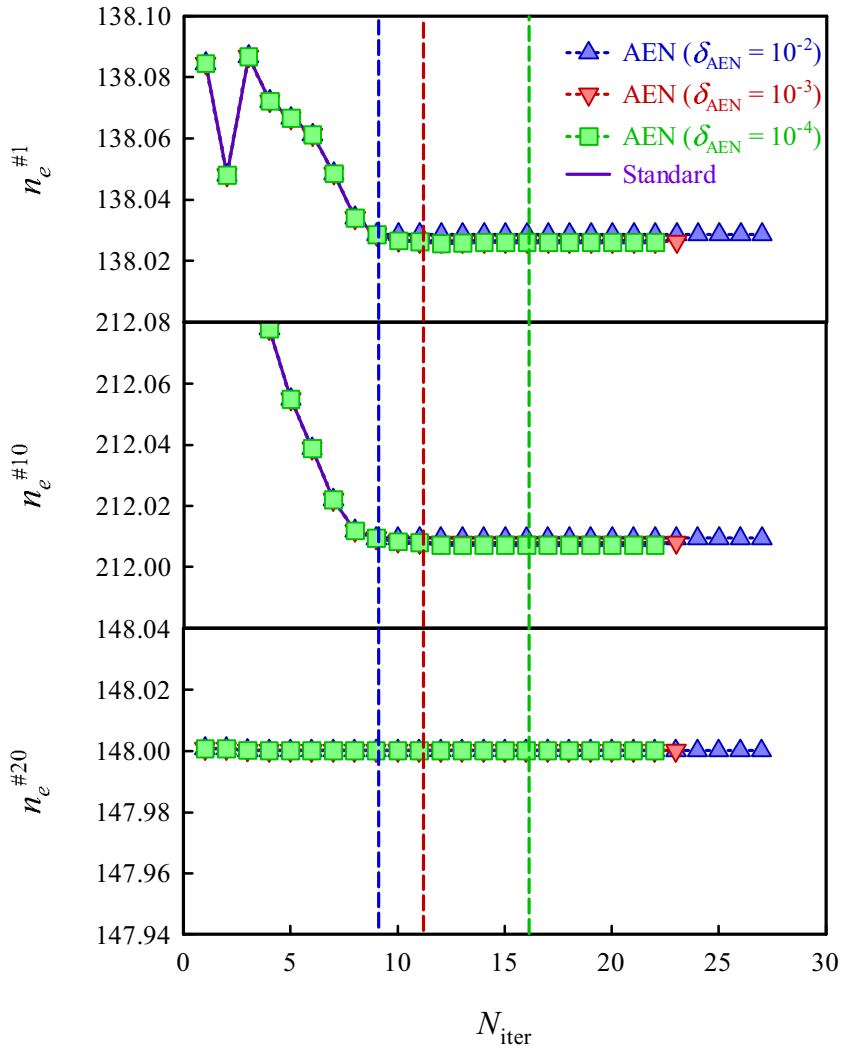

Fig. 7.8. Electron numbers n_e^s for subsystems #1, #10, and #20 in the standard DC-SCF calculation and the AEN treatments with $\delta_{AEN} = 10^{-2}$, 10^{-3}, and 10^{-4}.

Fig. 7.9 shows the changes of the common Fermi level ε_F with respect to the SCF iteration in the standard DC-SCF calculation and the AEN treatments with δ_{AEN} = 10^{-2}, 10^{-3}, and 10^{-4}. In the standard DC-SCF method as well as the AFL treatment, the Fermi level was common to all the subsystem. On the other hand, the AEN treatment determined the individual Fermi level for each subsystem to conserve the subsystem electron number. Therefore, Figs. 7.9(a), (b), and (c) demonstrated different behaviors of the Fermi levels for the subsystems #1, #10, and #20, respectively. The crude threshold $\delta_{AEN} = 10^{-2}$ led to large gaps among the converged Fermi levels for #1, #10, and #20. The gaps became smaller for $\delta_{AEN} = 10^{-3}$. For $\delta_{AEN} = 10^{-4}$, three Fermi levels agree well with the result of the standard DC-SCF calculation.

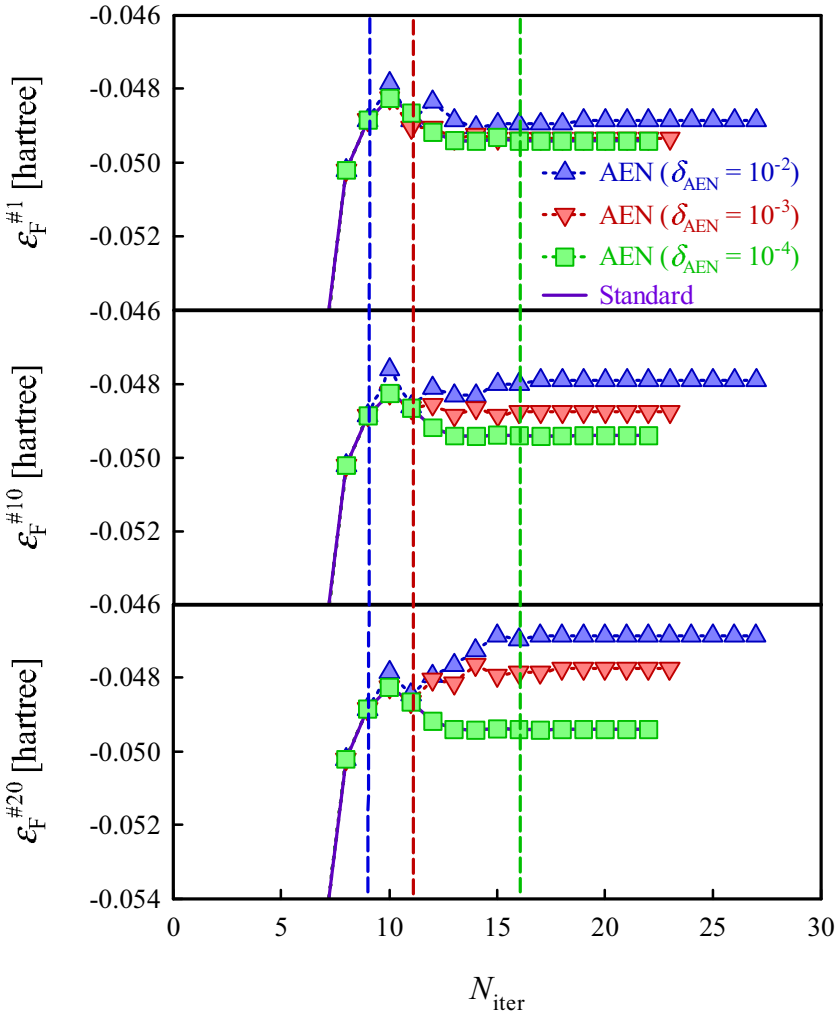

Fig. 7.9. Common Fermi level ε_F (in hartree) with respect to the SCF iteration in the standard DC-SCF calculation and the AEN treatments with δ_{AEN} = 10^{-2}, 10^{-3}, and 10^{-4}.

Table 7.1 summarizes the deviations of the total energy, Fermi level, and electron numbers of the subsystem #1, #10, and #20 obtained by the AFL and AEN calculations with respect to the standard DC-SCF results. As observed in Figs. 7.6-7.9, the deviations decreased as the smaller threshold, δ_{AFL} and δ_{AEN}. It should be noted that even for the crude threshold of $\delta_{\mathrm{AFL/AEN}} = 10^{-2}$ (hartree/-), the deviations of total energies were less than 1 mhartree.

The applicability of the AFL and AEN treatments was verified for a series of benchmarks: namely, hydrogen fluoride clusters $(\mathrm{HF})_n$ (n = 20, 30, and 40), water clusters $(\mathrm{H_2O})_n$ (n = 100, 125, and 150), polyglycine $(\mathrm{gly})_n$ (n = 10, 20, and 30), and polyene chain system $\mathrm{C}_n\mathrm{H}_{n+2}$ (n = 40, 60, and 80). In the DC-SCF calculations, each monomer was adopted as the central region. The buffer regions were defined as the atoms in the union of spheres centered at the atoms of central regions within radius of 5.0, 5.0, 8.0 and 9.0 (Å) for $(\mathrm{HF})_n$, $(\mathrm{H_2O})_n$, $(\mathrm{gly})_n$, and $\mathrm{C}_n\mathrm{H}_{n+2}$, respectively.

Table 7.2 summarizes the deviations of the total energies (in mhartree) obtained by the AFL and AEN calculations with respect to the standard DC-SCF results. The thresholds were changed: $\delta_{\mathrm{AFL/AEN}} = 10^{-2}$, 10^{-3}, and 10^{-4}. The energy errors for the molecular cluster systems, i.e. $(\mathrm{HF})_n$ and $(\mathrm{H_2O})_n$, were less than 1 μhartree even for $\delta_{\mathrm{AFL/AEN}} = 10^{-2}$ (hartree/-) because of the nature of the local electronic structure. On the other hand, the energy errors for the covalent bond systems, i.e. $(\mathrm{gly})_n$ and $\mathrm{C}_n\mathrm{H}_{n+2}$, became larger, but were still less than 1 mhartree.

Table 7.2 lists the SCF iteration to begin the AFL/AEN treatment as well as that to achieve the convergence; They are represented by N_{bgn} and N_{cnv}, respectively. N_{cnv} of the AFL and AEN calculations were the same as those of the standard DC-SCF calculations, except for $(\mathrm{gly})_{30}$ by the AEN method. N_{bgn} was more sensitive to the threshold in the AFL treatment than that in the AEN one. In fact, N_{bgn} in the AFL treatment increased as the smaller threshold.

Finally, the parallel efficiencies of the AFL and AEN methods were examined. Table 7.3 shows wall-clock times of individual steps in the standard DC-SCF, AFL, and AEN calculations of $(\mathrm{HF})_{128}$. Step 1 corresponds to the construction of local density matrices, Step 2 to the communication of local density matrices and construction of $\tilde{\boldsymbol{D}}^s$, Step 3 to the construction and diagonalization of local Fock matrices, Step 4 to the communication of MOs and orbital energies, Step 5 to the determination of the common Fermi level, and Step 6 to the communication for the common Fermi level. The time to determinate individual Fermi levels in the AEN method was included in t_5. The calculations were performed by $\delta_{\mathrm{AFL/AEN}} = 10^{-3}$ (hartree/-).

Table 7.3 also lists the parallel scalability (S) of total wall time (t_{tot}) with respect to the eight-core case (N_{core} = 8), which is defined as,

$$S = \frac{8 * t_{\mathrm{tot}}(8)}{N_{\mathrm{core}} * t_{\mathrm{tot}}(N_{\mathrm{core}})}. \tag{7.14}$$

where N_{core} is the number of processor cores. All calculations were converged at 11 SCF iteration: $N_{\mathrm{cnv}} = 11$. The SCF iteration to begin the AFL/AEN treatments were two: $N_{\mathrm{bgn}} = 2$.

In all cases, the wall clock times of Step 3 were the longest among all steps. However, t_3, as well as t_1 and t_2, approximately decreased in inverse proportion to N_{core}. This means that Steps 1, 2, and 3 had high parallel efficiencies. It is reasonable since Steps 1 and 3 performed independent operations to treat local Fock and density matrices. Although Step 2 communicated local density matrices among several cores that treated adjacent subsystems, the communications were not global.

Although t_4, t_5, and t_6 were small, the times were almost constant even when N_{core} increased. Because Steps 4 and 6 performed communications with all nodes and Step 5 used the master node. These processes would become one of the bottlenecks of the DC-SCF method on the parallel computations. Indeed, the parallel scalability S became smaller as N_{core} increased. On the other hand, the AFL and AEN methods could skip the processes partially and, therefore, reduce their wall clock times. In consequence, the decrease of the parallel scalability S were considerably smaller than the standard case.

Table 7.1. Deviations of the total energy E (in hartree), Fermi level ε_F (in hartree), and electron numbers n_e^s of the subsystem #1, #10, and #20 obtained by the AFL and AEN calculations with respect to the standard DC-SCF results

	Standard	AFL			AEN		
		$\delta_{AFL} = 10^{-2}$	$\delta_{AFL} = 10^{-3}$	$\delta_{AFL} = 10^{-4}$	$\delta_{AEN} = 10^{-2}$	$\delta_{AEN} = 10^{-3}$	$\delta_{AEN} = 10^{-4}$
E [hartree]	-1930.013950	0.000429	-0.000108	0.000000	-0.000064	-0.00001	0.000000
ε_F [hartree]	-0.0494	-0.0143	0.0005	0.0000	-	-	-
$\varepsilon_F^{s(\#1)}$ [hartree]	-	-	-	-	0.0005	0.0001	0.0000
$\varepsilon_F^{s(\#10)}$ [hartree]	-	-	-	-	0.0015	0.0007	0.0000
$\varepsilon_F^{s(\#20)}$ [hartree]	-	-	-	-	0.0025	0.0017	0.0000
$n_e^{s(\#1)}$	138.0259	-0.0243	0.0061	0.0001	0.0026	0.0002	0.0001
$n_e^{s(\#10)}$	212.0070	-0.0065	0.0016	0.0000	0.0015	0.0001	0.0001
$n_e^{s(\#20)}$	148.0000	0.0000	0.0000	0.0000	0.0000	0.0000	0.0000

Table 7.2. Deviations of the total energies (in mhartree) obtained by the AFL and AEN calculations with respect to the standard DC-SCF results.

	Standard	AFL									AEN								
		$\delta_{AFL} = 10^{-2}$			$\delta_{AFL} = 10^{-3}$			$\delta_{AFL} = 10^{-4}$			$\delta_{AEN} = 10^{-2}$			$\delta_{AEN} = 10^{-3}$			$\delta_{AEN} = 10^{-4}$		
	N_{cnv}	E	N_{bgn}	N_{cnv}	E	N_{bgn}	N_{cnv}	E	N_{bgn}	N_{cnv}	E	N_{bgn}	N_{cnv}	E	N_{bgn}	N_{cnv}	E	N_{bgn}	N_{cnv}
		diff.			difff.			diff.			diff.			diff.			dev		
$(HF)_{20}$	11	0.000	2	11	0.000	3	11	0.000	6	11	0.000	2	11	0.000	2	11	0.000	2	11
$(HF)_{30}$	10	0.000	2	10	0.000	3	10	0.000	6	10	0.000	2	10	0.000	2	10	0.000	2	10
$(HF)_{40}$	10	0.000	2	10	0.000	2	10	0.000	6	10	0.000	2	10	0.000	2	10	0.000	2	10
$(H_2O)_{100}$	12	0.000	2	12	0.000	3	12	0.000	5	12	0.000	2	12	0.000	2	12	0.000	2	12
$(H_2O)_{125}$	13	0.000	2	13	0.000	3	13	0.000	5	13	0.000	2	13	0.000	2	13	0.000	2	13
$(H_2O)_{150}$	12	0.000	2	12	0.000	3	12	0.000	5	12	0.000	2	12	0.000	2	12	0.000	2	12
$(gly)_{10}$	15	0.000	5	15	0.000	9	15	0.000	11	15	-0.005	2	15	-0.005	2	15	-0.005	2	15
$(gly)_{20}$	16	-0.002	4	16	0.000	8	16	0.000	10	16	0.009	2	16	0.009	2	16	0.009	3	16
$(gly)_{30}$	16	-0.005	5	16	0.003	8	16	0.000	10	16	0.014	2	17	0.014	3	17	0.014	3	17
$C_{40}H_{42}$	12	-0.063	3	12	-0.014	5	12	0.000	8	12	0.065	3	12	0.026	4	12	0.004	7	12
$C_{60}H_{62}$	12	-0.107	3	12	-0.024	5	12	0.000	8	12	0.046	4	12	0.046	4	12	0.000	7	12
$C_{80}H_{82}$	12	-0.148	3	12	-0.032	5	12	0.000	8	12	0.146	3	12	0.064	4	12	0.000	7	12

Table 7.3. Wall-clock times (in s) of the construction of local density matrices t_1, communication of local density matrices and construction of $\tilde{\boldsymbol{D}}^s$ t_2, construction and diagonalization of local Fock matrices t_3, communication of MOs and orbital energies t_4, determination of the common Fermi level t_5, and communication for the common Fermi level t_6, in standard DC-SCF, AFL, and AEN calculations of $(HF)_{128}$.

	Standard							AFL							AEL						
N_{core}	t_1 [s]	t_2 [s]	t_3 [s]	t_4 [s]	t_5 [s]	t_6 [s]	S	t_1 [s]	t_2 [s]	t_3 [s]	t_4 [s]	t_5 [s]	t_6 [s]	S	t_1 [s]	t_2 [s]	t_3 [s]	t_4 [s]	t_5 [s]	t_6 [s]	S
8	0.48	0.16	27.11	0.94	0.03	0.00	-	0.48	0.16	27.23	0.12	0.01	0.00		0.47	0.16	27.25	0.13	0.01	0.00	-
16	0.24	0.08	13.76	1.22	0.03	0.00	93.6	0.24	0.08	13.68	0.13	0.01	0.00	99.0	0.25	0.08	13.63	0.14	0.01	0.00	99.3
32	0.13	0.04	6.87	1.25	0.03	0.00	86.3	0.13	0.04	6.91	0.15	0.01	0.00	96.7	0.12	0.04	6.90	0.15	0.01	0.00	97.0
64	0.06	0.02	3.51	1.28	0.03	0.00	73.2	0.06	0.02	3.47	0.15	0.01	0.00	94.3	0.06	0.02	3.51	0.15	0.01	0.00	93.4
128	0.04	0.01	1.82	1.33	0.03	0.00	55.6	0.04	0.01	1.83	0.15	0.01	0.00	85.8	0.03	0.01	1.81	0.17	0.01	0.00	86.3

7.4. Conclusion

This Chapter proposed two efficient algorithms of the linear-scaling DC-SCF method for parallel computations. The algorithms could reduce the network communications in determining the common Fermi level. The AFL and AEN methods adopted approximate techniques to estimate the Fermi level in the latter part of SCF procedure. The numerical assessments of the methods clarified that the AFL and AEN methods were confirmed to display a higher parallel efficiency than the standard DC-SCF calculations.

The proposed algorithms can be directly applied to the DFT calculations. Furthermore, they are important for the post-HF calculations. In many cases, DC-HF calculations are more expensive than DC-MP2 ones [26,27]. Nakai research group previously developed the efficient parallelization algorithm for the DC-MP2 method [22]. The combination of the DC-SCF code with the previous DC-MP2 code would enable to extend the applicability of MP2 calculations using the parallel computers.

References

1. OpenMP, http://www.openmp.org. (accessed December 8, 2014)
2. J. Nieplocha, R. J. Harrison, R. J. Littlefield, J. Supercomput. 10 (1996) 197.
3. G. D. Floetcher, M. W. Schmidt, B. M. Bode, M. S. Gordon, Comput. Phys. Commun. 128 (2000) 190.
4. MPI, http://www.mpich.org. (accessed December 8, 2014)
5. M. F. Guest, I. J. Bush, H. J. J. Van Dam, P. Shenwood, J. M. H. Thomas, J. H. Van Lenthe, R. W. A. Havenith, J. Kendrick, Mol. Phys. 103 (2005) 719.
6. M. Valiev, E. J. Bylaska, N. Govind, K. Kowalski, T. P. Straatsma, H. J. J. Van Dam, D. Wang, J. Nieplocha, E. Apra, T. L. Windus, W. A. de Jong, Comput. Phys. Commun 181 (2010) 1477.
7. I. M. B. Nielsen, C. L. Janssen, Comput. Phys. Commun. 128 (2000) 238.
8. K. Ishimura, K. Kuramoto, Y. Ikuta, S. Hyodo, J. Chem. Theor. Comput. 6 (2010) 1075.
9. P. Koval, D. Foerster, O. Coulaud, J. Chem. Theor. Comput. 6 (2010) 2654.
10. K. Ishimura, S. Ten-no, Theor. Chem. Acc. 130 (2011) 317.
11. M. Katouda, T. Nakajima, J. Chem. Theor. Comput. 9 (2013) 5373.
12. Y. Hasegawa, J. Iwata, M. Tsuji, D. Takahashi, A. Oshiyama, K. Minami, T. Boku, H. Inoue, Y. Kitazawa, I. Miyoshi, M. Yokokawa, Int. J. High Performance Computing Applications 3 (2014) 335.
13. D. G. Fedorov, R. M. Olson, K. Kitaura, M. S. Gordon, S. Koseki, J. Comput. Chem. 25 (2004) 872.
14. Y. Mochizuki, K. Yamashita, K. Fukuzawa, K. Takematsu, H. Watanabe, N. Taguchi, Y. Okiyama, M. Tsuboi, T. Nakano, S. Tanaka, Chem. Phys. Lett. 493 (2010) 346.
15. K. Kristensen, T. Kjaergaard, I. M. Hoyvik, P. Ettenhuber, P. Jorgensen, B. Jansik, S. Reine, J. Jakowski, Mol. Phys. 111 (2013) 1196.
16. W. Yang, Phys. Rev. Lett. 66 (1991) 1438.
17. W. Yang, T. S. Lee, J. Chem. Phys. 103 (1995) 5674.
18. T. Akama, M. Kobayashi, H. Nakai, J. Comput. Chem. 28 (2007) 2003.
19. T. Akama, A. Fujii, M. Kobayashi, H. Nakai, Mol. Phys. 105 (2007) 2799.
20. T. Akama, M. Kobayashi, H. Nakai, Int. J. Quantum Chem. 109 (2009) 2706.
21. M. Kobayashi, T. Yoshikawa, H. Nakai, Chem. Phys. Lett. 500 (2010) 172.
22. M. Katouda, M. Kobayashi, H. Nakai, S. Nagase, J. Comput. Chem. 32 (2011) 2756.
23. D. G. Fedorov, R. M. Olson, K. Kitaura, M. S. Gordon, S. Koseki, J. Comput. Chem. 25 (2004) 872.

24. R. Krishnan, J. S. Binkley, R. Seeger, J. A. Pople, J. Chem. Phys. 72 (1980) 650.
25. M.W. Schmidt, K.K.Baldridge, J.A.Boatz, S.T. Elbert, M.S. Gordon, J.H. Jensen, S.Koseki, N. Matsunaga, K.A. Nguyen, S. Su,T.L. Windus,M. Dupuis, J.A. Montgomery Jr., J.Comput. Chem. 14 (1993) 1347.
26. M. Kobayashi, Y. Imamura, H. Nakai, J. Chem. Phys. 127 (2007) 074103.
27. T. Yoshikawa, M. Kobayashi, H. Nakai, Theor. Chem. Acc. 130 (2011) 411.

Chapter 8
Divide-and-Conquer Self-Consistent Field Calculation Using Resolution-of-Identity Approximation on Graphical Processing Units

8.1. Introduction

Nvidia GPUs and Intel Xeon Phi coprocessors obtain higher performance for four arithmetic operations than CPUs by using CUDA and OpenMP, respectively. Since 2008, GPUs have been utilized in two-electron integral computations [1–7], the HF method [8–12], DFT [13–18], MP2 theory [19,20], CC theory [21–25], and the semiempirical method [26,27]. Pioneering works by Yasuda [1,13] presented accelerated computations of the exchange-correlation term in DFT and evaluated two-electron integrals on GPUs. In the innovative works by Martinez and coworkers [2,4,6,9,12,16], fundamental computations in quantum chemistry such as two-electron integral evaluations, direct SCFs, analytical energy gradients, and TDDFT were implemented on GPUs. In those studies, the GPU memory layout, data flow, and computation mapping were intensively discussed for the efficient coding on GPUs. As a result, sophisticated and tuned implementations were achieved by adopting advanced programing techniques for parallelization.

Accelerated math libraries are being developed such as the cuBLAS [28], cuSPARSE [28], CULA [29], MAGMA [30], and VSIPL [31]. The use of math libraries could minimize the task of developing efficient GPU codes and guarantee compatibility with future development of GPU hardware. It is important to assess how suitable the combinations of the math libraries and quantum chemistry codes are on a practical platform. In fact, recent studies regarding GPU implementations adopted math libraries [8,13,16–23]. As such, performance assessments using math libraries become increasingly important. A recent paper by Gordon and coworkers [32] assessed DGEMM operations, a frequently used math library, and data transfer on Nvidia GPUs and Intel Xeon Phi coprocessors.

Although the hardware and software including the math libraries of GPUs have advanced, the slow CPU-GPU memory access as well as small GPU main memoryhinder further progress. Conventional *ab initio* codes on GPUs might be influenced by such drawbacks upon application to large systems. For instance, HF/DFT calculations for large systems that include construction and diagonalization of the enormous Fock matrix require communication between the GPU and CPU. Therefore, theoretical developments

to reduce such communication are essential to achieve high performance GPU implementations. Linear-scaling HF/DFT methods [33–45], which divide an entire system into several fragments, could avoid the slow memory access and other shortfalls of GPU memory by separately constructing and diagonalizing the local Fock matrix in each fragment. In addition, the GPU memory could effectively be utilized by the combination of the linear-scaling method with other methods, such as the RI and density fitting approximations [46–51], to reduce construction costs. The RI method is one of the most effective methods in massive parallel calculations, as exemplified by several successful attempts using the MP2 theory achieved by the high parallel efficiency of the RI method [52,53] and the compatibility with linear-scaling methods [54–56].

In this Chapter, the author implemented CPU and GPU codes for RI-HF based on the linear-scaling DC method [35–38]. An advantage in adopting the DC method is the wide applicability to systems with delocalized electrons and/or spins, for example. In the implementations of the RI-HF and DC-RI-HF codes on GPUs, the author adopted math libraries, namely, cuBLAS and MAGMA, in order to maintain compatibility with future developments of the GPU hardware.

8.2. Theory and Implementation

8.2.1. Theory of DC-RI-HF

In the DC-RI-HF method, calculations of the Fock matrix are evaluated by adopting the RI approximation of ERIs:

$$(\mu\nu|\lambda\sigma) \approx \sum_{l,m} (\mu\nu|l)(l|m)^{-1}(m|\lambda\sigma), \tag{8.1}$$

where $(\mu\nu|l)$ and $(l|m)$ are the three-center and two-center AO ERIs, respectively. Since the $(l|m)$ matrix is positive, definite calculations of $(l|m)^{-1}$ can be efficiently performed by the Cholesky decomposition of the $(l|m)$

$$(l|m) = \sum_{n} L_{ln} L_{nm}^{T}, \tag{8.2}$$

followed by the efficient inversion of the triangular matrix $\boldsymbol{L}$, such that

$$(l|m)^{-1} = \sum_{n} L_{ln}^{-T} L_{nm}^{-1}. \tag{8.3}$$

Insertion of Eq. (8.3) in Eq. (8.1) leads to Coulomb $\boldsymbol{J}$ and exchange $\boldsymbol{K}$ terms:

$$\begin{aligned} J_{\mu\nu} \approx J_{\mu\nu}^{\text{DC-RI}} &= \sum_{\lambda,\sigma}\sum_{l,m,n} (\mu\nu|l)(l|m)^{-1}(m|\lambda\sigma) D_{\lambda\sigma}^{\text{DC}} \\ &= \sum_{\lambda,\sigma}\sum_{k} (\mu\nu|k)(k|\lambda\sigma) D_{\lambda\sigma}^{\text{DC}} \end{aligned} \tag{8.4}$$

$$\begin{aligned} K_{\mu\nu} \approx K_{\mu\nu}^{\text{DC-RI}} &= \sum_{\lambda,\sigma}\sum_{l,m,n} (\mu\lambda|l)(l|m)^{-1}(m|\nu\sigma) D_{\lambda\sigma}^{\text{DC}} \\ &= \sum_{\lambda,\sigma}\sum_{k} (\mu\lambda|k)(k|\nu\sigma) D_{\lambda\sigma}^{\text{DC}} \end{aligned} \tag{8.5}$$

where the transformed integrals $(\mu\lambda|k)$ are used. The Coulomb portion can be formulated as two scalar products: namely, the products between the three-center integrals and density matrix and between the intermediate result W_k and integrals:

$$W_k = \sum_{\lambda\sigma} (k|\lambda\sigma) D_{\lambda\sigma}^{\text{DC}} \tag{8.6}$$

$$J_{\mu\nu}^{\text{DC-RI}} = \sum_{k} (\mu\nu|k) W_k \tag{8.7}$$

The exchange contribution is evaluated by performing the matrix multiplication twice and summing over the results:

$$T_{\nu\lambda}^{k} = \sum_{\sigma} (k|\nu\sigma) D_{\lambda\sigma}^{\text{DC}} \tag{8.8}$$

$$W_{\mu\nu}^{k} = \sum_{\lambda} (\mu\lambda|k) T_{\nu\lambda}^{k} \tag{8.9}$$

$$K_{\mu\nu}^{\text{DC-RI}} = \sum_{k} W_{\mu\nu}^{k} \tag{8.10}$$

Although the above discussion is for closed-shell systems, the DC-RI-HF method can easily be extended to open-shell calculations using an unrestricted spin-orbital treatment.

8.2.2. Implementation of DC-RI-HF

The author implemented four Fortran codes in total: RI-HF/CPU, RI-HF/GPU, DC-RI-HF/CPU, and DC-RI-HF/GPU. To begin, the author explains the difference between the RI-HF and DC-RI-HF methods for diagonalization and construction of the Fock matrix. The DC method solves the local Roothaan–Hall equation corresponding to each subsystem $\mathbf{S}(s)$. By separately solving the local Roothaan–Hall equation, the parallel efficiency for diagonalizing the DC calculations is higher than that for the standard method, even though the construction scheme for the DC calculations is the same as that for the standard calculations. However, construction costs of the DC calculations will be smaller than those for the standard calculations as the system size increases, because the sparse density matrix in the DC calculations makes screening more efficient as compared to standard HF calculations.

In the RI-HF and DC-RI-HF methods with the GPU code, both diagonalization and construction of the Fock matrix are designed to run on GPU architectures. In the GPU code, the diagonalization time is reduced with MAGMA libraries, which are linear algebra algorithms and frameworks for hybrid many-core and GPU systems. Fig. 8.1 presents the pseudocode for the construction of RI-HF and DC-RI-HF algorithms. The construction consists of three steps: (1) generation of the two-center ERIs, (2) generation and transformation of the three-center ERIs, and (3) evaluation of the Coulomb and exchange contributions. The transformation of the three-center integrals $(\mu\lambda|k)$ and evaluation of the Coulomb and exchange contributions in Eqs. (8.6)–(8.10), which could be performed effectively on a GPU, are implemented using cuBLAS, especially cuBLASDGEMM, cuBLASDDOT, and cuBLASDAXPY. An alternative choice might be mixed precision matrix libraries [20,57], which effectively separate the double-precision and single-precision operations. The transformation and evaluation on CPU are implemented using Intel MKL. After Steps 1 and 2 are performed in the first SCF iteration, the transformed three-center ERIs are stored separately in the CPU main memory of each node by MPI. Because all of the transformed three-center ERIs cannot be stored in the small GPU memory, the three-center ERIs should be copied from CPU to GPU, as shown

in parentheses in Fig. 8.1. SIMD processing of GPU could perform the matrix operations on GPU and communicate between the CPU and GPU simultaneously. For example, the transformation of the three-center ERIs in Step 2 and evaluation of the Coulomb and exchange contribution in Step 3 could occur concurrently. Furthermore, the communication cost could be reduced because of the sparse density matrix of the DC-HF calculation. The author also implemented a multi-GPU code. For Fock constructions, multiple GPUs in parallel handle cyclically different rows of basis sets at Step 2 and auxiliary basis sets at Step 3.

[Step 1]
Evaluate $(l|m)$
Cholesky decomposition of $(l|m) = \sum_n L_{ln} L^T_{nm}$
Evaluate $(l|m)^{-1}$

[Step 2]
Evaluate $(\mu\nu|l)$
Do loop μ
(Copy $(\mu\nu|l)$ from CPU to GPU)
Index transformation $(\mu\nu|n) = \sum_l (\mu\nu|l) L^T_{nl}$
(Copy $(\mu\nu|n)$ from GPU to CPU)
End loop

[Step 3]
Do loop k
(Copy $(\mu\nu|n)$ from CPU to GPU)
Coulomb part:
Index transformation $W_k = \sum_{\lambda\sigma} (k|\lambda\sigma) D_{\lambda\sigma}$
Evaluate $J^{\mathrm{RI}}_{\mu\nu} = \sum_k (\mu\nu|k) W_k$
Exchange part:
Index transformation $T^k_{\nu\lambda} = \sum_\sigma (k|\nu\sigma) D_{\lambda\sigma}$
Index transformation $W^k_{\mu\nu} = \sum_\lambda (\mu\lambda|k) T^k_{\nu\lambda}$
Evaluate $K^{\mathrm{RI}}_{\mu\nu} = \sum_k W^k_{\mu\nu}$
End loop
(Copy $J^{\mathrm{RI}}_{\mu\nu}$ and $K^{\mathrm{RI}}_{\mu\nu}$ from GPU to CPU)

Fig. 8.1. Pseudocode of the Fock construction algorithm in the RI-HF method. The parts in parentheses are performed using only the GPU code.

8.3. Numerical assessment

In this section, the performances of RI-HF and DC-RI-HF calculations with the GPU codes are numerically assessed by comparison to CPU results. All calculations were performed using a modified version of the GAMESS program package [58]. In the DC-HF and DC-RI-HF calculations, the inverse temperature parameter of the Fermi function β in Eq. (4) was fixed to 200 a.u. unless otherwise noted. Two Intel Xeon E5-2643 (3.30 GHz) processors and Nvidia K20 were used on eight CPU cores and 2496 CUDA cores per node, respectively. All calculations adopted two-electron integral screening with the threshold of 10^{-9} hartree and C_1 symmetry.

First, the author examined the efficiency of the RI-HF method using CPU and GPU for small molecules: benzene, naphthalene, anthracene, tetracene, and pentacene. The cc-pVTZ basis set and corresponding auxiliary basis set were adopted [59,60]. Table 8.1 shows the wall-clock times and total energies of the standard HF and RI-HF calculations. The speedups from the standard HF cases are shown in parentheses. For both CPU and GPU, the RI technique reduced the wall-clock times. For CPU, the speedups of RI-HF as compared to the standard HF changed slightly, i.e., 3.23–3.89, while those of RI-HF for GPU increased remarkably. This was because the performance of the cuBLAS libraries on GPU increases with respect to matrix size.

Table 8.2 shows the wall-clock times of individual steps in the RI-HF calculations for the small molecules with respect to the number of basis sets, N_{BS}. Namely, Step 1 corresponds to the generation of the two-center ERIs, Step 2 to the generation and transformation of the three-center ERIs, and Step 3 to the evaluation of the Coulomb and exchange contributions. Because the computational costs of Step 1 are small and not accelerated well on GPU, Step 1 was examined on CPU for CPU and GPU cases, as discussed in Section 2. In Steps 2 and 3, the GPU code reduced the wall-clock times, with the exception of Step 2 for benzene and naphthalene. Step 3 performs better than Step 2 because there is less communication between CPU and GPU in Step 3 than in Step 2. The energy errors of the RI-HF results as compared those of the standard HF for benzene, naphthalene, anthracene, tetracene, and pentacene were less than 1 mhartree. Table 8.2 also shows the required memory sizes of the RI-HF on GPU for benzene, naphthalene, anthracene, tetracene, and pentacene. The GPU required small memory size scales $O(n^2)$.

Table 8.1. Wall-clock times (in s) and total energies (in hartree) of the standard HF and RI-HF calculations on CPUGPU for calculations of benzene, naphthalene, anthracene, tetracene, and pentacene using the cc-pVTZ and corresponding auxiliary basis sets. Speedups and energy differences in mhartree from standard HF are shown in parentheses. Two Intel Xeon E5-2643 (3.30 GHz) processors and Nvidia K20 were used on octa-cores and 2496 CUDA cores, respectively. The numbers of SCF iterations are also listed.

Molecule	N_{BS}	Wall-clock time [s]					Total energy [s]			N_{iter}
		HF	RI-HF				HF	RI-HF	(diff.) [mhartree]	
		CPU	CPU	(Speedup)	GPU	(Speedup)				
Benzene	300	51.2	13.8	(3.71)	9.4	(5.45)	-230.776747	-230.776988	(0.241)	9
Naphthalene	470	243.2	51.1	(4.76)	35.2	(6.91)	-383.472343	-383.472795	(0.452)	10
Anthracene	640	1056.2	122.0	(8.66)	75.2	(14.04)	-536.134531	-536.135136	(0.605)	10
Tetracene	810	2852.1	396.4	(7.20)	146.9	(19.41)	-688.825718	-688.826495	(0.777)	11
Pentacene	980	6321.2	886.0	(7.13)	308.4	(20.50)	-841.545909	-841.545083	(0.823)	12

Table 8.2. Wall-clock times (in s) of individual steps in the standard HF and RI-HF calculations on CPU/GPU. The wall-clock time in Step 2 is separated into the generation time t_{gen} and transformation time t_{tran} of the three-center ERIs. Memory size [MB] required in the GPU calculation are also listed.

Molecule	N_{BS}	CPU				GPU				
		Wall-clock time [s]				Wall-clock time [s]				Memory size
		Step 1	Step 2		Step 3	Step 2		Step 3		
			t_{gen}	t_{tran}		t_{tran}	(Speedup)		(Speedup)	
Benzene	300	0.1	0.4	2.8	9.9	2.9	(1.0)	5.4	(1.8)	2.8
Naphthalene	470	0.1	1.6	6.3	40.3	8.6	(0.7)	22.1	(1.8)	6.9
Anthracene	640	0.2	3.3	13.2	97.5	12.7	(1.0)	51.2	(1.9)	12.8
Tetracene	810	0.2	6.5	31.1	344.2	15.8	(1.9)	110.0	(3.1)	20.5
Pentacene	980	0.3	13.3	75.3	769.0	21.9	(3.4)	244.8	(3.2)	30.0

Next, the author examined the efficiency of the DC-RI-HF method using GPU for polyacene, $C_{44}H_{26}$, which is a delocalized system. The 6-311G** basis set and corresponding auxiliary basis set were adopted [61,62]. Table 8.3 shows the wall-clock times of the standard HF, DC-HF, RI-HF, and DC-RI-HF methods. In the DC calculations, C_4H_2 (or C_6H_2 for the center and C_4H_4 for the edges) was adopted as the central region and the adjacent three units on either side were treated as the corresponding buffer region. The standard HF and DC-HF calculations were examined on CPU, while the RI-HF and DC-RI-HF calculations were examined on CPU and GPU. The speedups from standard HF are shown in parentheses. The DC method accelerated the diagonalization step by solving the local Roothaan–Hall equation corresponding to each subsystem. Moreover, the computational cost for the Fock construction could be reduced because of the sparse density matrix of the DC-HF calculation. The DC-HF method brought about a 1.4-fold speedup, although the numbers of SCF iterations were 15 and 18 in the standard and DC method, respectively. The combination of GPU and RI reduced the construction time drastically, providing a 4.2-fold speedup. The MAGMA libraries also decreased the diagonalization time. DC-RI-HF with the GPU code achieved a 4.6-fold speedup for the total time by combining the three technologies: namely, the DC method, RI approximation, and GPU implementation. The error in energy from the standard HF method was less than 1 kcal/mol. The author further investigated the possibility of using multiple GPUs in parallel. The 4-GPU system demonstrated a speedup of 17.5-fold, which was comparable and slightly faster than that with four independent single GPUs, which achieved a 3.7-time acceleration on each single GPU, namely, 14.8-fold.

Table 8.3 also shows the total energies of the standard HF, DC-HF, RI-HF, and DC-RI-HF methods. The energy differences from the standard HF result are given in parentheses. The differences introduced by the DC and RI methods were 0.207 and 0.856 mhartree, respectively. The summation of the differences by the DC-HF and RI-HF methods was comparable with the difference by DC-RI-HF method; 0.970 mhartree achieves so-called chemical accuracy ($\leq$ 1 kcal/mol).

Table 8.3. Wall-clock times (in s) of the construction t_{fock} and diagonalization t_{diag} of the Fock matrix and total energies (in hartree) for the standard HF, DC-HF, RI-HF, and DC-RI-HF calculations of polyacene, $C_{44}H_{26}$, using the 6-311G** and corresponding auxiliary basis sets. Speedups and energy differences in mhartree from standard HF are presented in parentheses. Two Intel Xeon E5-2643 (3.30 GHz) processors and Nvidia K20 were used on octa-cores and 2496 CUDA cores, respectively.

Method	Wall-clock time [s]						Total energy	(diff.)
	t_{fock}	(Speedup)	t_{diag}	(Speedup)	Total	(Speedup)	[hartree]	[mhartree]
HF/CPU	2481.9		45.0		2526.9		-1757.163227	-
DC-HF/CPU	1932.1	(1.3)	16.2	(2.7)	1948.3	(1.3)	-1757.163020	(-0.207)
RI-HF/CPU	1214.2	(2.0)	45.1	(1.0)	1259.3	(2.0)	-1757.162371	(-0.856)
DC-RI-HF/CPU	1123.5	(2.2)	16.1	(2.7)	1139.6	(2.2)	-1757.162257	(-0.970)
RI-HF/GPU	573.8	(4.3)	15.5	(2.9)	589.3	(4.3)	-1757.162371	(-0.856)
DC-RI-HF/GPU	542.8	(4.6)	5.1	(8.8)	547.9	(4.6)	-1757.162257	(-0.970)
DC-RI-HF/4 GPU	142.8	(17.4)	1.4	(32.1)	144.2	(17.5)	-1757.162257	(-0.970)

The wall-clock times for water clusters $(H_2O)_n$ (n = 75–125) were measured using the 6-311G** and corresponding auxiliary basis sets. Fig. 8.2 shows the wall-clock times per SCF iteration of the standard-HF, DC-HF, and DC-RI-HF calculations with respect to the number of water molecules, n. In the DC calculations, a single H_2O molecule was adopted as the central region while atoms lying within 5.0 Å of each central region were treated as the corresponding buffer regions. The standard HF and DC-HF calculations were examined on CPU, while the DC-RI-HF calculations were performed on GPU. In these calculations, the FMM implemented in the GAMESS program was activated. The DC-HF method reduced the order of the SCF calculation, so that the times scale with $O(n^{2.13})$ and $O(n^{1.37})$ for standard HF and DC-HF calculations was estimated by a double-logarithmic plot, respectively. As expected, the DC-RI-HF calculations with the GPU code achieved 4.1–5.0 fold speedups of the SCF calculations as compared to DC-HF; the times scaled with $O(n^{1.30})$. Unlike with the small molecules, the scalings were close to those using CPU because acceleration of the product of the double precision matrices by the cuBLAS libraries saturated at matrices larger than 3000×3000 in size.

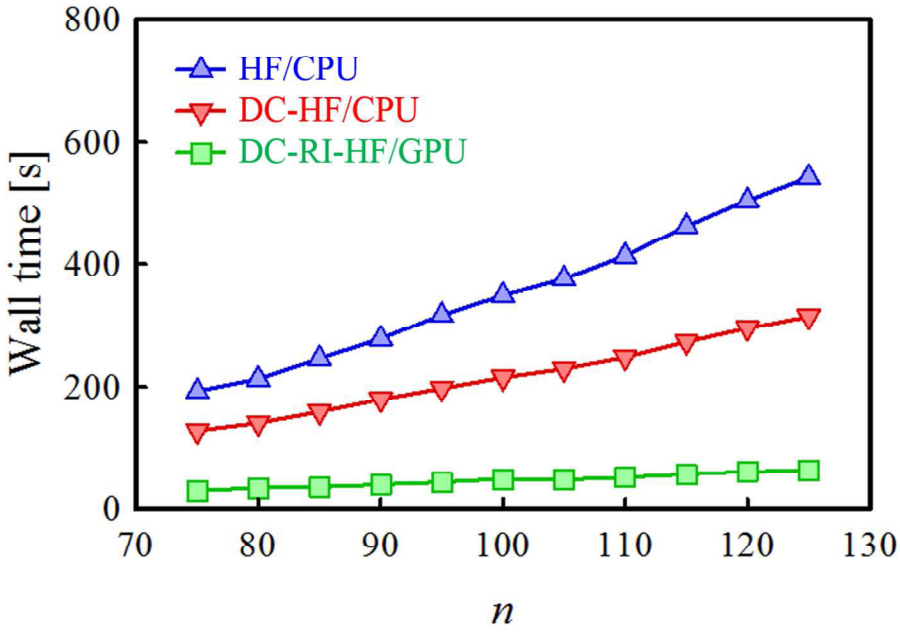

Fig. 8.2. System-size dependence of the wall-clock times (in s) of the standard HF, DC-HF, and DC-RI-HF per SCF iteration of water clusters $(H_2O)_n$ at the 6-311G**

Finally, a series of benchmark HF calculations on polyglycine ($C_{32}N_{16}O_{16}H_{50}$), phenol in 120 explicit water molecules (C_6H_5OH + 120 H_2O), olestra ($C_{156}H_{278}O_{19}$), and protein (1FSV in the Protein Data Bank [63], $C_{158}N_{48}O_{43}H_{257}$) were performed, as depicted in Fig. 8.3. The DC conditions are summarized in Table 8.4. The buffer regions were considered as the atoms contained within a radius r_b of each central region. The number of basis sets of the total system N_{tot} and the maximum number of basis sets of the subsystem N_{sub} are shown in Table 8.4.

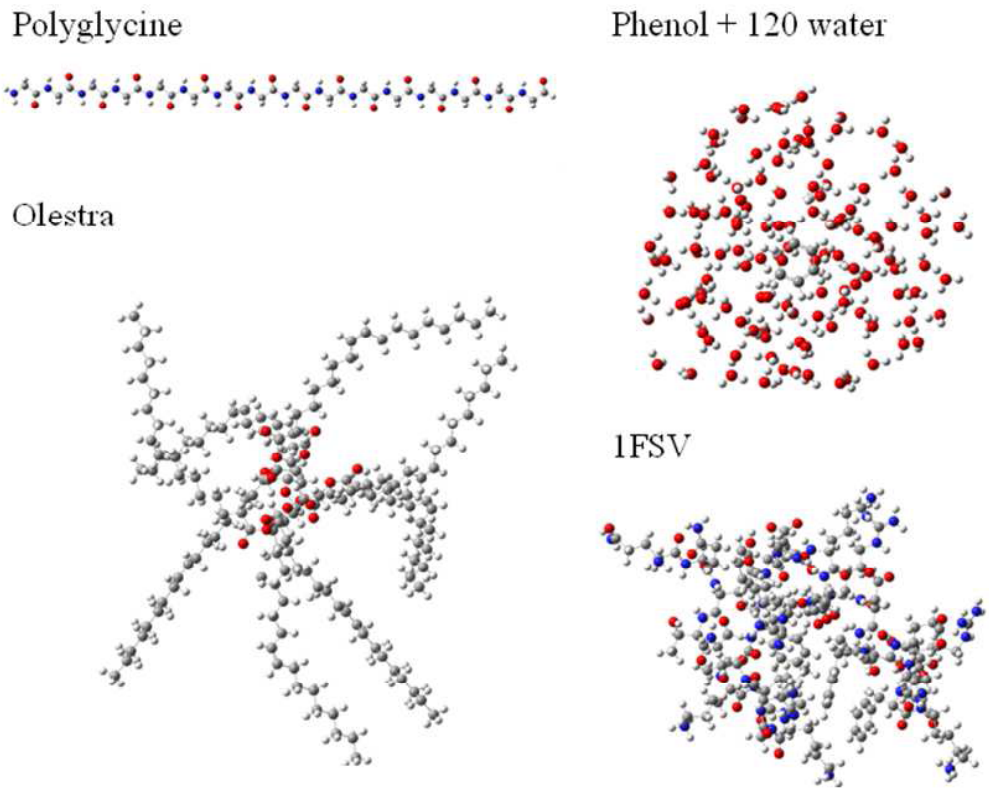

Fig. 8.3. Structures of polyglycine ($C_{32}N_{16}O_{16}H_{50}$), phenol in 120 explicit water molecules (C_6H_5OH + 120 H_2O), olestra ($C_{156}H_{278}O_{19}$), and 1FSV ($C_{158}N_{48}O_{43}H_{257}$)

Table 8.5 shows the numbers of SCF iterations N_{iter}, wall-clock times per SCF iteration, and total energies in the standard HF and DC-RI-HF calculations using the 6-311G** and corresponding auxiliary basis sets. The standard HF and DC-RI-HF calculations were examined on CPU and four GPUs, respectively. The speedups and energy errors from the standard HF results are presented in parentheses. Except for olestra, the SCF convergences of the DC method were the same as the standard ones. In all of the calculations, the DC-RI-HF method with the GPU code showed high efficiency and chemical accuracy. The speedups of DC-RI-HF on GPU compared with standard HF increased with increasing molecular size because of the sparse density matrix and local diagonalization by the DC-HF method. The errors in the energy of polyglycine, phenol in 120 explicit water molecules, olestra, and 1FSV from the standard HF method were 0.74, 0.89, 0.87, and 0.93 mhartree, respectively.

Table 8.4. Conditions of DC calculations for polyglycine ($C_{32}N_{16}O_{16}H_{50}$), phenol in 120 explicit water molecules (C_6H_5OH + 120 H_2O), olestra ($C_{156}H_{278}O_{19}$), and protein (1FSV in the Protein Data Bank, $C_{158}N_{48}O_{43}H_{257}$). The buffer regions were considered as the atoms contained within a radius r_b (in Å) of each central region. N_{tot} and N_{sub} indicate the number of basis sets of the total system and the maximum number of basis sets of the subsystem, respectively.

	$C_{32}N_{16}O_{16}H_{50}$	C_6H_5OH+120 H_2O	$C_{156}H_{278}O_{19}$	$C_{158}N_{48}O_{43}H_{257}$
Central region	C_2NOH_3/C_2NOH_4 (one glycine unit)	C_6H_5OH/H_2O (phenol/one water molecule)	2.0 Å cubic grid	2.0 Å cubic grid
r_b	8.9	5.0	7.0	7.0
N_{tot}	1132	3127	3943	4753
N_{sub}	350	977	1141	1164

Table 8.5. Wall-clock times (in s) per SCF iteration, total energies (hartree), and the numbers of SCF iterations N_{iter} in the standard HF and DC-RI-HF calculations of polyglycine ($C_{32}N_{16}O_{16}H_{50}$), phenol in 120 explicit water molecules (C_6H_5OH + 120 H_2O), olestra ($C_{156}H_{278}O_{19}$), and 1FSV ($C_{158}N_{48}O_{43}H_{257}$) using the 6-311G** and corresponding auxiliary basis sets. Speedups and energy differences in mhartree from standard HF are presented in parentheses. Two Intel Xeon E5-2643 (3.30 GHz) processors and Nvidia K20 were used on octa-cores and 2496 CUDA cores, respectively.

	Wall-clock time [s]			Total energy [s]			N_{iter}	
	HF/CPU	DC-RI-HF/GPU	(Speedup)	HF/CPU	DC-RI-HF/GPU	(diff.) [mhartree]	HF/CPU	DC-RI-HF/GPU
$C_{32}N_{16}O_{16}H_{50}$	46.6	15.3	(3.05)	-3310.1504	-3310.1496	(0.741)	11	11
C_6H_5OH + 120 H_2O	792.4	206.2	(3.84)	-9424.9912	-9424.9903	(0.889)	13	13
$C_{156}H_{278}O_{19}$	1594.0	204.6	(7.79)	-7539.8667	-7538.9917	(0.875)	14	15
$C_{158}N_{48}O_{43}H_{257}$	3051.3	332.7	(9.17)	-11909.2510	-11908.3191	(0.932)	13	13

8.4. Conclusion

In this Chapter, the author performed GPU implementations for accelerating HF calculations by combining the linear-scaling DC method with the effective RI technique. Math libraries, i.e. cuBLAS and MAGMA, for GPU were adopted in order to reduce the implementation task as well as guarantee the compatibility with future development of the GPU architecture. For comparison, four different codes, namely, RI-HF/CPU, RI-HF/GPU, DC-RI-HF/CPU, and DC-RI-HF/GPU were implemented. Numerical assessments of the present methods, DC-RI-HF/GPU, displayed higher efficiency than the others as well as standard HF/CPU. Speedups from standard HF calculations increased with increasing molecular size. This was because the performance of the cuBLAS libraries on GPU increases with respect to matrix size, while the total density matrix of DC-HF calculations became sparse in larger systems. Furthermore, the wall-clock times for DC-RI-HF calculations scaled linearly with respect to the system size. Therefore, the DC-RI-HF/GPU code is promising in large systems, even if GPU architectures are modified in the future.

References

1. K. Yasuda, J. Comp. Chem. 29 (2008) 334.
2. I. S. Ufimtsev, T. J. Martinez, J. Chem. Theory Comp. 4 (2008) 222.
3. A. Asadchev, V. Allada, J. Felder, B. M. Bode, M. S. Gordon, T. L. Windus, J. Chem. Theory Comp. 6 (2010) 696.
4. N. Luehr, I. S. Ufimtsev, T. J. Martinez, J. Chem. Theory Comp. 7 (2011) 949.
5. K. A. Wilkinson, P. Sherwood, M. F. Guest, K. Naidoo, J. Comp. Chem. 32 (2011) 2313.
6. F. V. Titov, I. S. Ufimtsev, N. Luehr, T. J. Martinez, J. Chem. Theory Comp. 9 (2013) 213.
7. Y. Miao, K. M. Merz, Jr., J. Chem. Theory Comp. 9 (2013) 965.
8. I. S. Ufimtsev, T. J. Martinez, J. Chem. Theory Comp. 5 (2009) 1004.
9. I. S. Ufimtsev, T. J. Martinez, J. Chem. Theory Comp. 5 (2009) 2619.
10. P. P. Janes, A. P. Rendell, J. Chem. Theory Comp. 7 (2011) 1549.
11. A. Asadchev, M. S. Gordon, J. Chem. Theory Comp. 8 (2012) 4166.
12. C. M. Isborn, A. W. Gotz, M. A. Clark, R. C. Walker, T. J. Martinez, J. Chem. Theory Comp. 8 (2012) 5092.
13. K. Yasuda, J. Chem. Theory Comp. 4 (2008) 1230.
14. L. Genovese, M. Ospici, T. Deutsch, J. F. Mehaut, A. Neelov, S. Goedecker, J. Chem. Phys. 131 (2009) 034103.
15. P. Brown, C. J. Woods, S. McIntosh-Smith, F. R. Manby, J. Comp. Chem. 31 (2010) 2008.
16. C. M. Isborn, N. Luehr, I. S. Ufimtsev, T. J. Martinez, J. Chem. Theory Comp. 7 (2011) 1814.
17. X. Andrade, A. Aspuru-Guzik, J. Chem. Theory Comp. 9 (2013) 4360.
18. M. A. Nitsche, M. Ferreria, E. E. Mocskos, L. M. C. Gonzalez, J. Chem. Theory Comp. 10 (2014) 959.
19. L. Vogt, R. Olivares-Amaya, S. Kermes, Y. Shao, C. Amador-Bedolla, A. Aspurn-Guzik, J. Phys. Chem. A 112 (2008) 2049.
20. R. Olivares-Amaya, M. A. Watson, R. G. Edgar, L. Vogt, Y. Shao, A. Aspuru-Guzik, J. Chem. Theory Comp. 6 (2010) 135.
21. A. E. DePrince, J. R. Hammond, J. Chem. Theory Comp. 7 (2011) 1287.
22. W. Ma, S. Krishnamoorthy, O. Villa, K. Kowalski, J. Chem. Theory Comp. 7 (2011) 1316.
23. K. Bhaskaran-Nair, W. J. Ma, S. Krishnamoorthy, O. Villa, H. J. J. van Dam, E. Apra,

K. Kowalski, J. Chem. Theory Comp. 9 (2013) 1949.
24. A. Asadchev, M. S. Gordon, J. Chem. Theory Comp. 9 (2013) 3385.
25. A. E. DePrince, M. R. Kennedy, B. G. Sumpter, C. D. Sherrill, Mol. Phys. 112 (2014) 844.
26. J. D. C. Maia, G. A. U. Carvalho, C. P. Mangueira, S. R. Santana, L. A. F. Cabral, G. B. Rocha, J. Chem. Theory Comp. 8 (2011) 3072.
27. X. Wu, A. Koslowski, W. Thiel, J. Chem. Theory Comp. 8 (2012) 2272.
28. cuBLAS, https://developer.nvidia.com/cublas (accessed June 1, 2014).
29. CULA, http://www.culatools.com/ (accessed June 1, 2014).
30. MAGMA,http://icl.cs.utk.edu/magma (accessed June 1, 2014).
31. VSIPL, http://www.omgwiki.org/hpec/vsipl (accessed June 1, 2014).
32. S. S. Leang, A. P. Rendell, M. S. Gordon, J. Chem. Theory Comp. 10 (2014) 908.
33. W. Yang, Phys. Rev. Lett. 66 (1991) 1438.
34. W. Yang, T. S. Lee, J. Chem. Phys. 103 (1995) 5674.
35. T. Akama, M. Kobayashi, H. Nakai, J. Comp. Chem. 28 (2007) 2003.
36. T. Akama, A. Fujii, M. Kobayashi, H. Nakai, Mol. Phys. 105 (2007) 2799.
37. T. Akama, M. Kobayashi, H. Nakai, J. Comp. Chem. 109 (2009) 2706.
38. M. Kobayashi, T. Yoshikawa, H. Nakai, Chem. Phys. Lett. 500 (2010) 172.
39. A. Imamura, Y. Aoki, K. Maekawa, J. Chem. Phys. 95 (1991) 5419.
40. J. Korchowiec, F. L. Gu, Y. Aoki, Int. J. Quantum Chem. 105 (2005) 875.
41. S. R. Gadre, R. N. Shirsat, A. C. Limaye, J. Phys. Chem. 98 (1994) 9165.
42. K. Kitaura, E. Ikeo, T. Asada, T. Nakano, M. Uebayasi, Chem. Phys. Lett. 313 (1999) 701.
43. S. R. Pruitt, D. G. Fedorov, K. Kitaura, M. S. Gordon, J. Chem. Theory Comp. 6 (2010) 1.
44. H. Umeda, Y. Inadomi, T. Watanabe, T. Yagi, T. Ishimoto, T. Ikegami, H. Tadano, T. Sakurai, U. Nagashima, J. Comp. Chem. 31 (2010) 2381.
45. H. Nakata, D. G. Fedorov, T. Nagata, S. Yokojima, K. Ogata, K. Kitaura, S. Nakamura, J. Chem. Phys. 137 (2012) 044110.
46. J. L. Whitten, J. Chem. Phys. 58 (1973) 4496.
47. B. I. Dunlap, J. W. D. Connolly, J. R. Sabin, J. Chem. Phys. 71 (1979) 3396.
48. E. J. Baerends, D. E. Ellis, P. Ros, Chem. Phys. 2 (1973) 41.
49. O. Vahtras, J. Almlöf, W. Feyereisen, Chem. Phys. Lett. 213 (1993) 514.
50. H. A. Fruchtl, R. A. Kendall, R. J. Harrison, K. G. Dyall, Int. J. Quantum Chem. 64 (1997) 63.
51. F. R. Manby, J. Chem. Phys. 119 (2003) 4607.

52. D. E. Bemholdt, R. J. Harrison, Chem. Phys. Lett. 250 (1996) 477.
53. M. Katouda, T. Nakajima, J. Chem. Theory Comp. 9 (2013) 5373.
54. R. A. Distasio, R. P. Steele, M. Head-Gordon, Mol. Phys. 105 (2007) 2731.
55. A. P. Pahalkar, M. Katouda, S. R. Gadre, S. Nagase, J. Comp. Chem. 31 (2009) 2405.
56. T. Ishikawa, K. Kuwata, Chem. Phys. Lett. 474 (2009) 195.
57. M. Watson, R. Olivares-Amaya, R. G. Edgar, A. Aspuru-Guzlk, Computing in Science and Engineering 12 (2010) 40.
58. M. W. Schmidt, K. K. Baldridge, J. A. Boatz, S. T. Elbert, M. S. Gordon, J. H. Jensen, S. Koseki, N. Matsunaga, K. A. Nguyen, S. Su, T. L. Windus, M. Dupuis, J. A. Montgomery, Jr., J. Comp. Chem. 14 (1993) 1347.
59. T. H. Dunning, Jr., J. Chem. Phys. 90 (1989) 1007.
60. F. Weigend, A. Köhn, C. Hättig, J. Chem. Phys. 116 (2002) 3175.
61. M. Tanaka, M. Katouda, S. Nagase, J. Comp. Chem. 29 (2013) 2568.
62. R. Krishnan, J. S. Binkley, R. Seeger, J. A. Pople, J. Chem. Phys. 72 (1980) 650.
63. PDB, http://www.rcsb.org (accessed February 1, 2014).

General Conclusion

In this thesis, the author reported theoretical extension and high parallelization of the DC method. In Part I of this thesis, the author performed the theoretical extension for open-shell calculation of the DC method. In Chapter 2, the DC-SCF method was extended to spin-unrestricted open-shell calculations. Numerical assessments revealed that the accuracy of the DC-UHF method was comparable to that of the closed-shell DC-HF method: the energy and spin-density errors reduced along with the buffer size. Non-integer charge and spin densities in each subsystem were also confirmed. Furthermore, the CPU time for the DC-UHF calculation scaled linearly with respect to the system size by combining with the FMM. In Chapter 3, the author enabled the correlated open-shell treatment in the framework of the DC-based correlation method. The present DC-UMP2 method was assessed in calculations of the spin- and charge-delocalized polyene cation systems. Numerical assessments revealed that the DC-UMP2 method: has the advantageous features of the closed-shell DC-MP2 method: the correlation energy errors are generally small achieving the chemical accuracy and are controllable with the buffer size, the CPU time scales quasi-linearly with respect to the system size, and the required memory size becomes constant.

In Part II of this thesis, the author performed the theoretical extension for excited-state calculations of the DC method. In Chapter 4, the author has developed the DC-based SAC method as a good starting point to excited-state calculations. In the numerical assessments of the present method, the local orbitals constructed in the DC method improve the performance of the configuration selection in the SAC calculations, as well as that the computational time scales quasi-linearly with respect to the system size. In Chapter 5, the author has developed a DC-based SACCI theory in conjunction with the DC-CIS theory and DC-TDDFT. The excitation energy errors are generally small, indicating that high chemical accuracy is achieved. It was confirmed that the present scheme enabled efficient excited-state calculations of large systems. Chapter 6 presented the development and numerical assessments of excited-state calculations using dynamic polarizabilities as alternative excited-state calculations for large systems. Chapter 6 proposed an algorithm that searches the pole of the polarizability at regular intervals, obtains accurate excitation energies and oscillator strengths with the bisection method, and subtracts contributions of detected excited states. The numerical assessments investigated the convergence condition and regular interval dependence of excitation energies and oscillator strengths. By using the proper threshold and regular interval, the present algorithm effectively detects all poles without loss of accuracy. The algorithm

with DC as well as conventional TDCPHF methods could reproduce the large-charge-transfer excitation.

In Part III of this thesis, the author accelerated the DC method by using parallel computations. Chapter 7 proposed two efficient algorithms of the linear-scaling DC-SCF method for parallel computations. The present algorithms could reduce the network communications in determining the common Fermi level. The AFL and AEN methods adopted approximate techniques to estimate the Fermi level in the latter part of SCF procedure. The numerical assessments of the present methods clarified that the AFL and AEN methods were confirmed to display a higher parallel efficiency than the standard DC-SCF calculations. In Chapter 8, the author performed GPU implementations for accelerating HF calculations by combining the linear-scaling DC method with the effective RI technique. Math libraries for GPU were adopted in order to reduce the implementation task as well as guarantee the compatibility with future development of the GPU architecture. Numerical assessments of the present methods, DC-RI-HF/GPU, displayed higher efficiency than the others as well as standard HF/CPU. Furthermore, the wall-clock times for DC-RI-HF calculations scaled linearly with respect to the system size.

Acknowledgement

本研究は早稲田大学化学・生命化学科中井浩巳教授のご指導のもとで行われました。中井教授には研究室配属以来の 6 年間，研究指導のみならず様々なことを根気強くお教えいただきました。本論分の執筆に当たりましても、多くのご助言を頂きました。ここに、心よりお礼申し上げます

また，本論文をまとめるにあたり同化学・生命化学科の古川行夫教授，井村考平教授から多くのご助言，ご意見を頂きました。心より感謝致します。

本論分の研究を進めるにあたり、多くの人たちにご助言を頂きました。特に、本論文の第一・二部につきましては、DC 法の開発者であり、所属した班のリーダーであった小林正人助教よりプログラムの実装および研究内容に関する貴重なご助言を頂きました。また、今村穣博士、菊池那明博士、赤間知子博士、西澤宏晃博士、清野淳司博士、五十幡康弘博士、石川敦之博士、王祺博士、西村好史博士には、研究のみならず、発表に関するアドバイスなども頂きました。同じ Order(*N*)班の先輩方である藤井厚彦修士、當眞嗣貴修士からは学部時代から修士過程にかけて手厚いご指導を賜りました。また、同班であった樽見望都修士、高田雄太修士、野中佑太郎学士と吉原詢也君、後輩の窪田崇人修士、中嶋裕也修士と中野匡彦修士には、様々な協力をしていただきました。特に、本論分の 6 章において野中佑太郎学士の協力がなければ完成しなかったと思います。また、学部卒業後は別々の進路でしたが同輩である岡田剛嗣修士がいたことで乗り越えることができました、全員の氏名を挙げることはできませんが、本論分を完成させることができたのはこれらの方々の多くのご支援のおかげです。心から感謝いたします。

また，2012 年度から 2013 年度においては，文部科学省グローバル COE プログラム『実践的化学知教育研究拠点』と 2013 年度から 2014 年度においては、学術振興会『特別研究員奨励費』による研究費の補助を頂き，円滑に研究を進めることができました。ここに御礼申し上げます。

最後に，大学入学から学位取得まで経済的，精神的に支援してくれた家族に感謝致します。

List of Achievement

1．論文

○ 1．Masato Kobayashi, **Takeshi Yoshikawa**, and Hiromi Nakai
『Divide-and-Conquer Self-Consistent Field Calculation for Open-Shell Systems: Implementation and Application』
Chem. Phys. Lett., **500** (1-3), 172 (2010).

○ 2．**Takeshi Yoshikawa**, Masato Kobayashi, and Hiromi Nakai
『Linear-Scaling Divide-and-Conquer Second-Order Møller-Plesset Perturbation Calculation for Open-Shell Systems: Implementation and Application』
Theor. Chem. Acc., **130** (2-3), 411 (2011).

○ 3．**Takeshi Yoshikawa**, Masato Kobayashi, and Hiromi Nakai
『Divide-and-conquer-based symmetry adapted cluster method: Synergistic effect of subsystem fragmentation and configuration selection』
Int. J. Quantum Chem., **113** (3), 218 (2013).

○ 4．**Takeshi Yoshikawa**, Masato Kobayashi, Atsuhiko Fujii, and Hiromi Nakai
『Novel approach to excited-state calculations of large molecules based on divide-and-conquer method: application to photoactive yellow protein』
J. Phys. Chem. B, **117** (18), 5565-5573 (2013).

○ 5．**Takeshi Yoshikawa** and Hiromi Nakai
『Linear-scaling self-consistent field calculations based on divide-and-conquer method using resolution-of-identity approximation on graphical processing units』
J. Comp. Chem., **36** (3), 164-170 (2015).

6．Daeheum Cho , Kyoung Chul Ko , Yasuhiro Ikabata , Kazufumi Wakayama , **Takeshi Yoshikawa** , Hiromi Nakai , Jin Yong Lee
『Effect of Hartree-Fock Exact Exchange on Intramolecular Magnetic Coupling Constants of Organic Diradicals』
J. Chem. Phys., in press.

2．講演

国際発表

(口頭発表)

1．○Masato Kobayashi, Tomoko Akama, Tsuguki Touma, **Takeshi Yoshikawa**, and Hiromi Nakai

『Linear-scaling electronic structure calculations based on divide-and-conquer method』

2010 International Chemical Congress of Pacific Basin Societies, PHYS1291, Honolulu, USA, (December 2010).

2．○Masaki Okoshi, Yuta Takada, **Takeshi Yoshikawa**, Patchreenart Saparpakorn, and Hiromi Nakai

『Theoretical study on the mechanisum of fluorescence enhancement of Pico Green』

17th International Annual Symposium on Computational Science and Engineering, 67, Khon Kaen, Thailand, (March 2013).

3. ○**Takeshi Yoshikawa**, and Hiromi Nakai

『Acceleration oflarge-scale calculation with GPGPU: hybrid of divide-and-conquer method and resolution-of-identity approximation』

International Symposium on Computational Sciences: Simulations for Material and Biological Systems, session I, Shanghai, China, (November 2013).

(ポスター発表)

1．○**Takeshi Yoshikawa**, Masato Kobayashi and Hiromi Nakai

『Linear-scaling divide-and-conquer calculations for open-shell systems』

2010 International Chemical Congress of Pacific Basin Societies, PHYS1291, Honolulu, USA, (December 2010).

2．○**Takeshi Yoshikawa**, Masato Kobayashi and Hiromi Nakai

『Divide-and-conquer symmetry-adapted cluster method』

The Seventh Congress of the International Society for Theoretical Chemical Physics, 4PP-24, Tokyo, Japan, (September 2011).

3．○**Takeshi Yoshikawa**, Masato Kobayashi and Hiromi Nakai

『Excited-state calculation of photoactive yellow protein using divide-and-conquer SAC-CI theory』

XVII International Workshop on Quantum Systems in Chemistry and Physics, P28, Turuku, Finland, (August 2012).

4．○**Takeshi Yoshikawa**, Masato Kobayashi, Yutaro Nonaka, and Hiromi Nakai

『Excited-state calculations based on divide-and-conquer method for large systems』
17th International Annual Symposium on Computational Science and Engineering, 69, Khon Kaen, Thailand, (March 2013).

5．○**Takeshi Yoshikawa**, and Hiromi Nakai
『Acceleration of divide-and-conquer method on GPU』
The VIIIth congress of the international society for theoretical chemical physics, II-69, Budapest, Hungary, (August 2013).

国内発表

(口頭発表)

1．○**吉川武司**、小林正人、中井浩巳
『非制限軌道法を用いた分割統治(DC)開殻系計算』
日本コンピュータ化学会 2010 年春季年会、1O08、東京、2010 年 5 月

2．○中井浩巳、**吉川武司**、野中祐太郎
『非局所励起状態に対する分割統治(DC)型線形スケーリング法の開発』
第 6 回分子科学討論会、1E18、東京、2012 年 9 月

3．○高田雄太、Patchreenart Saparpakorn, 大越昌樹、**吉川武司**、中井浩巳
『PicoGreen の蛍光増強メカニズムに関する理論的研究』
日本化学会第 93 春季年会(2013)、3G3-12、滋賀、2013 年 3 月

4．○**吉川武司**、中井浩巳
『GPU を用いた分割統治型電子状態計算の高速化』
第 7 回分子科学討論会、4E01、京都、2013 年 9 月

(ポスター発表)

1．○**吉川武司**、小林正人、中井浩巳
『大規模開殻系計算のための分割統治(DC)非制限 Hartree-Fock 法の開発』
日本化学会第 3 回関東支部大会、P1-003、東京、2009 年 9 月

2．○**吉川武司**、小林正人、中井浩巳
『分割統治(DC)法を用いた大規模開殻系計算』
第 3 回分子科学討論会、2P104、愛知、2009 年 9 月

3．○**吉川武司**、小林正人、中井浩巳
『分割統治(DC)法に基づく大規模開殻系電子相関計算:DC-UMP2』
第 13 回理論化学討論会、2P43、北海道、2010 年 5 月

4．○**吉川武司**、小林正人、中井浩巳
『DC-UHF、DC-UMP2 法の GAMESS への実装とアセスメント』

スーパーコンピューターワークショップ 2011、P14、愛知、2011 年 1 月

5. ○**吉川武司**、小林正人、中井浩巳

『DC-SAC 法～大規模励起状態理論の構築に向けて～』

日本コンピュータ化学会 2011 年春季年会、3P07、東京、2011 年 5 月

6. ○小林正人、赤間知子、當眞嗣貴、**吉川武司**、五十幡康、中井浩巳

『第 2 回次世代ナノ統合シミュレーションソフトウェア説明会』、東京、2012 年 1 月

7. ○**吉川武司**、小林正人、中井浩巳

『DC-SAC-CI 法～大規模励起状態理論の構築～』

日本コンピュータ化学会 2012 春季年会、1P10、東京、2012 年 5 月

8. ○**吉川武司**、小林正人、中井浩巳

『DC-SAC-CI 法による光活性タンパクの励起状態計算』

第 15 回理論化学討論会、1P09、宮城、2012 年 5 月

9. ○**吉川武司**、小林正人、中井浩巳

『分割統治法に基づく大規模励起状態計算法の確立：DC-SAC-CI 法』

第 6 回分子科学会シンポジウム、P005、東京、2012 年 6 月

10. ○**吉川武司**、中井浩巳

『統一的なフェルミ準位を用いない分割統治型量子化学計算法の開発』

第 6 回分子科学討論会、4P-121、東京、2012 年 9 月

11. ○野中祐太郎、**吉川武司**、中井浩巳

『非局所励起状態に対する分割統治(DC)型線形スケーリング法の数値検証』

第 6 回分子科学討論会、4P-087、東京、2012 年 9 月

12. ○**吉川武司**、中井浩巳

『CUDA/OpenACC を用いた GPU による分割統治法の高速化』

日本コンピュータ化学会 2013 春季年会、1P14、東京、2013 年 5 月

13. ○野中祐太郎、**吉川武司**、中井浩巳

『動的分極率計算に基づく励起状態計算法: 汎用アルゴリズムの開発』

日本コンピュータ化学会 2013 春季年会、1P16、東京、2013 年 5 月

3. 受賞

1. **吉川武司**

第 1 回関根吉郎賞『高速な励起状態計算理論の開発：大規模生体分子への適用』

早稲田大学先進理工学部化学・生命化学科稲化会、東京、2012 年 3 月

４．科研費採択課題

1. **吉川武司**

日本学術振興会特別研究員(DC2)　2013 年度

『大規模分子シミュレーションによる高機能性光学物質の理論設計』